Modelling of Turbulent Premixed Combustion using LES and RANS methods

M.E Usman Allauddin

Full copy of the thesis approved by the Department of Aerospace Engineering of the Bundeswehr University Munich for obtaining the Doctoral degree

Doctor of Engineering (Dr.-Ing)

Advisor:

1. Prof. Dr. rer. nat. Michael Pfitzner
2. ……
3. ……

The doctoral thesis was submitted at the Bundeswehr University Munich on 6th February, 2017 and accepted by the Department of Aerospace Engineering on 13th February, 2017. The oral examination took place on 4th July, 2017.

Acknowledgments

Firstly, I would like to thank Almighty Allah, who gave me the strength and dedication to persevere through the difficult times and complete my PhD work. Without His support this would never be possible.

The present work is conducted at the Institute of Thermodynamics of University of Bundeswehr Munich and I would like to gratefully acknowledge those who provided great assistance during my stay (about four and half years) in Munich.

I would like to especially thank my supervisor, Prof. Michael Pfitzner, for his invaluable guidance, advice and support given throughout the entire work. I am indebted to him for showing great confidence in me and always pushing me to achieve greater heights. Discussions with him were always quite helpful especially when things did not work out as expected. His constant support and encouragement always gave me the motivation and devotion to complete all the tasks.

The support received from Prof. Markus Klein and Prof. Nilanjan Chakraborty is also gratefully acknowledged. The collaboration with them was very beneficial and provided a way to learn and develop my understanding of turbulent combustion modelling.

I wish to especially thank my colleague Gabriele Frank for her assistance at the beginning of the work; a period of time in which I had no knowledge of combustion modelling. Even after that, she was very helpful, friendly and useful whenever I needed any assistance.

I would also like to thank Dr. Eike Tangermann, Syed Ahmad Raza and Dr. Mahrukh for reviewing my work and for the valuable feedback.

Last but not the least, my utmost gratitude is reserved for my parents, wife, daughters and all my well-wishers for always being there through my good and bad times.

Abstract

With increasing computational power, investigation of turbulent combustion by the Large Eddy Simulation (LES) method has emerged as a potential and reliable technique compared to the conventional Reynolds-averaged Navier-Stokes (RANS) approach. However, the turbulent premixed combustion modelling offers a problem of great importance since the flame thickness is typically too thin to be resolved on the typical LES filter sizes and thus, a model is required to describe the extent of subgrid scale flame wrinkling. In the present work the Flame Surface Density (FSD) method is used to model the filtered LES reaction rate. There are two well-established approaches for FSD modelling. In one approach the FSD is modelled in terms of a transport equation, while the other approach involves an algebraic formulation where equilibrium of production and dissipation of FSD is assumed. The present work is focused on the latter approach. In this work a recently developed LES subgrid FSD premixed combustion model has been used to investigate various features of significant importance. Firstly, the performance of a simplified version of the aforementioned model is investigated and validated with the original model and well documented experimental data. It is found that both original and simplified models are suitable for LES of low to high turbulent premixed combustion in ambient and elevated pressure conditions. Secondly, the performance of the original model is investigated in conjunction with more refined sub-grid scalar flux (SGSF) modelling. A significant change of the overall flame speed is not observed for different SGSF models. However, the flame shape and thickness respond to the modelling of SGSF. The detailed explanations for the observed behavior are presented. Thirdly, the effects of high pressure and the Lewis number (Le = thermal diffusivity/mass diffusivity) in premixed turbulent combustion are analytically and numerically investigated using some of the popular algebraic FSD models available in open literature. The original models are tuned to incorporate these two effects using an extensive parametric study based on numerical findings as well as on theoretical argumentation. The tuned models give satisfactory agreement with the experimental data. Fourthly, a RANS version of the FSD model is developed which is the focus of the current work. The performance of the RANS model is compared with the original LES model and validated with the experimental data. It is found that the RANS version of the model shows a reasonable agreement with the experimental data. Lastly, 1D flame calculations are done to investigate the effects of $|\nabla \bar{c}|$ versus $|\nabla \tilde{c}|$ in the generalized FSD expression in combination with different counter gradient type SGSF models.

Kurzzusammenfassung

Mit zunehmender Rechenleistung hat sich die Large-Eddy-Simulation (LES) neben der herkömmlich Reynolds-gemittelten Navier-Stokes-Simulation (RANS) zu einer vielversprechenden und zuverlässigen Simulationsmethode für die turbulente Verbrennung entwickelt. Eine große Schwierigkeit bei der LES turbulent vorgemischter Verbrennungen stellen die typischen LES-Filterweiten dar, welche zu weit sind, um die dünnen Flammendicken aufzulösen. Daher sind weitere Modelle erforderlich, um die Feinstrukturflammenfaltung zu beschreiben. In der vorliegenden Arbeit wird ein Flammenoberflächendichte-Modell (FSD) eingesetzt, um die LES-gefilterte Reaktionsrate zu modellieren. Innerhalb der FSD-Modellierungen haben sich zwei zentrale Ansätze etabliert. In einem Ansatz wird eine Transportgleichung für die FSD formuliert und gelöst. Alternativ kann, unter der Annahme eines Gleichgewichts zwischen Produktion und Dissipation, die FSD durch eine algebraische Formulierung beschrieben werden. Diese Arbeit verwendet den letzteren Ansatz. Mit dem neu entwickelten FSD-Modell werden folgende zentrale Eigenschaften mittels LES untersucht. Erstens, das ebengenannte vereinfachte FSD-Modell wird anhand experimenteller Daten validiert und die Leistungsfähigkeit mit dem Ausgangsmodells verglichen. Dabei zeigt sich, dass sowohl das ursprüngliche Modell als auch das vereinfachte Modell für die LES schwach bis stark turbulenter Vormischverbrennungen bei Umgebungsdruck bis hin zu hohen Drücken geeignet sind. Zweitens wird der Einfluss modifizierter Feinstrukturskalar-fluss-Modelle (SGSF) im Ausgangsmodell untersucht. Für die verschiedenen SGSF-Modelle sind keine signifikanten Veränderungen der resultierenden Flammengeschwindigkeit zu erkennen. Hingegen unterscheiden sich die berechneten Flammenformen und Flammendicken. Diese Abweichungen werden anschließend ausführlich in der Arbeit diskutiert. Drittens, die Gültigkeit des neuen Modells bei hohen Drücken und Variationen der Lewis-Zahl (Le = thermische Diffusivität/Diffusivität der Masse) für vorgemischte turbulente Verbrennungen wird analytisch untersucht und mit vorhandenen FSD-Modellen aus der Literatur verglichen. Dazu werden die bestehenden Modellansätze erweitert und in einer umfangreichen Parameterstudie untersucht. Die Ergebnisse der modifizierten Modelle weisen gute Übereinstimmungen mit den experimentellen Daten auf. Viertens, eine RANS-Version des FSD-Modells wird mit den Daten aus der LES verglichen und mit experimentellen Daten validiert. Dabei zeigt sich, dass die RANS hinreichend genaue Ergebnisse im Vergleich zu den Experimenten bietet. Abschließend werden eindimensionale Flammen simuliert, um die Effekte von $|\nabla \bar{c}|$ bzw. $|\nabla \tilde{c}|$ in der verallgemeinerten FSD-Modellierung in Verbindung mit verschiedenen sog. Gegengradient-SGSF-Modellen zu analysieren.

Table of Contents

List of figures

Figure 5.4: Variation of s_t/s_L^0 with u'/s_L^0 for (a) $p = 0.1$ MPa and (b) $p = 1.0$ MPa using methods given by Eqs. (5.2)-(5.4), which are indicated by M1, M2 and M3 in Figs. 5.4(a) and (b)

Figure 6.1: Comparison of time average $\langle\tilde{c}\rangle$ and instantaneous progess variable $\tilde{c}$ contours with (a) original (b) simplified Keppeler model.

Figure 6.2: Graphical representation of the method used to calculate flame speed

Figure 6.3: Comparison of turbulent flame speed at (a) 1 bar (b) 5 bar (c) 20 bar using methane fuel with original and simplified Keppeler models

Figure 6.4: Comparison of time-averaged $\langle\bar{c}\rangle$ and instantaneous flame surface $\tilde{c}$ with (a) GRAD (b) CLARK (c) HUAI models for case 4A; (d) an overlay of instantaneous flame contours for GRAD, CLARK and HUAI models for case 4A. The inner lines denote $\tilde{c} = 0.05$ whiles outer lines denote $\tilde{c} = 0.95$.

Figure 6.5: Comparison of time-averaged $\langle\bar{c}\rangle$ and instantaneous flame surface $\tilde{c}$ with (a) GRAD (b) CLARK (c) HUAI model for case 12A.

Figure 6.6: Influence of filter width on the time-averaged $\langle\bar{c}\rangle$, instantaneous flame surface $\tilde{c}$, FSD Σ and $|\nabla\tilde{c}|$ with HUAI model for (a) case 4A (b) 4C, and with CLARK model for (c) case 4A (d) 4C.

Figure 6.7: Comparison of turbulent flame speed at (a) 0.1 MPa, (b) 0.5 MPa and (c) 1.0 MPa using methane fuel

Figure 6.8: Figure 9. (a) Correlation coefficients between $\partial\left(F_i^{sg}\right)/\partial x_i$ and $\partial\left(F_i^{sg,model}\right)/\partial x_i$ for models GRAD, CLARK, IMPL: $c^{u',\Delta}$(■); $c^{\Delta}(u'/S_L = 5.0)$ (■); $c^{\Delta}(u'/S_L = 6.25)$ (■); $c^{\Delta}(u'/S_L = 7.5)$ ( ); $c^{\Delta}(u'/S_L = 9.0)$ (■) and $c^{\Delta}(u'/S_L = 11.25)$ (■)

Figure 6.9: Comparison of turbulent flame speed at (a) 1 bar and (b) 5 bar using tuned Keppeler model for propane fuel

Figure 6.10: Analytical comparison of wrinkling factor at (a) 1 bar, (b) 5 bar and (c) 10 bar using the original versions of the models for methane fuel

Figure 6.11: Analytical comparison of wrinkling factor at (a) 1 bar, (b) 5 bar and (c) 10 bar using the tuned versions of the models for methane fuel

Figure 6.12: Influence of filter width on the time-averaged $\langle\bar{c}\rangle$, instantaneous flame surface $\tilde{c}$, FSD Σ and $|\nabla\tilde{c}|$ with tuned Fureby model for (a) case 4A, (b) 4C, (c) case 12A (d)12C.

List of tables

Nomenclature

English symbols

A_L	Laminar flame surface area	m^2
A_t	Wrinkled flame surface area	m^2
$B(r)$	Flux limiter function	–
c	Reaction progress variable	–
C_{K1}	LES Keppeler model constant	–
C_{K2}	RANS Keppeler model constant	–
C_M	Muppala model constant	–
C_A	Angelberger model constant	–
C_Z	Zimont model constant	–
C_{EBU}	Eddy break-up model constant	–
C_s	Smagorinsky constant	–
C_P	Specific heat at constant pressure	J/kgK
D	Fractal dimension	–
D_{th}	Thermal diffusivity	m^2/s
D_t	Turbulent diffusivity	m^2/s
Da	Damköhler number	–
Da_Δ	Subgrid Damköhler number	–
$E(\kappa)$	Turbulent kinetic energy as a function of wavenumber κ	m^3/s^2
F	Thickening factor for ATF model	–
$F_{C,f}$	Convective fluxes over cell face f	–
$F_{D,f}$	Diffusive fluxes over cell face f	–
G	Scalar quantity used in G-equation model	–
G^*	Chosen G iso-level	–
h	Enthalpy	J/kg
k	Turbulent kinetic energy	m^2/s^2
k_{sgs}	Turbulent kinetic energy	m^2/s^2
Ka	Karlovitz number	–
Ka_Δ	Subgrid Karlovitz number	–
l_0	Integral length scale of turbulence	m
l_η	Kolmogorov length scale of turbulence	m
Le	Lewis number	–
Ma	Markstein number	–
M	Mach number	–
N_i	Resolved flame normal in the i-direction	–
p	Pressure	Pa
Re	Reynolds number	–
Re_{crit}	Critical Reynolds number	–
Re_t	Turbulent Reynolds number	–
s_t	Turbulent flame speed	m/s
s_L^0	Un-stretched laminar flame speed	m/s
s_L	Stretched laminar flame speed	m/s

S_{ij}	Shear stress tensor	1/s
Sc_t	Schmidt number	–
t	Time	s
t_η	Kolmogorov time scale	s
T	Temperature	K
T_a	Activation temperature	K
T_{ad}	Adiabatic temperature	K
T_b	Burnt temperature	K
T_u	Unburnt temperature	K
u'	RMS turbulent velocity	m/s
u'_Δ	Subgrid scale velocity fluctuations	m/s
u_i	Velocity component	m/s
U	Bulk velocity at inlet	m/s
u_η	Kolmogorov velocity	m/s
V	Volume	m^3
x_i	Spatial coordinate i	m
Y_k	Mass fraction of species k	–

Greek

α	Diffusivity	m^2/s
Γ	Efficiency function	–
δ_L^0	Thermal flame thickness	m
δ_L^t	Total flame thickness	m
δ_t	Turbulent flame brush thickness	m
δ_L	Zeldovich flame thickness	m
Δ	Filter size	m
Δx	Grid spacing	m
ϵ	Turbulent energy dissipation rate	m^2/s^3
ε_i	Inner cut off scale	m
ε_o	Outer cut off scale	m
η	Kolmogorov length scale	m
κ	Flame stretch rate	1/s
κ_s	Flame strain rate	1/s
μ	Dynamic viscosity	kg/ms
μ_t	Turbulent dynamic viscosity	kg/ms
ν	Kinematic viscosity	m^2/s
ν_t	Kinematic viscosity	m^2/s
ρ	Density	kg/m^3
Σ	Flame surface density	1/m
τ	Heat release factor	–
τ_c	Chemical time scale	s
τ_f	Flow or mixing time scale	s
τ_{ij}	Stress tensor	kg/ms^2
τ_{ij}^{sgs}	Subgrid stress tensor	kg/ms^2
Φ	Equivalence ratio	–

φ	Flame angle	radian
$\dot{\omega}$	Turbulent reaction source term	kg/m^{3}s
Ξ	Flame wrinkling factor	–

Superscripts and subscripts

$(.)''$	Backward reaction
$(.)'$	Forward reaction
$(.)^0$	Initial state at $t = 0$
$(.)^n$	Quantity at time level n
$(.)_{ad}$	Adiabatic
$(.)_b$	Burnt state
$(.)_f$	Cell face quantity
$(.)_{\mathrm{E}}$	Quantity at midpoint of a cell located east of cell *P*
$(.)_{\mathrm{e}}$	Quantity at the east face of cell *P*
$(.)_\Delta$	Filter size as length scale
$(.)_i$	Inner
$(.)_k$	k^{th} species
$(.)_o$	Outer
$(.)_{\mathrm{P}}$	Quantity at midpoint of cell *P*
$(.)_{res}$	Resolved
$(.)_{sgs}$	Subgrid scale
$(.)_t$	Turbulent
$(.)_{th}$	Thermal
$(.)_{tot}$	Total
$(.)_u$	Unburnt state
$(.)_{\mathrm{W}}$	Quantity at midpoint of a cell located west of cell *P*
$(.)_{\mathrm{w}}$	Quantity at the west face of cell *P*

Abbreviation

1D	One dimensional
3D	Three dimensional
ATF	Artificially thickened flame
BML	Bray Moss Libby analysis
BRZ	Broken reaction zones
CD	Central differencing scheme
CF	Corrugated flamelet
CFD	Computational fluid dynamics
CFL	Courant Friedrich Levy criterion
CGT	Counter-gradient transport
CV	Control volume
DNS	Direct numerical simulation
EBU	Eddy break-up
FFFD	Filtered flame front displacement
FDF	Flame density function
F-TACLES	Filtered tabulated chemistry for LES

FSD	Flame surface density
FV	Finite volume
GT	Gradient transport
KPP	Kolmogorov, Petrovski and Piskunov
LES	Large eddy simulation
LHS	Left-hand-side of an equation
PDE	Partial differential equation
RANS	Reynolds-averaged Navier-Stokes/simulation
RHS	Right-hand-side of an equation
SGS	Subgrid scale
SGSF	Subgrid scalar flux
SAFSD	Static algebraic flame surface density
TRZ	Thin reaction zones
TVD	Total variation diminishing
UD	Upwind differencing scheme
WF	Wrinkled flamelet

Chapter 1

Introduction

It is estimated that the total world energy consumption will be increased by 48% from 2012 to 2040 [1]. The global energy demand is primarily fulfilled by burning fossil fuels. Though extremely important in our daily lives, the dependence on fossil fuels has led to an issue of considerable significance–environmental pollution. The main pollutants produced by combustion are carbon dioxide, which is a main contributor to global warming, unburned harmful gases like nitrogen oxides (NO and NO_2), carbon monoxide and sulphur oxides (SO_2 and SO_3). Worldwide, there is a growing tendency of shifting towards alternative clean energy resources such as hydro, wind, solar etc., but they are unlikely to substitute fossil fuels in the foreseeable future, as it is estimated that about 78% of energy demand will still be accounted by consuming fossil fuels in 2040 [1]. Thus a detailed understanding of combustion and its control are essential to enhance the efficiency, safety, reliability and pollutants emission control of practical combustion devices.

The turbulent premixed combustion is the focus of the current work. It is encountered in many useful engineering devices, e.g., spark-ignition engines, industrial gas turbines, reheat systems in jet engines, industrial gas burners and gaseous explosions in a turbulent environment. Figure 1.1 shows four different examples of combustion chamber configurations involving premixed flames. In this mode of combustion, the fuel and oxidizer are mixed prior to chemical reaction and it is characterized by a flame front propagating into a mixture of fresh premixed reactants. It offers the advantages of lower emissions and better combustion efficiency. Because of the complex processes of flame folding on different length and time scales, many aspects of this type of combustion are still not fully understood. Also the combustors may experience combustion instabilities, producing oscillations that effectively reduce the combustor's lifetime. This can be prevented by better combustor designs, which is often accompanied by enhanced understanding of combustion processes. Experimental studies were used as the most direct method to achieve this goal in the times when computing power was lacking and numerical methods were not as developed as they are in recent rimes. Moreover, experimental studies are often limited by high equipment costs, handling difficulties and the accessibility issues in taking optical measurements of situations similar to the real combustors.

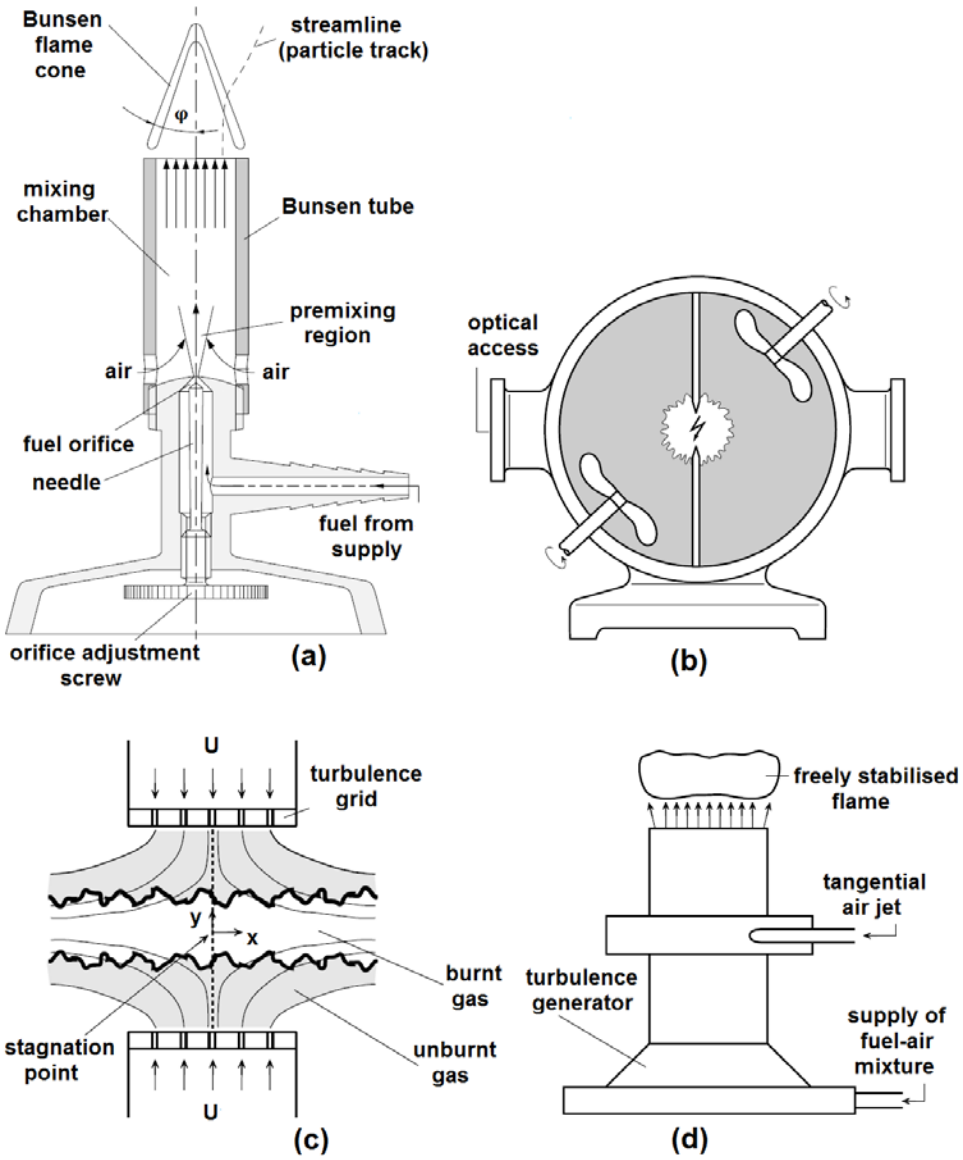

Figure 1.1: (a) classical Bunsen burner showing premixing in the Bunsen tube [2] (b) spherical premixed flame propagation in a combustion vessel [2] (c) turbulent counter flow premixed flames [2] (d) swirl burner with a freely stabilized premixed flame [2]

Increasing computational power and recent advances in the numerical methods have made possible the numerical study of combustion phenomenon, the predictions of unsteady turbulent reactive flows and offered a supportive tool for better design and development of combustors. Several robust and reliable modelling approaches have been developed which can describe the turbulence–chemistry interactions for different flow configurations. The RANS method is still a popular choice in the industrial sector, offering fast efficient simulation results with relatively

low computational resources. However, the ability to compute only temporally averaged quantities has restricted the application of RANS method in predicting instantaneous flow features and combustion instabilities. At the other extreme of the available computational methods is Direct Numerical Simulation (DNS) approach which removes the necessity of any numerical model as it resolves all the turbulent and chemical length and time scales of the flow field. Although DNS can be effectively used as a research tool for a model development but it requires highly expensive computational effort that restricts its use for practical engineering systems. The intermediate approach between RANS and DNS is LES approach, which has become quite famous in recent times. In LES, large scale geometry dependent flow structures are resolved and directly computed, while small scale turbulent structures are modelled. This presents the accurate prediction of large scale unsteadiness of the flow which is particularly important in the study of combustion instabilities. The small scale structures with sizes below the LES filter width, which are considered isotropic, are modelled. Rapidly increasing computational power has increased the use of LES method and allowed simulations of complex and moderate Reynolds number combustion cases. LES is computationally more expensive than RANS, but its advantages may compensate the costs as reported in [3,4].

1.1 Literature overview

Large Eddy Simulation (LES) has, in recent times, shown potential to remove the limitations imposed by the traditional RANS methods for the predictions of turbulent reactive flows [3,4]. However, in the turbulent premixed combustion a pertinent problem lies in the subgrid scale (SGS) modelling. It is difficult because of the flame thickness, which is typically too thin to be resolved on the typical LES filter sizes. Several modelling approaches have been developed by different researchers to overcome this issue, such as the flame front tracking method (level-set of G-equation [2,5]), the Artificially Thickened Flame (ATF) technique [6,7] and the concept of Flame Surface Density (FSD) [8,9]. The aforementioned three approaches generally describe the closure of the reaction rate through changes in flame surface area. The subgrid scale flame wrinkling is the main contributor to this change, whose extent can be measured by the wrinkling factor Ξ, which can also be described as a ratio of the turbulent to laminar flame speeds s_t/s_L in the case of little variation of local flame speed.

The well-established FSD based reaction rate closure approach exists with two main variants. In one approach the concept is implemented through algebraic expressions [8], while the other involves solving an additional FSD transport equation [9]. The latter offers certain advantages as it avoids the assumption of equilibrium of subgrid production and dissipation of FSD and accounts for the processes of resolved flame strain, curvature and propagation. These characteristics provide a way to capture unsteady flame propagation with combustion instabilities or conditions where the flame experiences progressive flame wrinkling with time. But it adds considerable complexity and presents a number of difficult modelling challenges. Thus, the method has been applied only to a limited number of a priori and LES studies [10-13]. In the Dynamic FSD concept [14,15], which is an another variant of algebraic formulation, the extent of wrinkling based on instantaneous resolved flame characteristics is automatically adjusted and thus it has the potential for modelling conditions with progressive flame wrinkling. The dynamic formulation relies on scale similarity between different filter sizes, thus it may encounter practical difficulties in selecting a correct combination of test filter width, averaging procedure and updating frequency. Several static algebraic flame surface density (SAFSD) models have been developed and applied in different premixed flame burners [16,17]. They can be simpler, less expensive in terms of computational time and numerically more robust than their counterparts. A further approach, to model premixed combustion, is to retain the FSD method and introduce the tabulation of precomputed detailed chemistry through the filtered tabulated chemistry for LES. This is called F-TACLES model and it uses the filter size larger than the grid spacing [18]. Recently Fiorina *et al.* [19] gave a state-of-the-art picture for a set of five modelling approaches for the investigation of stratified combustion. They compared filtered tabulated chemistry model (F-TACLES), combined artificial flame thickening and tabulated chemistry approach, coupled G-equation/progress variable formalism, flame surface density model and no combustion model (LES on a very fine grid). The simulations results were validated with data from the Darmstadt stratified flame series. They found out that most simulation results agree well with the experimental data.

One of the physical aspects that can be exploited, are the fractal characteristics of premixed flames which have been confirmed in several experimental works. The usage of fractal analysis to turbulence began with Mandelbrot's investigation that surfaces of constant properties of a passive scalar in turbulent flows hold fractal character [20], followed by a series of

investigations: see Sreenivasan [21] for a review. Many experimental studies have investigated the fractal character of turbulent premixed flames (e.g. [22]). It has been shown that the fractal analysis provides reasonable estimates of the turbulent flame speed for the assumed values of the cut off scales and the fractal dimension. Several models have been proposed for premixed flames using fractal analysis (e.g. [23,24]). It is assumed that the wrinkled flame front surfaces may be characterized by a fractal surface of dimension D, for a range of length scales between the inner cut off ε_{i} and the outer cut off ε_o, using a power law relation [8,25]. The availability of reliable models for fractal dimension and cut off scales is the key ingredient in the success and the applicability of fractal-based models. In the corrugated flamelet regime, the difference between laminar and turbulent flame speed is mainly due to the increased flame-surface area. The problem of estimation of the flame speed is thus largely dependent on the prediction of that area. In LES, since a major portion of the wrinkled flame front is resolved, the problem is further reduced to the estimation of the unresolved wrinkling. The resolution dependency of the unresolved area is, therefore, critical for proper LES modelling, and this is basically what the fractal analysis can provide.

The turbulent premixed combustion can be characterized by the reaction progress variable $c = (T - T_u)/(T_b - T_u)$, which is a normalised quantity that changes monotonically from 0 in reactants to 1 in completely burned products. The terms which need to be modelled in the Favre-filtered transport equation for the progress variable c correspond to the filtered reaction rate $\overline{\dot{\omega}}$ and the sub-grid turbulent scalar flux $\left(F_i^{sg} = \bar{\rho}\widetilde{u_{\mathrm{i}}c} - \bar{\rho}\widetilde{u}_{\mathrm{i}}\tilde{c}\right)$. The turbulent scalar flux consists of two contributions of entirely different nature, one produced by thermal expansion and the other by turbulent motions. The turbulent transport is of the gradient type for a sufficiently high level of turbulence as the flame is unable to impose its own dynamics to the flow field and the flame front motions are dominated by the turbulence. On the other hand, the turbulent transport is of the counter gradient type when the turbulence level is relatively low, the thermal expansion due to heat release dominates and the flame gets able to impose its own dynamics to the flow field. Traditionally, the sub-grid scalar flux (SGSF) is modelled using a gradient hypothesis. With using the gradient hypothesis based model, the counter gradient subgrid scalar fluxes cannot be explicitly modelled. Theoretical [26,27], experimental [28-33] and Direct Numerical Simulations (DNS) [34-39] studies have shown that the turbulent sub-grid scalar flux (SGSF) can exhibit counter gradient behaviour under some conditions. The SGSF is related to conditional mean

velocities in the Bray-Moss-Libby (BML) model [28] and the counter-gradient diffusion may occur in case when the conditional burned-gas velocity is larger than the unburned-gas counterpart. The counter-gradient diffusion is attributed to differential acceleration of burned and unburned gases due to the pressure gradients across the flame brush. The DNS based analysis by Veynante *et al.* [35] indicated a simple criterion to delineate between the gradient and counter-gradient turbulent transport regimes. This criterion suggests that the counter-gradient (gradient) diffusion is obtained for low (high) values of the ratio of root-mean-square value of turbulent velocity to unstrained laminar flame speed u'/s_L^0 and high (low) values of heat release parameter $\tau = (T_{ad} - T_u)/T_u$ where T_u and T_{ad} are the unburned gas and adiabatic flame temperatures respectively. Pfadler *et al.* [40,41] and Lecocq *et al.* [42] assessed the performances of different possible models of turbulent scalar flux. Recently, Gao *et al.* [43,43] have carried out a detailed assessment of different LES models for turbulent scalar flux for a range of different Lewis numbers based on a-priori analysis of DNS data. They concluded that the SGSF models, which account for the alignment of local resolved velocity and scalar gradients, perform better than the other existing models. The models by Huai *et al.* [45] and Clark *et al.* [46] were found to capture adequately both the qualitative and quantitative behaviours of (F_i^{sg}) for $\Delta > \delta_L^0$ in all cases, where Δ denotes the LES filter width.

The practical industrial devices involving premixed combustion operate under high-pressure conditions with a variety of fuels. In general, a numerical model should be able to account for the influence of pressure and fuel effects on reaction closure to claim its generality. However, quite often, most of the existing SAFSD models have been validated over a small range of conditions mainly limited to atmospheric methane flames. Pressure is known to affect both the turbulent flow field through a change of viscosity and laminar premixed flame structure. Experimentally [47-49], it is observed that as the flame wrinkling increases, the smaller turbulence scales (Taylor scales, Kolmogorov scales) decrease, while the turbulent integral length scale remains nearly unchanged with increment in pressure at constant inlet velocity. This can be explained by the classical turbulence theory. The kinematic viscosity $\nu = \mu/\rho$ is decreased, thus increased pressure brings higher turbulent Reynolds number $Re_t = u' l_0/\nu$ (if the mean bulk velocity is kept constant, typically the turbulence intensity is also weakly influenced by pressure). The smaller turbulence scales are inversely dependent on Re_t, thus measured turbulence energy spectra are shifted to higher frequency region [47]. The laminar flame speed s_L and laminar

flame thickness δ_L also scale with pressure. The pressure scaling for methane and propane fuels are $s_L^0 \propto p^{-0.5}$, $\delta_L \propto p^{-0.5}$ and $s_L^0 \propto p^{-0.25}$, $\delta_L \propto p^{-0.75}$, respectively. The influence of Le number on turbulent reaction rate is explained elaborately in the work of [50]. Le > 1 represents faster heat diffusion away from the flame front compared to the diffusion of species, which may result in reduced flame propagation. So the numerical models, without explicit Le number dependency, might be expected to predict higher values of turbulent flame speed especially at moderate to high turbulence.

The present study uses the concept of algebraic FSD modelling to perform LES and RANS investigations of turbulent premixed combustion at conditions typical for spark-ignition engines and industrial gas turbines. Chakraborty and Klein [51] extensively investigated different algebraic FSD models in a-priori DNS study of freely propagating statistically planar turbulent premixed flames falling in the corrugated flamelet and thin reaction zone regimes and provided a detailed insight into the formulations of the models. The performance of various algebraic FSD models is also investigated by performing LES of the ORACLES burner and Volvo Rig in a recent study by Ma *et al.* [52].

1.2 Motivation and Thesis objectives

In this work, an LES subgrid combustion model, which was derived and validated in a previous work by Keppeler *et al.* [53], has been used (henceforth denoted as Keppeler model). The Keppeler model offers a closure of the combined filtered reaction rate and molecular diffusion term with the help of a fractal based Flame Surface Density (FSD) formulation while the sub-grid turbulent scalar flux is modelled using the conventional gradient transport (GT) approximation. Experimental and DNS databases were used to estimate the fractal parameters, e.g., inner and outer cut off scales, fractal dimension, etc. The validation exercise reported in [53] shows excellent agreement with experimental data from turbulent Bunsen flames over a wide range of u'/s_L^0 and pressures between 1 and 20 bar, at conditions which are typical for spark-ignition engines and industrial gas turbines. The Keppeler model is derived on the basis of Lindstedt and Váos [54] model, which shows a good performance in the context of RANS. However, the latter model neither incorporates the effect of strain on the laminar flame speed nor shows correct behaviour in low Reynolds numbers limit. The new LES model takes into account

the linear theory of instabilities and is extended to cover the low Re regime. In addition, it was shown that the time-averaged turbulent flame speed predicted by the subgrid combustion model is quite robust with respect to changes in grid resolution, meaning that on a coarser grid the modelled subgrid source term increases such that the averaged turbulent flame speed stays approximately constant [53]. This is necessary, since in the high-pressure cases only 20% of the flame folding is resolved in the LES, although 80% of the turbulent kinetic energy is resolved as required for a "good" LES. In contrast, most of the flame wrinkling was resolved in the 1 bar cases [53]. These favourable properties of the Keppeler model prompted the author to choose it as the basis of the present investigation of various features of turbulent premixed combustion of significant importance.

The main objectives of this thesis are:

- In the work [53], a simplified version was proposed but not further investigated. The new model is simpler and without any model constants and blending functions. In the present work the performance of this simplified version is assessed, compared to the original model and validated with the experimental data.
- In the original Keppeler model, the SGSF was modelled using a classical gradient hypothesis [53]. With the model based on the aforementioned assumption, the counter gradient subgrid scalar fluxes cannot be modelled. Theoretical, experimental and Direct Numerical Simulations (DNS) studies have shown that the turbulent subgrid scalar flux (SGSF) can exhibit counter gradient behaviour under some conditions. In the present work, the performance of the original Keppeler model [53] is investigated in conjunction with more refined SGSF modelling, which showed good performance in a DNS based analysis of different SGSF models [43,44].
- Large-scale industrial devices such as internal combustion engines, gas turbine combustors, etc. operate under high-pressure conditions and use a variety of fuels. Contrary to these applications, most of the existing numerical modelling methodologies do not include explicit high-pressure and the Lewis number effects in premixed turbulent combustion. However, a numerical model should include both these effects to claim generality of the model. In the present work, some of the popular SAFSD models

available in open literature are analytically and numerically investigated for pressure and Le number effects in the modelling of premixed flames.

- Several LES combustion models have a direct counterpart in the RANS context. This can provide an advantage as it offers a good basis for the judgement of the strengths and weaknesses of the RANS and LES modelling approaches in the context of turbulent premixed combustion. This motivated to develop a RANS version of the Keppeler model [53] and assess its performance in comparison with the original LES model.

- Lastly, the effects of $|\nabla \bar{c}|$ versus$|\nabla \tilde{c}|$ in the generalized FSD expression are investigated in conjunction with different CGT SGSF models in a 1D formulation.

1.3 Thesis outline

The thesis is comprised of seven chapters. Following the introduction, chapter 2 of the thesis provides the fundamental concepts of fluid mechanics i.e. the governing equations for mass, momentum, energy and scalar transport, the structure of turbulence, some concepts that are commonly encountered in premixed combustion and an overview of different methods used for premixed combustion modelling. Chapter 3 presents the main elements of the finite volume formulation, including the spatial and time advancement schemes and boundary conditions. Chapter 4 describes the combustion models used in the present study. Chapter 5 presents the numerical setup and the experimental database used for the validation of the numerical predictions. Chapter 6 presents a detailed discussion on the obtained results. Finally the conclusions are presented in chapter 7.

Chapter 2

Theoretical background

Turbulent reactive flow involves a strong interaction between heat, mass and energy transfer. The complex interaction between turbulence and chemical reactions further increases the complexity of the problem. In this chapter an overview of the basic elements required for the analysis of turbulent reactive flows is presented. A general overview of the governing equations for reactive flows is presented first. This is followed by the characteristics of turbulence, premixed flames and the approaches used for their reaction rate closure. Lastly the available computation methods are discussed with emphasis placed on LES and RANS methods, which form the basis of this study.

2.1 Governing equations for reactive flows

The problem of a reactive flow can be described by a set of partial differential equations known as the governing equations of mass, momentum, energy, species mass fraction and scalar transport. In this section, a short overview of these equations is presented.

2.1.1 Continuity equation

The continuity equation is based on the statement that mass is a conserved quantity. The three dimensional continuity or mass conservation equation at a point in a compressible fluid under unsteady conditions can be written as:

$$\frac{\partial \rho}{\partial t} + \frac{\partial (\rho u_{\mathrm{i}})}{\partial x_{\mathrm{i}}} = 0 \tag{2.1}$$

where x_{i}, t and u denote the distance in the i-direction, time and flow velocity respectively. Any source term is absent in Eq. (2.1) since mass can neither be created nor be destroyed. The first term on the left hand side (LHS) of Eq. (2.1) shows the change in the density ρ with respect to time while the second term is known as the convective transport which describes the net rate of flow of mass through the control volume.

2.1.2 Momentum equation

The momentum or Navier-Stokes equation is based on the Newton's second law of motion that the resultant force acting on a fluid element equals the time rate of change of the momentum of the element. In Cartesian form, the momentum equation can be written as:

$$\frac{\partial(\rho u_{\mathrm{i}})}{\partial t}+\frac{\partial\left(\rho u_{\mathrm{i}} u_{\mathrm{j}}\right)}{\partial x_{\mathrm{j}}}=\frac{\partial \tau_{\mathrm{ij}}}{\partial x_{\mathrm{j}}}-\frac{\partial p}{\partial x_{\mathrm{i}}}+\rho f_{\mathrm{i}} \tag{2.2}$$

where p, τ_{ij} and f_{i} represent the pressure or normal stress, viscous stresses and external body forces (e.g. gravitational, centrifugal or Coriolis) respectively. The second term on the LHS of Eq. (2.2) represents the convective transport. The viscous stresses τ_{ij} can be written in terms of linear and volumetric deformations using the Newton's law of viscosity:

$$\tau_{\mathrm{ij}}=2\mu S_{\mathrm{ij}}-\frac{2}{3}\,\mu\delta_{\mathrm{ij}}\frac{\partial u_k}{\partial x_k} \tag{2.3}$$

where μ and δ_{ij} are the dynamic viscosity and Kronecker delta ($\delta_{\mathrm{ij}}=1$ if $\mathrm{i}=\mathrm{j}$ and $\delta_{\mathrm{ij}}=0$ otherwise). In Eq. (2.3), S_{ij} represents the strain rate and can be written like this:

$$S_{\mathrm{ij}}=\frac{1}{2}\left(\frac{\partial u_{\mathrm{i}}}{\partial x_{\mathrm{j}}}+\frac{\partial u_{\mathrm{j}}}{\partial x_{\mathrm{i}}}\right) \tag{2.4}$$

Neglecting the body forces and substituting Eq. (2.3) into Eq. (2.2), the momentum equation for a compressible Newtonian fluid becomes:

$$\frac{\partial(\rho u_{\mathrm{i}})}{\partial t}+\frac{\partial\left(\rho u_{\mathrm{i}} u_{\mathrm{j}}\right)}{\partial x_{\mathrm{j}}}=\frac{\partial}{\partial x_{\mathrm{j}}}\left[\mu\left(2S_{\mathrm{ij}}-\frac{2}{3}\,\delta_{\mathrm{ij}}\frac{\partial u_k}{\partial x_k}\right)\right]-\frac{\partial p}{\partial x_{\mathrm{i}}} \tag{2.5}$$

2.1.3 Species mass fraction

A combustion process involves many species and chemical reactions. In order to numerically simulate a reactive flow, a set of species transport equations needs to be solved along with the Navier-Stokes equations for the flow field. The composition of a mixture is usually represented in terms of the constituent mass fractions. The mass fraction of species k, Y_k, is a ratio of the mass of species k and the total mixture mass:

$$Y_k = \frac{m_k}{m_{tot}} \tag{2.6}$$

where k = 1,2,…..N and N is the number of total species. The sum of all the constituent mass fractions must be unity:

$$\sum_{k=1}^{N} Y_k = \sum_{k=1}^{N} \frac{m_k}{m_{tot}} = 1 \tag{2.7}$$

The transport equation for Y_k can be written as:

$$\frac{\partial(\rho Y_k)}{\partial t} + \frac{\partial(\rho u_\mathrm{i} Y_k)}{\partial x_\mathrm{i}} = -\frac{\partial j_\mathrm{i}^k}{\partial x_\mathrm{i}} + \dot{\omega}_k \tag{2.8}$$

The first and second terms on the right-hand side (RHS) of Eq. (2.8) are the diffusive fluxes and the formation rate of species k respectively. Although, the molecular transport processes that form the diffusive fluxes j_i^k are very complex, j_i^k can be estimated using Fick's law:

$$j_i^k = -\rho \alpha_k \frac{\partial Y_k}{\partial x_\mathrm{i}} \tag{2.9}$$

where α_k is the diffusion coefficient of species k.

2.1.4 Conservation of energy

Poinsot and Veynante [55] have discussed various forms of the energy conservation equations. In OpenFOAM, the CFD tool used for the present work, the energy conservation is taken into account by solving a simplified equation for enthalpy $h = h_{tot} - u_\mathrm{i} u_\mathrm{j}/2$:

$$\frac{\partial \rho h}{\partial t} + \frac{\partial \rho u_\mathrm{i} h}{\partial x_\mathrm{i}} = \frac{Dp}{Dt} - \frac{\partial q_\mathrm{i}}{\partial x_\mathrm{i}} + \tau_{ij} \frac{\partial u_\mathrm{i}}{\partial x_\mathrm{j}} + \dot{Q} + \rho u_\mathrm{i} f_\mathrm{i} \tag{2.10}$$

where $\tau_\mathrm{ij}\, \partial u_\mathrm{i}/\, \partial x_\mathrm{j}$, $\dot{Q}$ and $\rho u_\mathrm{i} f_\mathrm{i}$ represent the viscous heating term, the heat source term and the power produced by volume forces f_i respectively. The energy flux q_i is the sum of a heat diffusion given by the Fourier's law and the diffusion of species given by Fick's law (Eq. (2.9)):

$$q_i = -\lambda \frac{\partial T}{\partial x_\mathrm{i}} - \sum_{k=1}^{N} h_k\, \rho \alpha_k \frac{\partial Y_k}{\partial x_\mathrm{i}} \tag{2.11}$$

The relationship between h and h_k is defined as:

$$h = \sum_{k=1}^{N} Y_k \, h_k \tag{2.12}$$

Equation (2.11) is often written in term of a gradient of h [56, 57]:

$$q_{\mathrm{i}} = -\frac{\lambda}{C_p}\frac{\partial h}{\partial x_{\mathrm{i}}} + \mu \sum_{k=1}^{N} \left(\frac{\lambda}{\rho C_p \alpha_k} - 1 \right) \frac{1}{Sc_k} h_k \frac{\partial Y_k}{\partial x_{\mathrm{i}}} \tag{2.13}$$

where $\lambda / \rho C_p \alpha_k$ is known as the Lewis number (Le_k) which is a ratio of thermal diffusion to mass or species diffusion. Sc_k is the Schmidt number which is defined as a ratio of momentum diffusivity to species diffusivity:

$$Le_k = \frac{\lambda}{\rho C_p \alpha_k} = \frac{\alpha_{th}}{\alpha_k} \tag{2.14}$$

$$Sc_k = \frac{\mu}{\rho \alpha_k} \tag{2.15}$$

If the fluid is assumed to be an ideal gas, the thermodynamic variables ρ, p and T can be related using the ideal gas equation of state:

$$p = \rho R T \sum_{k=1}^{N} \frac{Y_k}{M_k} \tag{2.16}$$

The relationship between enthalpy and temperature is defined as:

$$h_k = h_{k,0} + \int_{T_0}^{T} C_{p,k} \, dT \tag{2.17}$$

The specific heat capacity $C_{p,k}$ is estimated with the following fit polynomial:

$$C_{p,k} = \frac{R}{M_k} \left(a_0 + a_1 T + a_2 T^2 + a_3 T^3 + a_4 T^4 \right) \tag{2.18}$$

Substituting Eq. (2.18) into Eq. (2.17) and after integrating, it is possible to calculate h_k:

$$h_k = h_{k,0} + \frac{R}{M_k} \left(a_0 T + \frac{a_1}{2} T^2 + \frac{a_2}{3} T^3 + \frac{a_3}{4} T^4 + \frac{a_4}{5} T^5 \right) \tag{2.19}$$

The coefficients in Eq. (2.18) and (2.19) are calculated from the JANAF tables provided in [58]. The temperature dependence of the molecular viscosity μ is estimated using the Sutherland model:

$$\mu = \frac{A_s T^{0.5}}{1 + T_s T^{-1}} \tag{2.20}$$

For air $A_s = 1.485 * 10^{-6}$ kg/msK$^{0.5}$ and $T_s = 110.4\ K$.

2.1.5 Scalar transport equation

To properly characterize a chemically reactive flow, a transport equation for scalar is required in addition to the mass, momentum and energy equations. The transport equation for an arbitrary scalar Q (the mass fraction or progress variable in premixed combustion) takes the following form:

$$\frac{\partial(\rho Q)}{\partial t} + \frac{\partial(\rho Q u_\mathrm{i})}{\partial x_\mathrm{i}} = \frac{\partial}{\partial x_\mathrm{i}}\left(\rho\alpha \frac{\partial Q}{\partial x_\mathrm{i}}\right) + \dot{S}_Q \tag{2.21}$$

where the temporal change and convective transport of the scalar are represented by the two terms on the LHS of Eq. (2.21) while the two terms on the RHS denote the molecular diffusion of Q assuming Fick's second law of diffusion with diffusivity α and the source term describing the production or destruction of the scalar respectively.

A turbulent low-speed premixed flame can be expressed using a transport equation for the progress variable c [2,55]. This is a normalized quantity which takes a value equal to zero for unburned reactants and unity for fully burned products. The progress variable c can be defined in terms of mass fraction Y_k or temperature T, the present work applies the latter:

$$c = \frac{T - T_u}{T_b - T_u} \tag{2.22}$$

where subscripts 'u' and 'b' denote unburnt and burnt states. This implies a one-step irreversible chemical reaction and the temperature is raised from T_u to T_b as a result of the corresponding heat release. Under the assumptions of low Mach number Ma, unity Le number and in the absence of heat losses, the transport equation for c takes the following form:

$$\frac{\partial(\rho c)}{\partial t} + \frac{\partial(\rho c u_{\mathrm{i}})}{\partial x_{\mathrm{i}}} = \frac{\partial}{\partial x_{\mathrm{i}}}\left(\rho\alpha \frac{\partial}{\partial x_{\mathrm{i}}}\right) + \dot{\omega} \tag{2.23}$$

With the algebraic FSD method, the problem of premixed combustion involving homogenous mixtures at low velocities can be described with a set of transport equations of mass, momentum, energy, progress variable and the equation of state.

2.2 Turbulence

In this section, a short overview of the basics of turbulence and its modelling techniques is presented.

2.2.1 Turbulence definition and description

The turbulence is characterized by apparent random unsteadiness associated with the fluid velocity at each point in the flow. It results when viscous actions are not sufficient to properly damp the instabilities formed in a flow. There is no complete definition of turbulence as it is among the least-known physical processes. A turbulent flow is:

- irregular
- diffusive
- rotational
- dissipative
- characterized by a wide range of scales

and a purely continuum phenomenon featuring fluid flows as even the smallest scales in a turbulent flow are typically far larger than any molecular length scale. The random fluctuations in a turbulent flow result in enhanced mixing, that increases the rate of mass, momentum and energy transfer. This feature plays an important role in the reactive flows and can increase the combustion rate.

The transition of a flow from laminar to turbulent state can be indicated by the Reynolds number, which is interpreted as the ratio of inertia and viscous forces:

$$Re = \frac{F_I}{F_V} = \frac{\rho U^2/L}{\mu U/L^2} = \frac{\rho UL}{\mu} = \frac{UL}{\nu} \tag{2.24}$$

where U, L and ν denote the characteristic velocity, length scale and kinematic viscosity. The existence of laminar or turbulent flow through a particular system or geometry can be found by comparing this dimensionless parameter against the critical value Re_{crit}. For a pipe flow the typical value Re_{crit} is 2300 when L is taken to be the pipe diameter.

One particularly useful approach to characterize turbulent flows quantitatively is Reynolds decomposition approach. In this method, any turbulent flow property is decomposed into mean and fluctuating components. For example, denoting the instantaneous, mean and fluctuating velocities by u_i, $\bar{u}_i$ and u_i', respectively, we can write for the instantaneous velocity:

$$u_i(t) = \bar{u}_i + u_i'(t) \tag{2.25}$$

Here, the mean component is calculated by time averaging over a sufficiently large time interval. In turbulent reactive flows, large random fluctuations in species, density and temperature fields are also observed, as defined by:

$$Y_k(t) = \bar{Y}_k + Y_k'(t);\ \ \rho(t) = \bar{\rho} + \rho'(t);\ \ T = \bar{T}\ + T'(t) \tag{2.26}$$

2.2.2 Turbulent scales

For a turbulent flow many length scales have been defined, however, two of them are frequently cited. In the order of decreasing size, these scales are integral scale l_0 and Kolmogorov scale l_η. The large eddies in a turbulent flow contain the most energy and have length scales that are limited by the flow geometry. The size of eddies l can be related to wave number κ, by $\kappa = 2\pi/l$, which shows that small wave number eddies correspond to large eddies in a turbulent flow. The integral length scale l_0 physically characterizes the mean size of these eddies. It is always smaller than the largest length scale in the system but has same order of magnitude. On the other hand, the Kolmogorov scale l_η represents the smallest scale associated with a turbulent flow. At this length scale, the viscous forces are dominant and the dissipation of turbulent kinetic energy to fluid internal energy occurs. The Kolmogorov length, velocity and time scales as a

function of kinematic viscosity and the kinetic energy dissipation rate can be derived by a dimensional analysis and are given by [59]:

$$l_\eta = \left(\frac{\nu^3}{\epsilon}\right)^{1/4} ; \qquad u_\eta = (\nu\epsilon)^{1/4} ; \qquad t_\eta = \left(\frac{\nu}{\epsilon}\right)^{1/2} \tag{2.27}$$

The rate of dissipation of turbulent kinetic energy ϵ can be approximated as:

$$\epsilon = \frac{u'^3}{l_0} \tag{2.28}$$

where u' is the turbulence intensity corresponding to the size of eddy l_0. The turbulent Reynolds number based on u' and l_0 can be defined as:

$$Re_{l_o} = \frac{u' l_0}{\nu} \tag{2.29}$$

Equations (2.27) and (2.28) defining the integral length scale and the dissipation rate can be combined with Eq. (2.29) to relate the smallest (l_η) and largest length (l_0) scales:

$$l_\eta = l_0 {Re_{l_o}}^{-3/4} \tag{2.30}$$

Equation (2.30) shows that for a fixed l_0, the small-scale turbulence becomes increasingly finer with increasing Re, leading to a greater range of scales that would increase the mixing in a turbulent flow field.

2.2.3 Energy cascade

The eddies with a size of the order of integral length scale l_0 carry most of the turbulent kinetic energy k, which can be defined as:

$$k = \frac{1}{2}\left(\overline{u_\mathrm{i}' u_\mathrm{i}'}\right) \tag{2.31}$$

For homogenous isotropic turbulence, it becomes $k = 3\overline{u_\mathrm{i}'^2}/2$, where i = x, y or z. Eddies of different sizes exist in a turbulent flow. This is because of the fact that the large eddies have a tendency of continuously breaking up into smaller eddies, which in turn break up into even smaller eddies. This process is continued until the viscous forces become dominant and the

smallest eddies are dissipated. An external source would be needed to make up for the loss of kinetic energy and sustain a turbulent flow. In the absence of external energy source, the turbulence would have a decaying trend of turbulent kinetic energy. This phenomenon of energy transfer from the large scale eddies to the small scale eddies is known as the energy cascade [59] and is illustrated in Fig. 2.1. Figure 2.2 shows a log-log plot of the energy spectrum $E(\kappa)$ of homogenous, isotropic turbulence versus the wave number κ or the reciprocal of the eddy size. The region bounded between the integral length scale and the Kolmogorov length scale is called the inertial subrange, which is characterized by a constant rate of energy transfer with a slope of $-5/3$.

2.3 Computational modelling approaches

In order to describe a reacting flow the continuity (Eq. (2.1)), momentum (Eq. (2.3)) and reactive scalar (Eq. (2.21)) equations need to be solved. However, in most practical applications the analytical solution is difficult to achieve. One way is to solve these equations numerically using computational modelling approaches. The three main computational approaches are Reynolds-averaged Navier-Stokes (RANS), Large Eddy Simulation (LES) and Direct Numerical Simulation (DNS). The choice of the suitable method is decided by the characteristics of the flow and geometry, the purpose of simulation, required accuracy and the computational power. The RANS method is commonly used in industry, but with the increased availability of computational power and advantage of providing more details about the flow problems, LES is becoming a popular practical option. On the other hand, the application of DNS is still limited by

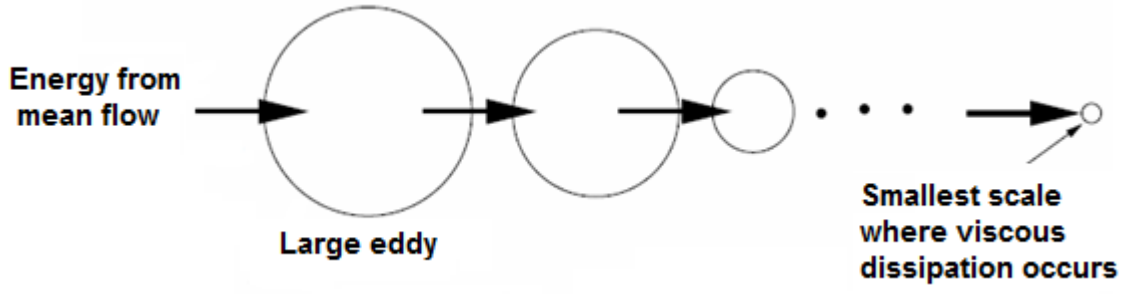

Figure 2.1: Schematic representation of energy cascade [61]

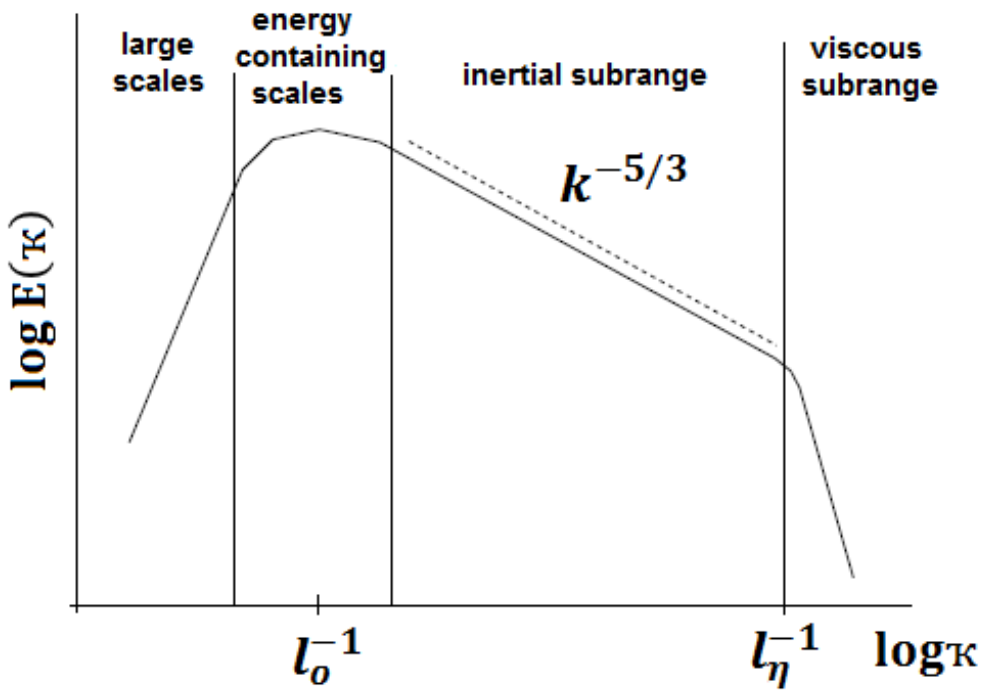

Figure 2.2: Turbulence energy spectrum plotted as a function of wave number

the current and foreseeable computational recourses to small and moderate Re number flows. In this section a short description of the three methods is presented.

2.3.1 Direct Numerical Simulation (DNS)

Direct Numerical Simulation can be claimed to obtain a complete and accurate description of a turbulent flow as it resolves all the length and time scales from the largest to the finest Kolmogorov scales and hence, modelling is not required. After the experimental results, the DNS results are widely trusted and used to validate the prediction obtained with the RANS and LES methods. However, a DNS study for a flow through a practical system requires a huge amount of computational time and resources. High order discretization schemes are required to reduce the numerical errors in the estimation of the governing equations. The selection of appropriate turbulence boundary conditions also demands considerable attention. Although, the computational resources and techniques have experienced a rapid increase and development in recent years, even with the currently available computational power the DNS method can still be applied only to low and moderate Re number flows involving simple geometries.

2.3.2 Reynolds-averaged Navier-Stokes (RANS) Method

As mentioned earlier, RANS method is the most commonly used numerical technique for industrial applications. Contrary to DNS, it models all turbulent structures in the energy spectrum. In this method, the grid size is significantly greater than DNS giving faster and cheaper numerical results. However, only averaged flow fields can be obtained as a solution. To obtain all the governing equations in the Reynolds-averaged form, each flow variable is decomposed into mean and fluctuating components using the Reynolds decomposition method and then time-averaging is applied to each term in the equation over a sufficiently large time interval $\Delta t = t_2 - t_1$. Time averaging applied to any flow property q is given by:

$$\bar{q} = \lim_{\Delta t \to \infty} \frac{1}{\Delta t} \int_{t_1}^{t_2} q(t) dt \; ; q(t) = \; \bar{q} + q'(t) \tag{2.32}$$

For unsteady cases, the averaging method needs to be redefined as ensemble average to account for the time dependence of mean quantities. When the Reynolds-averaging method, as defined in Eq. (2.32), is applied to a reactive flow that features changes in the density, the correlations of density and velocity fluctuations are formed, which need additional modelling. Such complications can be avoided by using Favre-averaging (density weighted averaging) for any flow property q of reactive flows:

$$\tilde{q} = \frac{\overline{\rho q}}{\bar{\rho}}; \; q(t) = \; \tilde{q} + q'(t); \quad \widetilde{q'} = 0; \quad \tilde{\tilde{q}} = \tilde{q} \tag{2.33}$$

Substitution of Eq. (2.33) into mass, momentum, species and energy equations result in the well-known Favre-averaged Navier Stokes Equations:

$$\frac{\partial \bar{\rho}}{\partial t} + \frac{\partial (\bar{\rho} \tilde{u}_\mathrm{i})}{\partial x_\mathrm{i}} \; = 0 \tag{2.34}$$

$$\frac{\partial (\bar{\rho} \tilde{u}_\mathrm{i})}{\partial t} + \frac{\partial \left(\bar{\rho} \tilde{u}_\mathrm{i} \tilde{u}_\mathrm{j}\right)}{\partial x_\mathrm{j}} = \frac{\partial \left(\overline{\tau}_\mathrm{ij} - \bar{\rho} \widetilde{u'_\mathrm{i} u'_\mathrm{j}}\right)}{\partial x_\mathrm{j}} - \frac{\partial \bar{p}}{\partial x_\mathrm{i}} + \overline{\rho f_\mathrm{i}} \tag{2.35}$$

$$\frac{\partial \left(\bar{\rho} \widetilde{Y_k}\right)}{\partial t} + \frac{\partial \left(\bar{\rho} \tilde{u}_\mathrm{i} \widetilde{Y_k}\right)}{\partial x_\mathrm{i}} = -\frac{\partial \overline{J_\mathrm{i}^k}}{\partial x_\mathrm{i}} - \frac{\partial \left(\bar{\rho} \widetilde{u'_\mathrm{i} Y'_k}\right)}{\partial x_\mathrm{i}} + \overline{\dot{\omega}_k} \tag{2.36}$$

$$\frac{\partial(\bar{\rho}\tilde{h})}{\partial t}+\frac{\partial(\bar{\rho}\tilde{u}_{\mathrm{i}}\tilde{h})}{\partial x_i}=\frac{\overline{Dp}}{Dt}-\frac{\partial(\bar{\rho}\widetilde{u'_{\mathrm{i}}h'})}{\partial x_{\mathrm{i}}}-\frac{\partial\bar{q}_{\mathrm{i}}}{\partial x_i}+\overline{\tau_{\mathrm{ij}}\frac{\partial u_{\mathrm{i}}}{\partial x_{\mathrm{j}}}}+\bar{\dot{Q}}+\overline{\rho u_{\mathrm{i}}f_{\mathrm{i}}} \tag{2.37}$$

There are two major consequences of the averaging process. First, the fine details of the flow are eliminated and secondly, some new terms appear in the time-averaged equations that are not present in the original time-dependent governing equations. For example, in the time-averaged momentum equation an additional term $\widetilde{u'_{\mathrm{i}}u'_{\mathrm{j}}}$ appears, which represents turbulent stresses or Reynolds stresses. The method to calculate or approximate these stresses or any other additional unknowns that appeared because of the averaging process is termed as the closure problem. The closure of the Reynolds stress tensor can be achieved by either the eddy viscosity concept as proposed by Boussinesq [61] or by solving a transport equation for the Reynolds stresses. The latter method is numerically more demanding as it offers the challenge of solving more unknown closure terms. The zero-equation model, one-equation model or two-equation models are based on the Boussinesq approximation and they offer the modelling of eddy viscosity. The zero-equation model is based on mixing length hypothesis as proposed by Prandtl [62], which represent the eddy viscosity as a product of characteristic turbulent velocity, fluid density and a length scale called the mixing length. The one-equation model solves an additional transport equation for turbulent kinetic energy k, whereas the two-equation models solve the combination of either k and ϵ, or k and ω. The energy and scale of the turbulence are determined by the variable k and ϵ (turbulent dissipation) or ω (specific dissipation), respectively. Among these three types of models, the two-equation models are commonly used. The $k-\epsilon$ and SST $k-\omega$ models, the most popular two-equation models, are explained in detail.

2.3.2.1 $k-\epsilon$ Two-equation model

The $k-\epsilon$ model represents the turbulent flow properties by solving two additional transport equations for k and ϵ. Several formulations of this model are available, starting from the earliest development effort of Chou [63] to the formulation of Launder and Sharma [64]. The form of the model presented in [64] is mostly used and typically referred as the Standard $k-\epsilon$ model. The $k-\epsilon$ model has shown very good performance for many industrial relevant flows. The model gives satisfactory performance in thin shear layer flow problems with relatively small pressure

gradients and in confined flows where the Reynolds shear stresses are dominant. The implementation of $k-\epsilon$ model in OpenFOAM for compressible flow is given by:

$$\frac{\partial(\rho k)}{\partial t}+\frac{\partial(\rho u_i k)}{\partial x_i}=P_k-\rho\epsilon+\frac{\partial}{\partial x_i}\left[\left(\mu+\frac{\mu_t}{\sigma_k}\right)\frac{\partial k}{\partial x_i}\right] \tag{2.38}$$

$$\frac{\partial(\rho \epsilon)}{\partial t}+\frac{\partial(\rho u_i \epsilon)}{\partial x_i}=C_{1\epsilon}\frac{\epsilon}{k}P_k-C_{2\epsilon}\rho\frac{\epsilon^2}{k}+\frac{\partial}{\partial x_i}\left[\left(\mu+\frac{\mu_t}{\sigma_\epsilon}\right)\frac{\partial \epsilon}{\partial x_i}\right] \tag{2.39}$$

$$\mu_t=C_\mu\rho\frac{k^2}{\epsilon},\quad l_0=\frac{{C_\mu}^{3/4}k^{3/2}}{\epsilon} \tag{2.40}$$

where $P_k=2\mu_t S_{\mathrm{ij}}S_{\mathrm{ij}}$ is the production of turbulence. The constants used in the model are:

$$C_{1\epsilon}=1.44;\quad C_{2\epsilon}=1.92;\quad C_\mu=0.09;\quad \sigma_k=1;\quad \sigma_\epsilon=1.3 \tag{2.41}$$

2.3.2.2 SST $k-\omega$ Two-equation model

The standard $k-\epsilon$ has shown only moderate agreement in free turbulent flows e.g. wake, mixing layer and free jet flows. The model severely over-predicts the spreading rate of axisymmetric jets in stagnant surroundings. The model also does not show satisfactory performance in low Re number flows, flows with high spatial gradients and flows with an adverse pressure gradient, recirculation regions, large extra strains or stress anisotropy. The $k-\omega$ model presented by [65], eliminates most of the problems observed with the $k-\epsilon$ model as it can be directly used in the near wall regions without any need of wall-damping functions in low Re number applications. However, this model also has a drawback that its performance is greatly dependent on the assumed free stream turbulence properties. This led to the development of SST $k-\omega$ model [66,67] which combines the best features of the $k-\epsilon$ and $k-\omega$ models. This is a hybrid model which activates the standard $k-\epsilon$ in the fully turbulent region far from the wall and the $k-\omega$ model in the near wall region. The implementation of SST $k-\omega$ model in OpenFOAM for compressible flow is given by:

$$\frac{\partial(\rho k)}{\partial t}+\frac{\partial(\rho u_i k)}{\partial x_i}=\widetilde{P_k}-\beta^*\rho\omega k+\frac{\partial}{\partial x_i}\left[\left(\mu+\frac{\mu_t}{\sigma_{k1}}\right)\frac{\partial k}{\partial x_i}\right] \tag{2.42}$$

$$\frac{\partial(\rho \omega)}{\partial t}+\frac{\partial(\rho u_i \omega)}{\partial x_i}=\frac{\gamma}{\nu_t}P_k-\beta\rho\omega^2+\frac{\partial}{\partial x_i}\left[\left(\mu+\frac{\mu_t}{\sigma_{\omega1}}\right)\frac{\partial k}{\partial x_i}\right]+(1-F_1)\,2\rho\sigma_{\omega2}\frac{1}{\omega}\frac{\partial k}{\partial x_i}\frac{\partial \omega}{\partial x_i} \tag{2.43}$$

$$P_k = \tau_{ij}\frac{\partial u_{\mathrm{i}}}{\partial x_{\mathrm{i}}};\quad \widetilde{P_k} = min(P_k, c_l\epsilon);\quad \mu_t = \frac{a_1 k}{max\left(a_1\omega, \sqrt{2}SF_2\right)};\quad S = \sqrt{S_{\mathrm{ij}}S_{\mathrm{ij}}} \tag{2.44}$$

$$F_1 = tanh(arg_1^4);\quad F_2 = tanh(arg_2^2);\quad \tau_{ij} = \mu_t\left(\frac{\partial u_{\mathrm{i}}}{\partial x_{\mathrm{j}}} + \frac{\partial u_{\mathrm{j}}}{\partial x_{\mathrm{i}}} - \frac{2}{3}\frac{\partial u_k}{\partial x_k}\right) - \frac{2}{3}\rho k\delta_{\mathrm{ij}} \tag{2.45}$$

$$arg_1 = min\left[max\left[\frac{\sqrt{k}}{\beta^*\omega y}, \frac{500\nu}{y^2\omega}\right], \frac{4\rho\sigma_{\omega 2}k}{CD_{k\omega}y^2}\right];\ CD_{k\omega} = max\left[2\rho\sigma_{\omega 2}\frac{1}{\omega}\frac{\partial k}{\partial x_i}\frac{\partial \omega}{\partial x_i}, 1e^{-10}\right] \tag{2.46}$$

$$arg_2 = max\left[2\frac{\sqrt{k}}{\beta^*\omega y}, \frac{500\nu}{y^2\omega}\right],\quad l_0 = \frac{{C_\mu}^{-1/4}k^{1/2}}{\omega} \tag{2.47}$$

The transformation between the $k-\omega$ and $k-\epsilon$ models is obtained using $\varphi = F_1\varphi_1 + (1-F_1)\varphi_2$, where φ_1, φ_2 stand for the coefficients of the $k-\omega$ and $k-\epsilon$ models respectively. The constants used in the model are:

$$\sigma_{k1} = 1.176,\ \sigma_{\omega 1} = 2.000,\ \kappa = 0.41,\quad \gamma_1 = 0.5532,\quad \beta_1 = 0.0750,\quad \beta^* = 0.09,\ c_l = 10$$

$$\sigma_{k2} = 1.000,\ \sigma_{\omega 2} = 1.168,\ \kappa = 0.41,\quad \gamma_2 = 0.4403,\quad \beta_2 = 0.0828,\quad \beta^* = 0.09 \tag{2.48}$$

2.3.3 Large Eddy Simulation (LES)

An intermediate method between RANS and DNS is known as Large Eddy Simulation (LES) method. The essence of this technique is that the larger eddies need to be filtered out and resolved directly while only the smaller eddies, which are nearly isotropic and have a universal behaviour with sizes below the defined filter width, should be modelled. This is contrary to the RANS method where all the turbulent structures are modelled. Instead of the time-averaging process used in the RANS method, a spatial filtering procedure is used to separate the smaller and larger eddies in the LES method. Due to spatial filtering, the information related to the smaller or filtered-out turbulent structures is lost. This and the effects of interactions between the smaller unresolved turbulent structures and the larger resolved ones produce the subgrid scale (SGS) stresses and need to be modelled by means of a subgrid scale model. For reactive flows, the SGS modelling becomes more difficult since the chemical reactions are characterized by propagating surfaces that are much thinner than the typical filter width. Thus the turbulence-chemistry interactions demand considerable attention and need to be modelled entirely. In the

following paragraphs the filtering process will be described first and then the LES filtered equations will be presented.

2.3.3.1 LES filtering

In LES the spatial filtering operation is applied by means of a filter function $F(\vec{x}-\vec{x}^*)$ as follows [68]:

$$\bar{q}(\vec{x}) = \int_{-\infty}^{+\infty} q\,(\vec{x}^*)\,F(\vec{x}-\vec{x}^*)d\vec{x}^* \tag{2.49}$$

In three-dimensional LES computations, the commonly used spatial filters are:

- Top-hat or box filter:

$$F(\vec{x}) = F(x_i) = \begin{cases} 1/\Delta^3, & \text{if} |x_i| \le \dfrac{\Delta}{2}, \text{i} = 1,2,3 \\ 0, & otherwise \end{cases} \tag{2.50}$$

- Gaussian filter:

$$F(\vec{x}) = F(x_i) = \left(\frac{6}{\pi\Delta^2}\right)^{3/2} exp\left[-\frac{6}{\Delta^2}(x_1^2 + x_2^2 + x_3^2)\right] \tag{2.51}$$

Where (x_1, x_2, x_3) represent the spatial coordinates of the location $\vec{x}$ and Δ is the filter width. The filter functions are defined such that their integral over the whole domain is equal to 1:

$$\int_{-\infty}^{+\infty}\int_{-\infty}^{+\infty}\int_{-\infty}^{+\infty} F(x_1, x_2, x_3)dx_1\,dx_2dx_3 = 1 \tag{2.52}$$

For reactive flows, a density weighted Favre filtering process can be applied as:

$$\bar{\rho}\tilde{q}(\vec{x}) = \int_{-\infty}^{+\infty} \rho q\,(\vec{x}^*)\,F(\vec{x}-\vec{x}^*)d\vec{x}^* \tag{2.53}$$

For anisotropic grids, the size of the filter width can be calculated as $\Delta = \left(\Delta_{x_1}\Delta_{x_2}\Delta_{x_3}\right)^{1/3}$.

2.3.3.2 LES filtered governing equations

By applying the spatial filtering procedure defined above, the LES-filtered equations for mass, momentum, species, and energy can be obtained:

$$\frac{\partial \bar{\rho}}{\partial t} + \frac{\partial (\bar{\rho}\widetilde{u_{\mathrm{i}}})}{\partial x_{\mathrm{i}}} = 0 \tag{2.54}$$

$$\frac{\partial (\bar{\rho}\widetilde{u_{\mathrm{i}}})}{\partial t} + \frac{\partial \left(\bar{\rho}\widetilde{u_{\mathrm{i}}}\widetilde{u_{\mathrm{j}}}\right)}{\partial x_{\mathrm{j}}} = -\frac{\partial}{\partial x_{\mathrm{j}}}\left[\bar{\rho}\left(\widetilde{u_{\mathrm{i}}\,u_{\mathrm{j}}} - \widetilde{u_{\mathrm{i}}}\widetilde{u_{\mathrm{j}}}\right)\right] + \frac{\partial \bar{\tau}_{\mathrm{ij}}}{\partial x_{\mathrm{j}}} - \frac{\partial \bar{p}}{\partial x_{\mathrm{i}}} + \overline{\rho f_{\mathrm{i}}} \tag{2.55}$$

$$\frac{\partial \left(\bar{\rho}\widetilde{Y_k}\right)}{\partial t} + \frac{\partial \left(\bar{\rho}\widetilde{u_{\mathrm{i}}}\widetilde{Y_k}\right)}{\partial x_{\mathrm{i}}} = -\frac{\partial}{\partial x_{\mathrm{i}}}\left[\bar{\rho}\left(\widetilde{u_{\mathrm{i}}\,Y_k} - \widetilde{u_{\mathrm{i}}}\widetilde{Y_k}\right)\right] - \frac{\partial \overline{J_{\mathrm{i}}^{k}}}{\partial x_{\mathrm{i}}} + \overline{\dot{\omega}_k} \tag{2.56}$$

$$\frac{\partial \left(\bar{\rho}\tilde{h}\right)}{\partial t} + \frac{\partial \left(\bar{\rho}\widetilde{u_{\mathrm{i}}}\tilde{h}\right)}{\partial x_i} = -\frac{\partial}{\partial x_{\mathrm{i}}}\left[\bar{\rho}\left(\widetilde{u_{\mathrm{i}}h} - \widetilde{u_{\mathrm{i}}}\tilde{h}\right)\right] + \frac{\overline{Dp}}{Dt} - \frac{\partial \bar{q}_{\mathrm{i}}}{\partial x_i} + \overline{\tau_{\mathrm{ij}}\frac{\partial u_{\mathrm{i}}}{\partial x_{\mathrm{j}}}} + \bar{\dot{Q}} + \overline{\rho u_{\mathrm{i}} f_{\mathrm{i}}} \tag{2.57a}$$

where

$$\frac{\overline{Dp}}{Dt} = \frac{\partial \bar{p}}{\partial t} + \overline{u_{\mathrm{i}}\frac{\partial p}{\partial x_{\mathrm{i}}}} \tag{2.57b}$$

The LES-filtered governing equations look similar to RANS equations with the difference that the overbar indicates spatially filtered flow variables. In Eqs. (2.55)-(2.57) the following terms need suitable closure models as discussed below:

2.3.3.3 Modelling of Reynolds stresses $\left(\widetilde{u_{\mathrm{i}}\,u_{\mathrm{j}}} - \widetilde{u}_{\mathrm{i}}\widetilde{u}_{\mathrm{j}}\right)$

The first term on RHS side of Eq. (2.55) is known as subgrid scale stresses and they are caused by the convective momentum transfer due to interactions of unresolved eddies. These stresses are modelled with a so-called SGS turbulence model. The closure of the SGS stress tensor can be obtained with a variety of methods, most of which use the local resolved velocity field. The eddy viscosity models, which are commonly used in the LES computations, describe the dissipation of energy from large to small scales through SGS viscous effects. These models are based on the Bousinessq approximation and assume a constant SGS eddy viscosity to represent SGS stresses in terms of resolved-flow strain rate. The commonly used eddy viscosity SGS models are the Smagorinsky model [69], the dynamic Smagorinsky model [70], one-equation eddy viscosity model [71], etc. The last of these models, as developed by Schumann [71] and further investigated by Fureby *et al.* [72], is used in the present work to close the SGS stresses. The one-equation eddy viscosity model solves an additional transport for the SGS turbulent kinetic energy k_{sgs}.

$$\frac{\partial \bar{\rho} k_{sgs}}{\partial t} + \frac{\partial \left(\bar{\rho} \widetilde{u_{\mathrm{i}}} k_{sgs}\right)}{\partial x_{\mathrm{i}}} - \frac{\partial}{\partial x_{\mathrm{i}}}\left(\mu_{eff} \frac{\partial k_{sgs}}{\partial x_{\mathrm{i}}}\right) = -\bar{\rho} S_{ij} B_{ij} - C_e \bar{\rho} \frac{{k_{sgs}}^{\frac{3}{2}}}{\Delta} \tag{2.58}$$

$$B_{ij} = \frac{2}{3} k_{sgs} \delta_{\mathrm{ij}} - 2\nu_{sgs}\left\{S_{ij} - \frac{1}{3} tr\left(S_{ij}\right)\delta_{ij}\right\}; \quad \mu_{sgs} = C_k \bar{\rho} \sqrt{k_{sgs}}\Delta \; ; \nu_{sgs} = C_k \sqrt{k_{sgs}}\Delta \tag{2.59}$$

where $\mu_{eff} = \mu + \mu_{sgs}$ is the effective viscosity with μ_{sgs} and ν_{Δ} being eddy dynamic and kinematic viscosities respectively. In the present analysis the model coefficients C_e and C_k are taken to be 1.05 and 0.095 respectively. The sub-grid turbulent kinetic energy transport equation does not explicitly account for pressure dilatation effects (such a model is yet to be introduced in existing literature) but dilatation effects are implicitly included in the production and dissipation mechanisms of sub-grid turbulent kinetic energy transport equation. Although, the computational cost is increased by solving an additional equation, the method offers few advantages over the Smagorinsky model. The non-equilibrium effects in production and dissipation of k_{sgs} are accounted for and the model makes sure that the SGS stresses disappear for laminar flow as $k_{sgs} \to 0$.

2.3.3.4 Modelling of species fluxes $\left(\widetilde{u_{\mathrm{i}} Y_k} - \widetilde{u_{\mathrm{i}}} \widetilde{Y_k}\right)$ and enthalpy fluxes $\left(\widetilde{u_{\mathrm{i}} h} - \widetilde{u_{\mathrm{i}}} \tilde{h}\right)$

The gradient hypothesis based model is commonly used to model turbulent fluxes of the unresolved fine structures:

$$\widetilde{u_{\mathrm{i}} Y_k} - \widetilde{u_{\mathrm{i}}} \widetilde{Y_k} = -\frac{\nu_{sgs}}{Sc_t} \frac{\partial \widetilde{Y_k}}{\partial x_{\mathrm{i}}} \tag{2.60}$$

$$\widetilde{u_{\mathrm{i}} h} - \widetilde{u_{\mathrm{i}}} \tilde{h} = -\frac{\nu_{sgs}}{Pr_t} \frac{\partial \tilde{h}}{\partial x_{\mathrm{i}}} \tag{2.61}$$

The values of Sc_t and Pr_t are based on experience and chosen between 0.5-1.

2.3.3.5 Modelling of filtered laminar diffusion fluxes $\overline{J_{\mathrm{i}}^k}$

The filtered laminar diffusion flux for species $\overline{J_{\mathrm{i}}^{k}}$ can be modelled using a simple gradient assumption i.e. $\bar{\rho}\,\overline{\alpha_k}\partial\widetilde{Y_k}/\partial x_{\mathrm{i}}$.

2.3.3.6 Modelling of pressure velocity term $\overline{u_{\mathrm{i}}(\partial p/\partial x_{\mathrm{i}})}$

The pressure velocity term $\overline{u_{\mathrm{i}}(\partial p/\partial x_{\mathrm{i}})}$ is usually modelled as $\widetilde{u_{\mathrm{i}}}(\partial\bar{p}/\,\partial \mathrm{x_i})$.

2.3.3.7 Modelling of filtered reaction rate $\overline{\dot{\omega}_k}$

The modelling of filtered reaction rate is discussed in detail in section 2.5.

2.4 Basics of Premixed Combustion

Combustion can be broadly classified as premixed combustion and non-premixed (or diffusion) combustion. These two broad classes of combustion are distinguished by the state of mixedness of the reactants. In premixed combustion, the oxidizer and fuel are mixed perfectly before the occurrence of a chemical reaction. The premixed flame is characterized by the propagation of a thin reaction zone, usually referred to as a flame, converting the reactants into hot products of combustion and leading to temperature and pressure rise in the direction of flame propagation. The premixed flames can also be classified according to the flow characteristics as laminar or turbulent flames. The turbulence results in the increased flame surface area, leading to faster flame propagation and consumption of the reactants. In this section, some basic concepts and different modelling methods of premixed combustion will be discussed.

2.4.1 Rate of chemical reaction

A chemical reaction may involve several species and many elementary reactions. For a chemical reaction with N species reacting through M elementary reactions, one can write for jth species in the ith reaction:

$$\sum_{\mathrm{j}=1}^{N} \vartheta'_{\mathrm{ji}} X_{\mathrm{j}} \leftrightharpoons \sum_{\mathrm{j}=1}^{N} \vartheta''_{\mathrm{ji}} X_{\mathrm{j}} \qquad for\ \mathrm{i} = 1,2,\ldots\ldots,M \tag{2.62}$$

where ϑ'_{ji} and $\vartheta''_{\mathrm{ji}}$ are the stoichiometric coefficients of the reactants and products respectively. The net chemical reaction rate of each species in a multistep chemical reaction can be written as:

$$\dot{\omega}_{\mathrm{j}} = \sum_{\mathrm{i}=1}^{M} \left(\vartheta''_{\mathrm{ji}} - \vartheta'_{\mathrm{ji}}\right) \left(K'_{\mathrm{i}} \prod_{\mathrm{j}=1}^{N} \left[X_{\mathrm{j}}\right]^{\vartheta'_{\mathrm{ji}}} - K''_{\mathrm{i}} \prod_{\mathrm{j}=1}^{N} \left[X_{\mathrm{j}}\right]^{\vartheta''_{\mathrm{ji}}} \right) \tag{2.63}$$

where K'_{i} and K''_{i} represent the forward and reverse rate coefficients respectively and $\left[X_{\mathrm{j}}\right]$ is the molar concentration. The rate coefficients can be calculated using the Arrhenius law:

$$K_{\mathrm{i}} = A_{\mathrm{i}} T^{\beta_{\mathrm{i}}} exp\left(-\frac{T_{a\mathrm{i}}}{T}\right) \tag{2.64}$$

where A_{i}, β_{i} and $T_{a\mathrm{i}}$ represent the pre-exponential factor, temperature exponents and activation temperature for the reaction i. The computation of a premixed flame requires the calculation of the chemical reaction rate for all species. However, due to complex nature of the reacting system, the process is computationally expensive, preventing the method to be used for practical engineering situations. Therefore, the simplifications of chemistry and transport are required to tackle the complex problems. Poinsot and Veynante [55] have discussed various useful assumptions, for example, one-step chemistry mechanism, to simplify the problem. The intense non-linear nature of the mean reaction rate is preserved even after the simplification and it offers the greatest challenge in turbulent combustion modelling

2.4.2 Laminar flame structure

A structure of a typical one-dimensional (1D) laminar premixed flame is comprised of three regions: the preheat zone, the inner layer and the oxidation zone [2]. Figure 2.3 shows the structure of 1D methane-air laminar premixed flame where the flame is stationary and the reactants are entering the flame with a speed equal to the flame propagation speed s_L^0 [2]. In the preheat zone, the temperature of the unburnt reactants is raised by heat transfer from the inner zone through thermal diffusion. However, chemical reaction does not occur in this region as the temperature is below the activation temperature of the chemical reaction. The most of the

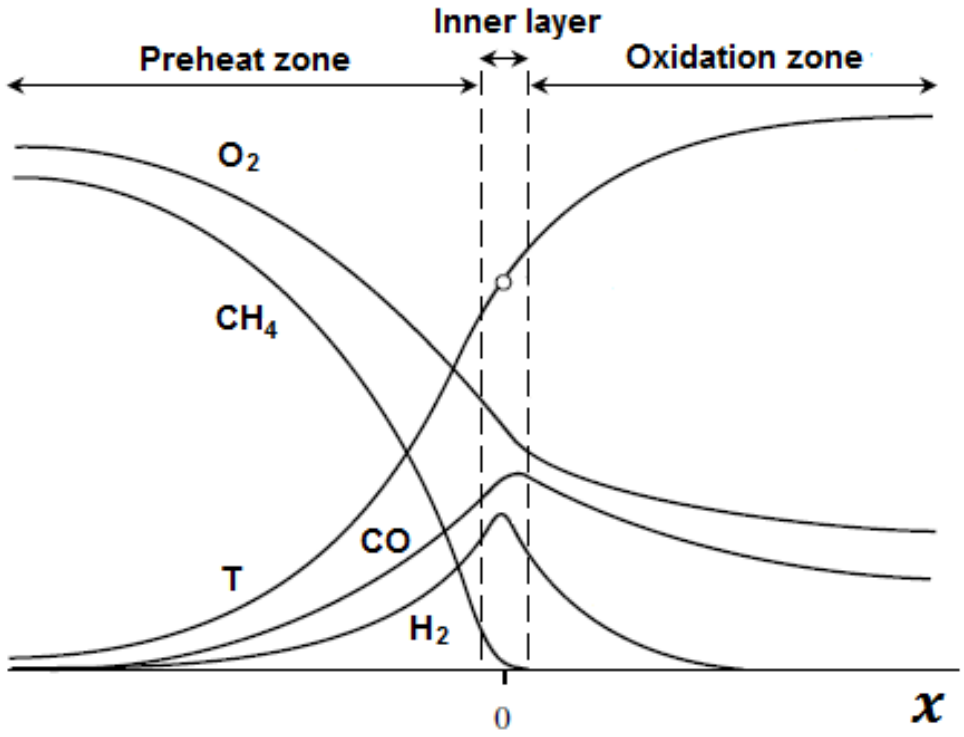

Figure 2.3: The structure of a premixed methane-air flame [2]

chemical reaction takes place in the inner zone where the temperature is higher than the activation temperature. The bulk of the chemical energy is released in this region. The inner zone is quite thin (approximately 0.1 times the laminar flame thickness at atmospheric pressure [2]) and it is followed by a much wider region of slow chemistry where the radicals are recombined in exothermic reactions. The balance of mass and heat diffusion maintains the three-zone flame structure. The thickness of the inner zone also determines different turbulent premixed regimes. The structure of the inner zone is affected by the turbulence when the smallest turbulent eddies are smaller than the thickness of the inner zone. The turbulent mixing would enhance heat conduction and diffusion of radicals out of it. The unburnt reactants from the preheat zone are transferred to the inner zone through mass diffusion, while the heat produced through chemical reactions occurring in both the inner and oxidation zones, is transferred into the preheat zone because of the temperature gradient. The ratio of thermal to mass diffusivity of a reactant mixture is given by *Le* number (Eq. 2.14).

2.4.3 Laminar flame properties: thickness and speed

Defining and estimating the laminar flame thickness is an important parameter in the numerical modelling of premixed flames. It is not only used as a parameter in the combustion models, but also controls the required mesh resolution so that the flame structure is properly resolved. The flame thickness can be defined using many ways, as described in [55]. One way of defining the flame thickness is to use the distance over which the progress variable changes from 0.01 to 0.99 and the calculated thickness is known the total flame thickness δ_L^t. The limits are selected arbitrarily and this method would result in a thicker flame and can be misleading to determine the grid resolution [55]. A more useful way of calculating thickness is to use the temperature profile and compute the maximum gradient of temperature. The flame thickness calculated from this method is known as the thermal flame thickness:

$$\delta_L^0 = \frac{T_2 - T_1}{\max\left(\left|\frac{\partial T}{\partial x}\right|\right)} \tag{2.65}$$

δ_L^t and δ_L^0 can only be calculated during the post-processing of the flame front propagation results, for example, in a one-dimensional laminar flame study using a certain air-fuel mixture ratio. The calculation of δ_L^t and δ_L^0 is illustrated in Fig. 2.4. From scaling laws, another useful

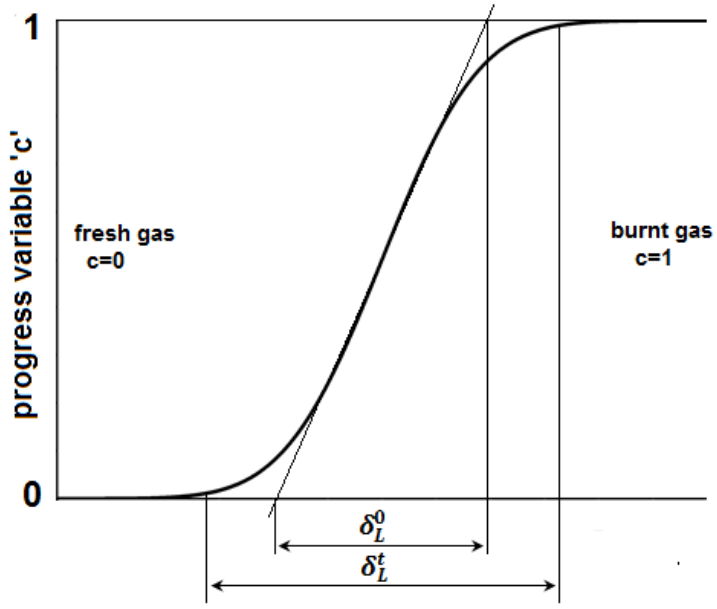

Figure 2.4: Calculation of thermal and total flame thicknesses for a premixed flame.

definition of the flame thickness, known as the Zeldovich thickness [73], can be constructed which depends on the laminar flame speed s_L^0 and thermal diffusivity α_{th}, and can be calculated before the start of the actual simulation.

$$\delta_L = \frac{\lambda}{\rho_u C_p s_L^0} = \frac{\alpha_{th}}{s_L^0} \tag{2.66}$$

In the present work, the Zeldovich thickness is used.

Another important parameter in the modelling of premixed flames is the laminar flame speed s_L^0, which is defined as the speed at which the flame front propagates towards the fresh unburnt mixture. It can also be defined as the magnitude of the fresh mixture velocity to keep the flame at the same spatial position, i.e. no propagation towards the reactants. As shown in Fig. 2.5, it is directed normal to the flame from products to reactants. The laminar flame speed can either be calculated experimentally [74,75] or estimated by algebraic expressions [55]. The classical analysis of Zeldovich, Frank-Kamenetski and von Karman (ZFK) or the analysis based on the Arrhenius expression [55], are used as the basis of most algebraic expressions. The expressions for s_L^0, using these methods as described in [55], are proportional to the square root of the

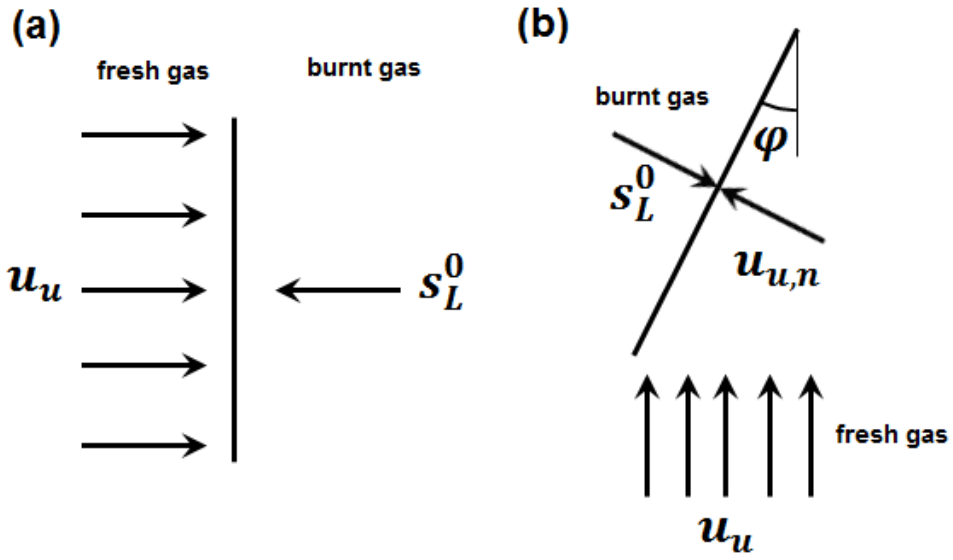

Figure 2.5: Laminar flame speeds when the flame propagation is (a) normal (b) oblique to the fresh gas flow.

product of the reaction and diffusion coefficients. Another useful way of calculating s_L^0 is the numerical computation of 1D flames using detailed chemistry. In the present work, the experimental values of s_L^0 are used in the numerical simulations of premixed flames.

For a given fuel, the laminar flame speed s_L^0 depends on the equivalence ratio, pressure and the initial temperature of the reactants. The influence of pressure and unburnt gas temperature on s_L^0 for selected fuels is described in the experimental studies [74,75]. Generally, s_L^0 decreases with increasing pressure and increases with increasing fresh gas temperature, but the influence of changing temperature is stronger than pressure.

2.4.4 Effect of turbulence on flame front

The practical industrial devices involve the reactive processes in a turbulent environment. The introduction of turbulence increases the rate of consumption of reactants and the rate of heat released to much greater values compared to those under laminar environment. Turbulence induces the wrinkling of the flame due to an interaction of eddies with the flame front and results in an increased flame propagation, which is known as the turbulent flame speed s_t. One of the simplest ways to study the effect of flame wrinkling on the flame propagation speed is to consider a 1D laminar flame propagating in the negative x-direction against the turbulent flow of fresh reactants as shown in Fig. 2.6. The flame wrinkling increases the flame area, therefore, the ratio of s_t to s_L is simply a ratio of the wrinkled flame front area to the laminar flame area:

$$\frac{s_t}{s_L} = \frac{A_t}{A_L} \tag{2.67}$$

Many theoretical [76-79] and experimental [80-83] attempts have been made by several researchers to relate the turbulent flame speed to flow properties. The first model was presented by Damköhler [77] and can be written as:

$$\frac{s_t}{s_L} = 1 + \frac{u'}{s_L} \tag{2.68}$$

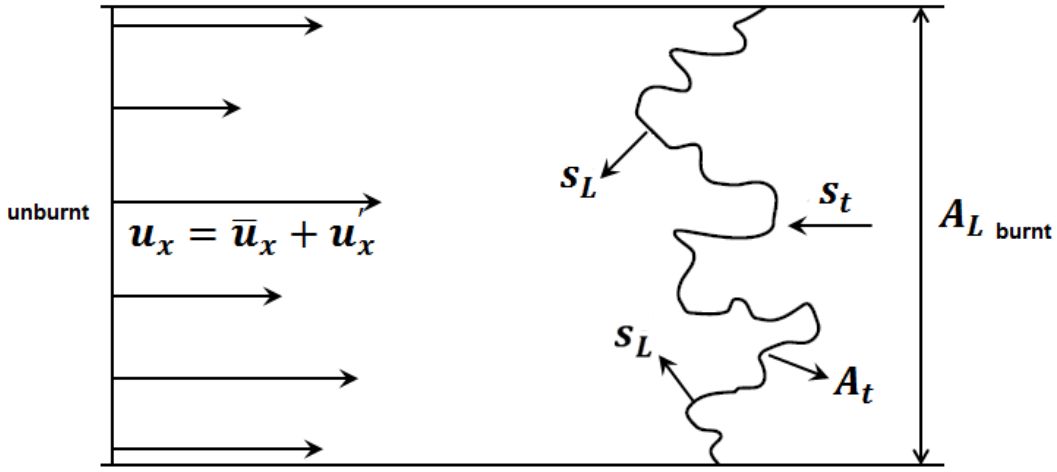

Figure 2.6: A schematics representation of a propagating flame front in a turbulent flow field

Several researchers have also represented the ratio s_t/s_L^0 in terms of flow properties using a general power law of the form:

$$\frac{s_t}{s_L} = 1 + C\left(\frac{u'}{s_L}\right)^n \tag{2.69}$$

where C and n can take a range of values [2]. When the turbulence intensity is small, or the flame thickness is smaller than the Kolmogorov scale, thus the turbulence can only wrinkle the flame but cannot disturb the inner laminar flame structure. This regime of premixed combustion is known as the wrinkled Flamelet regime. On the other hand, for high-intensity turbulence, the smallest turbulent eddies are smaller than the flame thickness. These eddies can enter into the preheat zone and enhance the transport of heat and radicals within the chemically inert preheat zone. This regime is known as the thin reaction zone regime. Different premixed combustion regimes will be discussed in detail in section 2.4.5. Based on the scaling of laminar flame speed with the molecular kinematic viscosity:

$$s_L \sim \left(\frac{\nu}{\tau_c}\right)^{0.5} \tag{2.70}$$

Damköhler [77] argued that ν in the thin reaction zone regime should be replaced with the turbulent kinematic viscosity and the turbulent flame speed can be written as:

$$s_t \sim \left(\frac{\nu_t}{\tau_c}\right)^{0.5} \tag{2.71}$$

From Eq. (2.70) and (2.71), a relation between s_t and s_L can be written as:

$$\frac{s_t}{s_L} \sim \left(\frac{\nu_t}{\nu}\right)^{0.5} \tag{2.72}$$

The above paragraphs discussed the effect of turbulence on the flame front, however, the turbulent flow field can also be influenced by the combustion. The combustion is accompanied by a large temperature rise, which increases the kinematic viscosity and decreases the Re number, so the flow can be re-laminarized. On the other hand, the flow experiences flame generated turbulence due to a rapid acceleration through the thin flame front, hence, generating higher velocity fluctuations. The increment in the velocity through the flame front is significant (of the order of 4-5 m/s) for typical hydrocarbons flames [55]. Moreover, such flames have the typical flame thicknesses of the order of 0.1 mm, which means that the flow acceleration across the flame is occurring through a very thin region and thus modifies the turbulent flow field. The velocity and density changes also lead to a change in the vorticity field and results in the so-called flame generated turbulence. However, the effects of flame fronts on turbulent field depend on different factors. Some flows experiences re-laminarization while a few studies suggest that the flow experiences an enhancement of the turbulent flow field when burning [55].

2.4.5 Premixed combustion regimes

In premixed combustion, different regime diagrams have been proposed to describe the turbulence-chemistry interactions. Borghi [84], Peters [2], Abdel-Gayed and Bradley [85], Poinsot and Veynante [55], Düsing *et al.* [86] and others have presented different forms of regime diagrams in terms of length and velocity scale ratios. Along with the length and velocity scale ratios, three dimensionless numbers, i.e. the turbulent Reynolds number, the Damköhler number and the Karlovitz number, are also used in this regime diagram to identify different combustion regimes. Figure 2.7a shows the regime diagram proposed by Peters [2], which plots the velocity ratio u'/s_L^0 versus length scale ratio l_0/δ_L.

The turbulent Reynolds number in terms of flame properties can be written as:

$$Re_t = \frac{u' l_0}{s_L \delta_L} \tag{2.73}$$

$Re_t < 1$ represents the laminar Flamelet regime in Fig. 2.7a. Because of the low turbulence level, this regime yields little interest in technical combustion devices.

The turbulent Damköhler number represents the ratio of a characteristics flow or mixing time to a characteristics chemical time scale:

$$Da = \frac{\tau_f}{\tau_c} = \frac{l_0 s_L^0}{\delta_L u'} \tag{2.74}$$

$Da \gg 1$ represents the fast chemistry regime where the rate of chemical reaction is faster than the fluid mixing rate. On the other hand, $Da \ll 1$ represents a well-stirred reactor regime where the reaction rate is slower than the mixing rate.

The Karlovitz number represents the ratio of chemical time scale to the Kolmogorov time scale and describes the turbulence-chemistry interaction on the smallest turbulent scales. It can be defined as:

$$Ka = \frac{\tau_c}{\tau_\eta} = \left(\frac{u'}{s_L^0}\right)^{3/2} \left(\frac{\delta_L}{l_0}\right)^{1/2} = \left(\frac{\delta_L}{l_\eta}\right)^2 \tag{2.75}$$

Using Ka and Da, various combustion regimes can be identified in Fig. 2.7a. $Ka < 1$ (Da >1) represents the flamelet regime where the laminar flame thickness is small in comparison with the Kolmogorov scales. Turbulence can therefore only wrinkle the thin laminar flame, but cannot disturb the laminar flame structure. On the basis of the values of u'/s_L^0, the flamelet regime can be further be divided into two regimes i.e. the wrinkled flamelet ($u'/s_L^0 < 1$) and the corrugated flamelet regime ($u'/s_L^0 > 1$). The criterion for the existence of flamelet regime is sometimes referred to as the Williams-Klimov criterion [87] ($Ka = 1$). On the other hand $Ka > 1$ represents the thin reaction zone regime (TRZ) where the Kolmogorov scale gets smaller than the flame thickness but remains bigger than the reaction zone thickness, which can be estimated to be one order of magnitude smaller than the flame thickness. In this regime, the transport within the preheat region is increased by the turbulent mixing while the thin reaction zone retains a laminar structure. The most practical engineering systems are operated in the thin reaction zone regime, because the enhanced mixing leads to a higher heat release and shorter combustion

times. $Ka \approx 100$ represents the other extreme in the regime diagram where all the turbulent scales are smaller than the reaction zone thickness, which is known as broken reaction zone (BRZ) regime. The molecular processes become no longer responsible for the transport within the reaction zone, but solely controlled by the turbulence. The Karlovitz number can also be defined in terms of the reaction zone thickness which is typically $0.1\delta_L$, such that Ka_δcan be written as:

$$Ka_\delta = \left(\frac{0.1\delta_L}{l_\eta}\right)^2 = 0.01Ka \tag{2.76}$$

The Ka_δ can be used to divide the thin reaction zone regime and the broken reaction zone regime. $Ka_\delta > 1$ represents the broken reaction zone regime. The broken reaction zone regime is usually avoided in the most practical engineering systems because of the noise, instabilities and flame extinction problems.

The regime diagram presented by Peters [2], as shown in Fig 2.7a, is based on physical quantities only. A similar regime diagram for LES is proposed by Pitsch and Duchamp de Lageneste [88] and Pitsch [89] using the filter size Δ as the length scale and the sub-filter velocity fluctuation u'_Δ as the velocity scale. This LES regime diagram introduces both physical and modelling parameters and describes the sub-filter turbulence-chemistry interactions. This regime diagram uses the ratio of filter width to laminar flame thickness Δ/δ_L and the sub-grid Karlovitz number Ka_Δ as the axes of the diagram, as shown in Fig. 2.7b. The sub-filter Reynolds number, the Damköhler number and the Karlovitz number relevant in Fig. 2.7b can be defined by replacing u' and l_0 with u'_Δ and Δ, respectively.

$$Re_\Delta = \frac{u'_\Delta\,\Delta}{s_L^0\delta_L}, \qquad Da_\Delta = \frac{\Delta\, s_L^0}{\delta_L u'_\Delta}, \qquad Ka_\Delta = \left(\frac{u'_\Delta}{s_L^0}\right)^{3/2}\left(\frac{\delta_L}{\Delta}\right)^{1/2} = \left(\frac{\delta_L}{{s_L^0}^3}\epsilon\right)^{1/2} \tag{2.77}$$

The second definition of Ka_Δ in Eq. (2.77) is obtained by substituting the value of l_η from Eq. (2.27) with $\nu = s_L^0\delta_L$ into the length scale ratio definition of Ka in Eq. (2.75). This shows that, although Ka_Δ is defined in terms of physical and modelling parameters but it remains a physical quantity independent of filter width as the dissipation rate is constant within the inertial sub-range. Therefore, in LES, for a given flow field and chemistry, Ka_Δ is a fixed quantity such that the changes in the filter width are counterbalanced by the subsequent changes in u'_Δ. Another

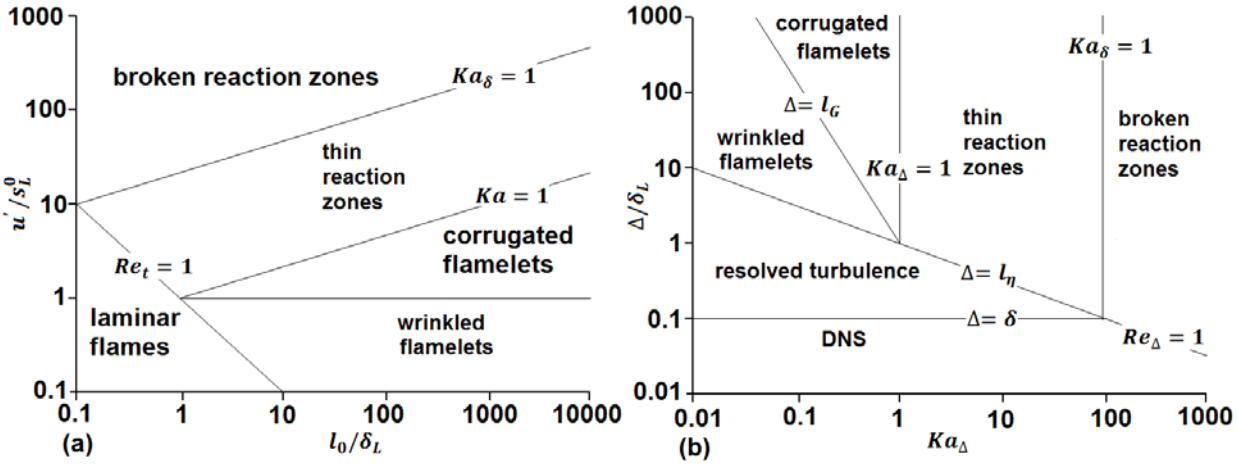

Figure 2.7: Premixed combustion regime diagrams proposed by (a) Peters [2] (b) Pitsch [89]

interesting feature of the LES regime diagram is that a transition between different combustion regimes is not observed as the filter width is changed at constant Karlovitz number. The influence of changing Δ can be studied, by starting from any of the combustion regimes at large Δ/δ_L. As Δ is reduced, the Re_Δ eventually becomes smaller than one. This regime corresponds to the resolved turbulence regime as Δ is smaller than the Kolmogorov scales. However, in order to resolve the entire flame including the reaction zone, the filter width should be much smaller than the reaction zone thickness.

2.5 Overview of Premixed Combustion models

The main challenge in the numerical modelling of premixed flames using LES method, is the modelling of the filtered reaction rate. When the LES filtering process is applied, the effect of the unresolved turbulence on the flame front wrinkling is neglected. Another main challenge in the LES premixed combustion modelling is that a premixed flame is generally much smaller than the LES filter width Δ, as shown in Fig. 2.8. Thus for a major part of the regime diagram the flame is mostly on the sub-filter scale. The flame front cannot be resolved on typical LES mesh, which leads to numerical problems. A suitable modelling of the filtered reaction rate is the main task of premixed combustion modelling. In this section, different modelling methods based on the Flamelet assumption (i.e. assuming the flame front a thin surface separating burnt and fresh gases) will be discussed.

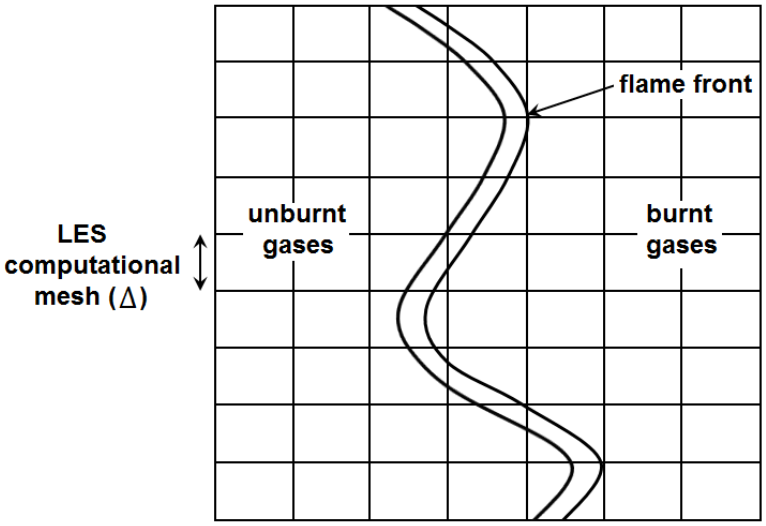

Figure 2.8: Comparison between premixed flame thickness and typical LES mesh size Δ

2.5.1 The Arrhenius approach

The Arrhenius approach represents the reaction rate in terms of mean quantities. In LES, this is equivalent to compute the filtered reaction rate based on the resolved quantities. This approach neglects the effects of turbulence on the turbulent combustion by retaining only the first term in the Taylor series of the exponential function and discarding the subgrid scale fluctuations:

$$\bar{\dot{\omega}} = \bar{\dot{\omega}}(\tilde{c}) = -A\bar{\rho}(1-\tilde{c})exp\left(-\frac{T_a}{T_u + (T_b - T_u)\tilde{c}}\right) \tag{2.78}$$

This model is applicable only in the low Damköhler limit where reactants burn slowly but mix rapidly and can be effectively used for a simple analysis. Nieuwstadt and Meeder [90] have used this approach for modelling chemical reactions in atmospheric boundary layers. However, in the context of premixed combustion, the model is inadequate [91] and can lead to significant errors of orders of magnitude [55].

2.5.2 The eddy break-up model (EBU)

The eddy break up model (EBU) was first proposed by Spalding [92]. Contrary to the Arrhenius model, the eddy break up model assumes that the turbulent structures control the reaction rate

and the chemistry does not play any explicit role. Thus, the model is applicable to fast chemistry regime, which is characterized by high Reynolds and Damköhler numbers. Based on these assumptions, the reaction rate can be written in terms of characteristic turbulent mixing time τ_t and the temperature fluctuations $\widetilde{T''^2} = \tilde{c}(1-\tilde{c})$ [56]:

$$\bar{\dot{\omega}} = C_{EBU}\bar{\rho}\frac{\tilde{c}(1-\tilde{c})}{\tau_t} \tag{2.79}$$

where C_{EBU} is a model constant. In the RANS context, the turbulence time τ_t can be calculated using the turbulent kinetic energy k and its dissipation rate ϵ:

$$\tau_t = \frac{k}{\epsilon} \tag{2.80}$$

The eddy break up model can also be extended for the context of LES:

$$\bar{\dot{\omega}} = C_{EBU}\bar{\rho}\frac{\tilde{c}(1-\tilde{c})}{{\tau_t}^{sgs}} \tag{2.81}$$

where ${\tau_t}^{sgs}$is the sub-grid turbulent time scale:

$${\tau_t}^{sgs} = \frac{\Delta}{\sqrt{k_{sgs}}} \tag{2.82}$$

The sub-grid turbulent kinetic energy k_{sgs} is modelled either using algebraic expressions or solving an additional transport equation for k_{sgs} as discussed in section 2.3.3.3. The EBU model is attractive because of its simple formulation and its applications are found in most commercial codes. However, its basic form has an obvious shortcoming that the reaction rate is independent of chemical reaction. The model also tends to over-predict the reaction rate, especially in zones of high strain as ϵ/k becomes large [55]. Another drawback is the model constant C_{EBU}, which depends on various parameters and needs to be adjusted for each test case. Said and Borghi [93] proposed some modifications of $C_{EBU}$to incorporate the chemical effects. Fureby and Moeller [94] coupled the EBU model and the Arrhenius law to limit the mean reaction rate using the chemistry effects.

2.5.3 The artificially thickened flame model (ATF)

The artificially thickened flame model solves the issue of resolving the laminar premixed flame on an LES mesh by artificially modifying the transport-chemistry interaction to obtain a thickened flame that can be resolved on a given mesh, as shown in Fig 2.9. The flame is artificially thickened by multiplying the flame diffusivity by a constant factor. Then, the reaction rate needs to be divided by the same factor to obtain the same flame speed as in the un-thickened case. The model based on this principle was first presented by Butler and O'Rouke [6]. Based on the laminar premixed flame theories [95,96], the flame speed s_L and the flame thickness δ_L can be written as:

$$s_L \propto \sqrt{\alpha_{th}\bar{\dot{\omega}}}\,; \qquad \delta_L \propto \frac{\alpha_{th}}{s_L} = \sqrt{\frac{\alpha_{th}}{\bar{\dot{\omega}}}} \tag{2.83}$$

It can be seen that when α_{th} is multiplied and $\bar{\dot{\omega}}$ is divided by a thickening factor F, the flame speed remains constant but the flame thickness becomes $F\delta_L$. Unfortunately, the thickening of the flame from δ_L to $F\delta_L$ is accompanied by a change in the turbulence-chemistry interactions as

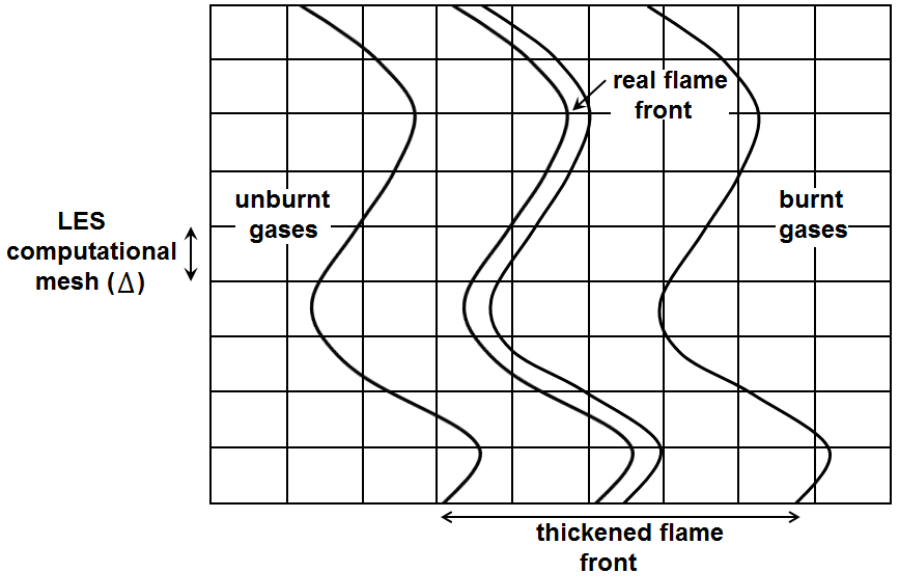

Figure 2.9: Schematic representation of the artificially thickened flame method

indicated by a decrement in the Damköhler number (Eq. (2.73)) by a factor F. This means that the thickened flame becomes more and more insensitive to turbulent motions as F is increased. The thickened flame experiences lesser wrinkling induced by the turbulent structure compared to the un-thickened flame. Angelberger *et al.* [97] and Colin *et al.* [7] investigated these effects using DNS of flame/vortex interactions. They proposed that the reaction rate should be empirically modified by multiplying with an efficiency function E to compensate for the loss in the flame wrinkling such that the thickened flame propagates with a turbulent speed of Es_L. Assuming single step chemistry, the LES filtered progress variable transport equation, to model an artificially thickened flame model, can be written as:

$$\frac{\partial \bar{\rho}\tilde{c}}{\partial t} + \frac{\partial \bar{\rho}\widetilde{u_i}\tilde{c}}{\partial x_i} = \frac{\partial}{\partial x_i}\left(\bar{\rho}EF\alpha_{th}\frac{\partial \tilde{c}}{\partial x_i}\right) + \frac{E\bar{\dot{\omega}}}{F} \tag{2.84}$$

Where the Arrhenius law is used to express $\dot{\omega}$ [26,98]:

$$\bar{\dot{\omega}} = A\bar{\rho}(1-\tilde{c})exp\left(-\frac{T_a}{T}\right) \tag{2.85}$$

The ATF model offers the advantage of modelling the situations of ignition, quenching, flame-wall interaction and complex chemistry [55]. However, the artificial thickening modifies the interaction between chemistry and turbulence, such that the model performance depends on the proper estimation of thickening factor and the efficiency function to compensate for the loss of flame wrinkling.

2.5.4 G-equation model

Contrary to the ATF method, G-equation model assumes the flame thickness to be infinitely thin and the position of the flame front is described by an iso-level G^*, which separates the reactant domain into fresh ($G > G^*$) and burnt ($G < G^*$) gas zones, as shown in Fig. 2.10. The transport equation for the field variable G can be written as:

$$\frac{\partial \bar{\rho}\tilde{G}}{\partial t} + \frac{\partial \bar{\rho}\widetilde{u_i}\tilde{G}}{\partial x_i} = \rho_u \bar{s_t}|\nabla \bar{G}| \tag{2.86}$$

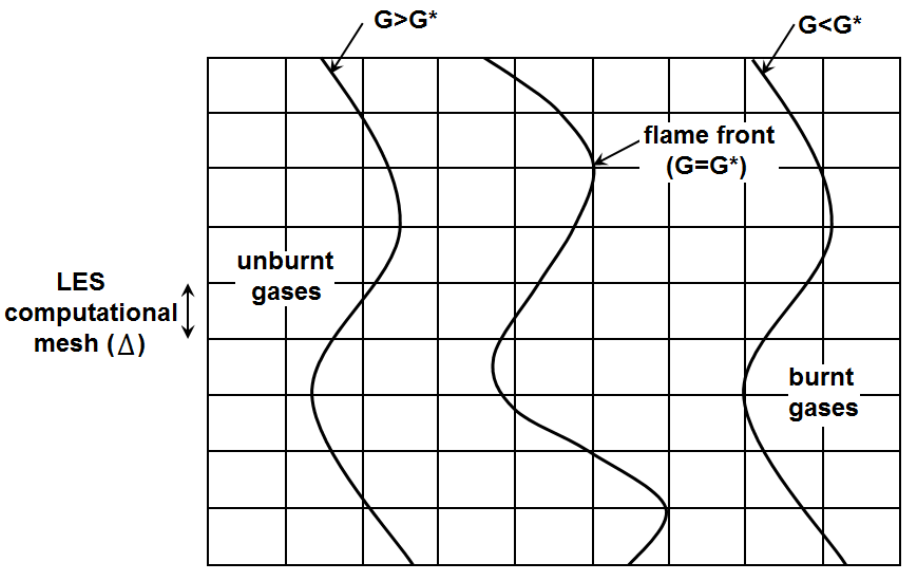

Figure 2.10: Schematic representation of the G-equation method

The comparison of above equation with the transport equation of the progress variable, Eq. (2.86), shows that the G-transport equation does not have a filtered molecular diffusion and sub-grid scalar transport terms and the mean reaction rate is replaced by $\rho_u \bar{s_t} |\nabla \bar{G}|$. Despite of the simple formulation of G-equation model, the absence of molecular diffusivity can lead to numerical difficulties. The numerical flame cusps can be formed, which require the addition of artificial diffusivity in the expression of $\bar{s_t}$ [98,99]. The inherent numerical diffusion present in some combustion codes may also smear out the flame cusps [100]. Kim *et al.* [101] and Im *et al.* [98] included the subgrid transport in the G-equation model and modelled it using a simple gradient hypothesis. The subgrid scale turbulent flame speed $\bar{s_t}$ needs to be properly modelled and its closure is generally based on Eq. (2.68):

$$\frac{\bar{s_t}}{s_L} = 1 + C \left(\frac{u'_\Delta}{s_L} \right)^n \tag{2.87}$$

where u'_Δ is the subgrid scale turbulence level. $\bar{s_t}$ is not a well-defined quantity and lacks the availability of a universal mode [55]. Yakhot [102], Pocheau [103] and Kim *et al.* [101] developed and investigated the performance of algebraic models for $\bar{s_t}$ for an accurate prediction of the flame location. Peters [2] discussed a closure model for $\bar{s_t}$ appropriate for the corrugated Flamelet and thin reaction zone regimes. The model was further developed by Pitsch and De

Lagneste [88] for LES of turbulent Bunsen flames. Despite these limitations, the G-equation model is a popular method for premixed combustion modelling.

2.5.5 Flame surface density model (FSD)

The FSD method for LES was presented by Boger *et al.* [8]. Contrary to the G-equation model, which arbitrarily defines a G-field, the FSD model characterizes the premixed flame propagation in terms of physical quantities, such as the progress variable and the flame surface densities that can be extracted from DNS or experimental measurements. In RANS context, the FSD represents the mean flame surface area per control volume, while in LES context it represents the flame surface within the filter volume. In the LES filtered progress variable transport equation, the sum of filtered molecular diffusion term and the reaction can be described in terms of generalized flame surface density Σ_{gen}. The term "generalized" is used here to refer to the independence of Σ_{gen} on any chosen progress variable contour. There are two well-established approaches for FSD modelling. In one approach, the FSD is modelled in terms of a transport equation [8,10-13], while the other approach involves an algebraic formulation [97,53,104-106]. The FSD method and some of the popular algebraic FSD models will be discussed in detail in chapter 4.

Chapter 3

Numerical Methodology

This chapter presents the numerical methodology used for the discretization of the set of equations of mass, momentum, energy and progress variable that were described in chapter 2. The set of aforementioned partial differential equations (PDEs) characterize the main flow variables that vary across time and space domains. In order to obtain a solution using a computational code, the set of PDEs is discretized on a computational grid and undergoes time and spatial advancement. The term discretization is defined as a process of approximating a problem into discrete quantities and converts a PDE that is usually non-linear, into a simple algebraic expression. The CFD package used in the present work is an open source software known as OpenFOAM.

3.1 Spatial discretization

3.1.1 Grid structure

Figure 3.1a shows the spatial discretization of the space domain in OpenFOAM. The space domain is converted into a computational mesh that consists of a number of contiguous cells or control volumes and the PDEs are subsequently discretized on this mesh. The cells completely fill the domain and do not overlap one another. The code principally uses a collocated grid arrangement where the dependent variables and other properties are stored at the cell centroids. However, they may also be defined at the cell faces or vertices. The collocated grid needs more interpolation than the staggered grid as the quantities stored at cell faces must first be interpolated to the cell centres. However, the collocated arrangement offers greater simplicity in handling the different control volumes for different variables. It also minimizes the number of coefficients that must be calculated and stored. In OpenFOAM, an arbitrarily unstructured mesh can be created with no limitation on the number of faces bounding each cell nor any restriction on the alignment of each face. This gives greater freedom in spatial discretization, particularly when the geometry of the domain is complex. Figure 3.1b shows a two-cell arrangement with

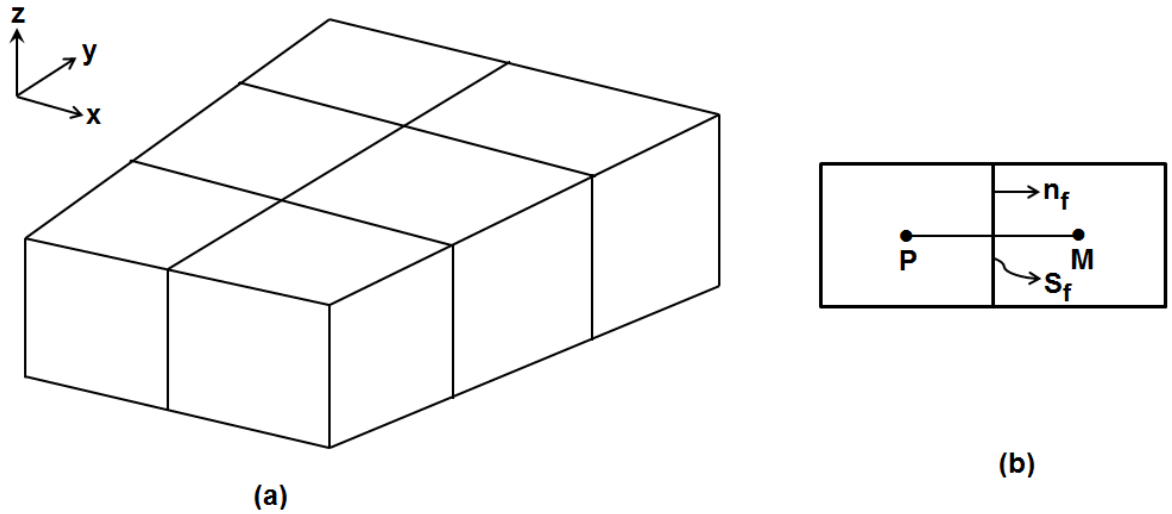

Figure 3.1: (a) Spatial discretization of the solution domain (b) Parameters in finite volume discretization

centroids P and M. The surface connecting the two cells has surface area S_f and normal unit vector n_f.

3.1.2 Finite volume method

The finite volume (FV) method and others such as finite difference and finite elements methods, all transform the set of PDEs into a system of linear algebraic equations. The FV method is commonly used in the modern CFD tools and also in OpenFOAM as a discretization method. It has gained high popularity in recent times because of the high flexibility it provides as a discretization method. The discretization can be performed directly in the physical domain without any requirement for transformation between the physical and computational coordinate systems. The adoption of collocated grid arrangement allowed this method to cover a wide range of applications from simple to complex geometries, while holding the simplicity of its mathematical formulation. The inherent conservation property in dealing with the face fluxes makes the FV method a preferred choice among modern CFD tools. Since the unknown variables are evaluated at the cell centres, the implementation of a variety of boundary conditions is quite easy [107]. A brief description of FV method is presented in the next paragraphs and the interested reader is referred to [107, 108] for more detail.

The FV discretization of each term of the PDEs is formulated by first doing an integration of the term over a cell volume. Then, the volume integrals of the most spatial derivative terms are replaced by integrals over the cell surfaces through the use of the Gauss's theorem:

$$\int_V \frac{\partial}{\partial x_i}(\emptyset)\, dV = \int_S \emptyset n_i\, dS \tag{3.1}$$

where n_i represents a normal vector pointing outwards from the control volume surface. The surface integral can be easily calculated as the sum over all cell surfaces:

$$\int_S \emptyset n_i\, dS = \sum_f \emptyset_f n_f S_f \tag{3.2}$$

where f represents the cell face with surface area S_f. With the application of the FV method, the general transport equation for a conserved scalar Q (setting $\emptyset = \rho Q$ in Eq. (2.21)) can be written for a control volume P as:

$$\int_t^{t+\Delta t}\left[\int_{V_P}\frac{\partial \emptyset}{\partial t}dV + \int_{V_P}\frac{\partial(\emptyset u_i)}{\partial x_i}dV - \int_{V_P}\frac{\partial}{\partial x_i}\left(D\frac{\partial \emptyset}{\partial x_i}\right)dV\right]dt = \int_t^{t+\Delta t}\left[\int_{V_P}\dot{\omega}\; dV\right]dt \tag{3.3}$$

Assuming that the control volumes do not change with time and using the Gauss's theorem for the volume integral of the convective and diffusive terms, Eq. (3.3) can be written as:

$$\int_t^{t+\Delta t}\left[\left(\frac{\partial \emptyset}{\partial t}\right)_P V_P + \sum_f \emptyset_f u_f n_f S_f - \sum_f \left(D\frac{\partial \emptyset}{\partial x_i}\right)_f n_f S_f\right]dt = \int_t^{t+\Delta t}[\dot{\omega}_P V_P]\; dt \tag{3.4}$$

Since $\emptyset$ is stored at the cell centroid, it needs to be interpolated to the center of the cell surface in order to calculate the convective and diffusive fluxes in above equation. The diffusive fluxes are normally calculated using a second order central differencing scheme while a variety of interpolation schemes are available in OpenFOAM to evaluate the convective fluxes as discussed in the next section. The notation used in explaining these schemes is illustrated in Fig. 3.2. The mass and momentum equations can be discretized using a similar approach by setting $\emptyset$ equal to ρ and ρu_j respectively.

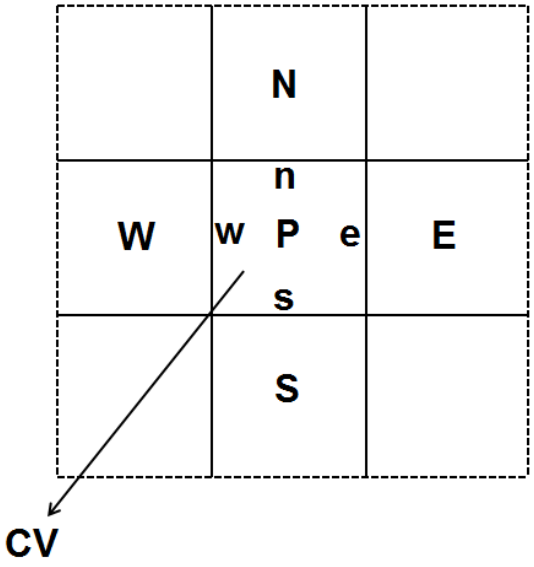

Figure 3.2: Nomenclature for a 2D collocated grid showing cells in the North (*N*), West (*W*), East (*E*) and South (*S*) directions with respect to the control volume *P*. The upper case letters denote the cell centroids while lower case letters represent the cell faces.

3.1.3 Convective fluxes ($F_{C,f}$)

The convective flux for the east face, e, of the control volume P can be written as:

$$F_{C,e} = \emptyset_e u_e n_e S_e \tag{3.5}$$

If the grid is equidistant, the normal velocity on the east face u_e can be calculated using linear interpolation:

$$u_e = \frac{u_P + u_E}{2} \tag{3.6}$$

The remaining term $\emptyset_e$ in Eq. (3.4) can be calculated using a variety of schemes, each of which hold varying degrees of order (accuracy) and stability. Only three basic schemes are described here, the interested readers are referred to [108] for detailed explanations of other schemes.

The upwind differencing (UD) scheme is first order accurate and it determines $\emptyset_e$ from the direction of the flow. It is bounded at the expense of accuracy.

$$\emptyset_e = \begin{cases} \emptyset_P & if u_e > 0 \\ \emptyset_E & if u_e < 0 \end{cases} \tag{3.7}$$

A major inadequacy of this scheme is that it produces incorrect results, due to its diffusive nature, when the flow direction is oblique to the grid lines. The diffusive characteristic of UD scheme can be demonstrated by taking a Taylor series expansion of $\emptyset_e$ around point P. The first truncation term is $\Delta x(\partial\emptyset/\partial x)_P$ which resembles the diffusive flux and can lead to erroneous solutions.

The central differencing (CD) scheme is second order accurate but un-bounded. For a uniformly spacing grid, $\emptyset_e$, using CD scheme can be written as:

$$\emptyset_e = \frac{\emptyset_P + \emptyset_E}{2} \tag{3.8}$$

One of the major drawbacks of this scheme is its inability to identify the flow direction. The $\emptyset_e$ is always influenced by both $\emptyset_P$ and $\emptyset_E$. In the case of strongly convective flow from west to east, this calculation gives erroneous results because the east cell face should get much stronger influencing from node P than the node E. The central differencing scheme is normally used for the convective term in the momentum equation and is not ideal for the scalar transport equation as it can give undershoots and overshoots. The CD scheme is also less diffusive than the UD scheme, as the leading truncation term in the Taylor series expansion of $\emptyset_e$ around point P is of the order of $\sim O(\Delta x)^2$ contrary to UD schemes ($\sim O(\Delta x)$). It also shows that the truncation error reduces by a power of two and one in the CD and UD schemes, respectively, with the grid refinement.

It has been described that an accurate and stable solution cannot be obtained using UD or CD schemes. Several high order schemes have been designed to overcome the inadequacies of the UD scheme but they produce oscillations or wiggles, which can give physically erroneous negative values and instability. The total variation diminishing (TVD) schemes are designed to overcome the aforementioned issue. In TVD schemes, the undesirable oscillatory behaviour is stabilized by adding an artificial diffusion part or weighting towards upstream contribution. The general form of a TVD scheme can be written as:

$$\emptyset_e = \emptyset_P + B(r)\frac{\emptyset_P - \emptyset_W}{2} \; ; \; r = \frac{\emptyset_E - \emptyset_P}{\emptyset_P - \emptyset_W} \tag{3.9}$$

where r is the flux limiter function. A variety of flux limiter functions exist [112] and a few of them are given below:

- SMART limiter

$$B(r) = \max\{0, \min\{2r, 0.75r + 0.25, 4\}\} \tag{3.10}$$

- CHARM limiter

$$B(r) = \frac{r(3r+1)}{(r+1)^2}, \;\; B(r) = 0 \; for \; r \leq 0 \tag{3.11}$$

- Superbee limiter

$$B(r) = \max\{0, \min\{2r, 1\}, \min\{r, 2\}\} \tag{3.12}$$

- Minmod limiter

$$B(r) = \max\{0, \min\{r, 1\}\} \tag{3.13}$$

After selecting an appropriate interpolation scheme, the total convective flux $F_{C,P}$ for control volume P can be calculated by summing the fluxes over all faces of the control volume.

3.1.4 Diffusive fluxes ($F_{D,f}$)

The diffusive flux for the east face, e, of the control volume P can be written as:

$$F_{D,e} = D_e \frac{\partial \emptyset_e}{\partial x_i} n_e S_e \tag{3.14}$$

where the diffusion coefficient D_e is obtained by interpolating the values at the centers of cells P and E. The term $\partial \emptyset_e / \partial x_1$ can be calculated using a second order central differencing scheme:

$$\frac{\partial \emptyset_e}{\partial x_1} = \frac{\emptyset_E - \emptyset_M}{\Delta x} \tag{3.15}$$

where Δx is the distance between the cell centers P and E. The total diffusive flux $F_{D,P}$ for control volume P can be obtained by summing the fluxes over all faces of the control volume.

3.2 Temporal discretization

Having discretized all the spatial terms, this section will discuss the temporal discretization of Eq. (3.3). If we represent all the spatial terms as $A\emptyset$ for control volume P, Eq. (3.3) can be written as:

$$\int_t^{t+\Delta t}\left[\int_{V_P}\frac{\partial \emptyset}{\partial t}dV\right]dt \;=\; \int_t^{t+\Delta t}\left[\int_{V_P}A\emptyset\, dV\right]dt \tag{3.16}$$

$$\frac{\emptyset_P^n-\emptyset_P^0}{\Delta t}\,V_P\Delta t = \int_t^{t+\Delta t}A^*\emptyset\;dt \tag{3.17}$$

where $\emptyset_P^n = \emptyset_P(t+\Delta t)$ and $\emptyset_P^0 = \emptyset_P(t)$ and A^* represents the spatial discretization of A. The time integral of the RHS term can be performed with three different ways as explained in the following sections.

3.2.1 Euler implicit method

This method is based on the implicit discretization of the spatial terms and uses the values at the current time step:

$$\int_t^{t+\Delta t}A^*\emptyset\;dt = A^*\emptyset^n\Delta t \tag{3.18}$$

This form of temporal discretization offers boundedness and is unconditionally stable. However, it requires a system of linear equations to be solved and thus, needs greater computational time. This method is first-order accurate in time.

3.2.2 Explicit method

This method is based on the explicit discretization of the spatial terms and uses the values at the old time step:

$$\int_t^{t+\Delta t}A^*\emptyset\;dt = A^*\emptyset^0\Delta t \tag{3.19}$$

This method is also first-order accurate in time but it does not require solving a system of linear equations. However, it becomes unstable if the Courant number C_o gets greater than 1. The C_o is defined as:

$$C_o = \frac{U_f\Delta t}{\Delta x} \tag{3.20}$$

where U_f is the characteristic velocity, e.g. flow velocity.

3.2.3 Crank Nicholson method

This method is based on the trapezoidal rule to discretize the spatial terms and uses the values at both old and current time steps:

$$\int_{t}^{t+\Delta t} A^{*}\emptyset \; dt = A^{*}\left(\frac{\emptyset^{n} + \emptyset^{0}}{2}\right)\Delta t \tag{3.21}$$

This form of temporal discretization does not offer boundedness of the solution, but is unconditionally stable. This method is second order accurate in time.

3.3 Boundary conditions

A computational grid is comprised of a series of internal and boundary faces. The latter coincide with the boundaries of the physical domain under consideration. All CFD problems require a suitable specification of initial and boundary conditions. Boundary conditions can be split into two basic types.

3.3.1 Dirichlet boundary condition

It specifies the value of the variable on the boundary. It is also known as fixed value boundary condition.

3.3.2 Neumann boundary condition

It specifies the gradient of the dependent variable normal to the boundary under consideration. It is also known as fixed gradient boundary condition.

The most of the physical boundary conditions are defined in terms of the aforementioned two basic types of boundary conditions. For an incompressible flow, the physical boundaries are defined as described in the following sections.

3.3.3 Inlet boundary condition

The inlet boundary conditions for the velocity field as well as other scalar variables like temperature, progress variable, etc. are specified by means of Dirichlet boundary condition. On the other hand, Neumann boundary condition is set for pressure at the inlet. For a turbulent case, a suitable method is required to provide a turbulent velocity field matching the data used for the validation of the CFD results.

3.3.4 Outlet boundary condition

Dirichlet boundary condition is used for pressure while Neumann boundary condition is specified for velocity and other variables at the outlet boundary condition.

3.3.5 Wall boundary condition

Dirichlet boundary condition is used for the velocity of the fluid in grid nodes conjoined with the walls, and for the walls, fluid velocity is set equal to the wall movement. In case of a fixed wall, the velocity of the fluid near the wall is zero. The pressure is specified with Neumann boundary condition as the flow flux through the solid wall is zero.

3.3.6 Symmetry boundary condition

The symmetry boundary condition features no flow and no scalar flux across the boundary. It is defined by specifying the component of the gradient normal to the plane to zero. The components parallel to the plane are projected on the symmetry plane from the inside of the domain.

3.3.7 Periodic or cyclic boundary condition

The periodic or cyclic boundary condition can be applied on two boundary faces by setting the flux of all flow variables leaving one boundary face equal to the flux entering the other boundary face.

For compressible flows at low Mach numbers, the physical boundaries are defined with the same approach as described above. However, the boundary conditions need to be modified for transonic and supersonic flows. For these cases, the interested reader is referred to [109].

For turbulent flows, Dirichlet and Neumann boundary conditions are typically used at the inlet and outlet, respectively, for turbulence variables (k and ϵ, for example). The wall boundary conditions depend on the form of the selected turbulence model and the near-wall treatment.

3.4 Solution algorithm

The solution of Eqs. (2.1) and (2.5) offers the issues of non-linearity of the momentum equation and pressure velocity coupling. The non-linearity is originated from the convective term of the momentum equation which contains the quantity $\rho u_i u_j$. The set of equations are coupled as every velocity component appears in each momentum equation and in the continuity equation. The role played by the pressure also needs to be resolved as it appears in the momentum equation but a transport equation for the calculation of pressure is evidently not available in incompressible flows. These issues are resolved by using pressure-based iterative solution strategies such as the Pressure Implicit Splitting of Operator (PISO) for transient calculations or the Semi Implicit Method for Pressure-linked Equations (SIMPLE) algorithm for steady-state calculations. The pressure-based solvers (PISO/SIMPLE) were originally designed for the incompressible flows but they are now improved and can be used for compressible flows with low Mach numbers. This offers an advantage of using a unified solver which is valid over a wide range of flow regime. Many density-based solvers, where the velocity field, temperature and density are calculated with the momentum equation, energy equation and continuity equation respectively and the pressure is obtained from the ideal gas law, which are developed for highly compressible flows are extended to incompressible flows through preconditioning for the same reason. In the present work PISO method is used. Only a short description of the method is presented here, the interested readers are referred to [108] for detailed explanations. The working of the PISO algorithm can be summed up as follows:

1. The boundary and initial conditions are set up for all field values.
2. The discretized momentum equation is solved to compute an intermediate velocity field.

3. The mass fluxes are calculated at the cells faces.
4. The pressure equation, deduced from the continuity equation, is solved.
5. The mass fluxes are corrected at the cell faces.
6. The velocities are corrected on the basis of the new pressure field.
7. The boundary conditions are updated.
8. The PISO loop starting from step 3 can be solved for the prescribed number of times.
9. Using the pressure and velocity fields all the other equations in the system are solved.
10. The time step is increased and the algorithm is repeated from step 1.

Chapter 4

Combustion Model Development

Turbulent premixed combustion at constant pressure can be characterised by the reaction progress variable $c = (T - T_u)/(T_b - T_u)$, which is a normalised quantity that changes monotonically from 0 in reactants to 1 in completely burned products. Here subscripts *'u'* and *'b'* denote unburnt and burnt states. Under the assumptions of a unity Le number, adiabaticity and low Mach number, the Favre-filtered transport equation for c can be written as:

$$\frac{\partial \bar{\rho}\tilde{c}}{\partial t} + \frac{\partial \bar{\rho}\tilde{c}\tilde{u}_{\mathrm{i}}}{\partial x_i} + \frac{\partial}{\partial x_i}(\bar{\rho}\widetilde{u_{\mathrm{i}}c} - \bar{\rho}\tilde{u}_{\mathrm{i}}\tilde{c}) = \frac{\partial}{\partial x_{\mathrm{i}}}\left(\overline{\rho\alpha\frac{\partial c}{\partial x_{\mathrm{i}}}}\right) + \bar{\dot{\omega}} \tag{4.1}$$

where ρ, u_i, α, $\dot{\omega}$ represent the density, flow velocity vector, progress variable diffusivity, progress variable chemical reaction rate and the overbar denotes an LES filtering operation. Using the FSD concept, the sum of the molecular diffusion of the reaction progress variable and the LES filtered reaction rate can be written as:

$$\frac{\partial}{\partial x_{\mathrm{i}}}\left(\overline{\rho\alpha\frac{\partial c}{\partial x_{\mathrm{i}}}}\right) + \bar{\dot{\omega}} = \overline{(\rho S_d)}_S \Sigma_{gen} \;\approx\; \rho_u s_L \Sigma_{gen} \tag{4.2}$$

where $\Sigma_{gen} = \overline{|\nabla c|}$ is the generalised FSD and the surface-filtered value of the density weighted displacement speed $\overline{(\rho S_d)}_S$ is approximated as $\rho_u s_L$, where the surface weighted filtering operation $\overline{(.)}_S$ is given by $\overline{(q)}_S = \overline{q|\nabla c|}/\overline{|\nabla c|}$ [8]. This indicates that the filtered reaction rate closure depends on the proper modelling of Σ_{gen} and s_L. The generalised FSD can also be related to the subgrid scale wrinkling factor $\Xi = \overline{|\nabla c|} \,/\, |\nabla \bar{c}|$, with this Eq. (4.2) becomes:

$$\frac{\partial}{\partial x_{\mathrm{i}}}\left(\overline{\rho\alpha\frac{\partial c}{\partial x_{\mathrm{i}}}}\right) + \bar{\dot{\omega}} = \rho_u s_L \, \Sigma_{gen} = \rho_u s_L \, \Xi \, |\nabla \bar{c}| \tag{4.3}$$

The fractal characteristic of premixed flames is well known and has been well proven experimentally. The wrinkling factor Ξ can be expressed in a form derived for a fractal-based method as proposed by Gouldin [23]:

$$\Xi = \left(1 + \frac{\varepsilon_o}{\varepsilon_i}\right)^{D-2} \tag{4.4}$$

where ε_i, ε_o and D denote inner and outer cut-off scales and fractal dimension of the premixed flame, respectively. The success and applicability of fractal-based models mainly depend on the availability of reliable models for the fractal dimension and cut-off scales.

4.1 Original Keppeler FSD combustion model

A short introduction of the Keppeler FSD combustion model is presented in section 1.2. The derivation and validation of the Keppeler LES subgrid combustion model were presented in detail in [53]. A short summary of the main ingredients of the model is provided here for the sake of completeness. Readers interested in the details of the model derivation and its validation are referred to [53].

The FSD is modelled assuming a fractal character of the flame folding as proposed by Gouldin *et al*. [23, 24]. The flame front S per volume L^3 wrinkled between an inner cut off scale ε_i and outer cut off scale L can be described as:

$$\frac{S}{L^3} \sim \left(\frac{\varepsilon_i}{L}\right)^{2-D} L^{-1} \tag{4.5}$$

where D is called the fractal dimension and it ranges close to 2 when the unresolved flame surface is smooth and becomes 3 when the control volume is completely filled by the unresolved surface. Gouldin *et al.* [24] in the RANS context utilized a probability density function:

$$P_c = \tilde{c}(1-\tilde{c})\,\frac{L}{\delta_t} \tag{4.6}$$

for finding a flamelet along the flame normal z. This ensures the probability of finding the flame surface within the turbulent flame brush thickness becomes 1. Using a proportionality constant C_{K1}, the FSD can be written as:

$$\Sigma = C_{K1}\left(\frac{\varepsilon_i}{L}\right)^{2-D} \frac{\tilde{c}(1-\tilde{c})}{\delta_t} \tag{4.7}$$

In the LES context, P_c is interpreted as the subgrid filtered density function and δ_t becomes the locally resolved flame brush thickness.

Normally the filter width Δ is used as an outer cut off scale. Here utilizing the Nyquist criteria, that at least 2 cells are required to resolve the largest non-resolved flame wrinkling length scale, the outer cut off scale is modelled as:

$$\varepsilon_o = 2.2\Delta \tag{4.8}$$

Gülder and Smallwood [110] examined numerous experimental and DNS databases and reported that the non-dimensional inner cut off scale ε_i/δ_L is proportional to Ka^{β} where β is a constant that ranges between -1/2 ≤ β≤ -1/3. Additionally, the investigation of inner cut off scale for the Kobayashi database in [111] reported a scaling of $\varepsilon_i \sim \delta_L Ka^{-1/2}$. Therefore, the inner cut off scale is modelled as:

$$\varepsilon_i = \max\left(\delta_L Ka_\Delta^{-1/2}, 2\delta_L\right) \quad \text{where} \quad Ka_\Delta = \left(\frac{u'_\Delta}{s_L^0}\right)^{\frac{3}{2}}\left(\frac{\Delta}{\delta_L}\right)^{-\frac{1}{2}} \tag{4.9}$$

and is limited to a value proportional to laminar flame thickness.

The expression for the fractal dimension is developed based on the work of Giacomazzi *et al.* [112] and is limited to a maximum value of 8/3:

$$D = \frac{8/3Ka_\Delta + 2C_D}{Ka_\Delta + C_D} \tag{4.10}$$

A value of 0.03 is chosen for constant C_D to obtain a good agreement with the expression developed for fractal dimension in [112]. A KPP-analysis of the present LES combustion model, as described, e.g. in Poinsot and Veynante [53], supports the use of an upper value of 8/3 for fractal dimension to get the correct pressure scaling at high turbulence values. An upper value of 8/3 is also reported by Chatakonda *et al.* [113] at high turbulence values. However, discrepancy in the upper values of fractal dimension is reported in experimental investigations, e.g [114]. The investigation of Constantin *et al.* [115] and Klimenko [116] clarified this discrepancy by indicating maximum values of about 8/3 in the fully turbulent inner portion of a jet and upper values of about 7/3 in the region mainly affected by the boundaries of the jet by Lagrangian investigations as well as experimental calculations.

The maximum gradient method [50] in flame normal direction *z* is utilized to model the turbulent flame brush thickness:

$$\delta_t^{-1} = \max\left(\frac{\partial \tilde{c}}{\partial z}\right) \tag{4.11}$$

Normalizing the flame normal direction with δ_t gives a universal profile of the progress variable in a fully developed turbulent flame brush, that can be approximated quite well by the complementary error function [50].

$$\tilde{c} = 1 - \frac{1}{2}\, erfc\left(\xi\sqrt{\pi}\right) \tag{4.12}$$

The slope of progress variable can be described as a function of the progress variable $F(\tilde{c}) = \partial\tilde{c}/\partial\xi$ by differentiating Eq. (4.12) with respect to the flame normalized flame normal direction $\xi = (z - z_0)/\delta_t$. The turbulent flame brush thickness can finally be written as:

$$\delta_t{}^{-1} \approx \ |\nabla\tilde{c}|\ F(\tilde{c})^{-1} \tag{4.13}$$

where

$$F(\tilde{c}) = e^{-\left[erfc^{-1}(2(1-\tilde{c}))\right]^2} \tag{4.14}$$

In the implementation of the code, $F(\tilde{c})$ is calculated by a simple polynomial fit: $F(\tilde{c}) = a1 - a2(\tilde{c} - 0.5)^2 - a3(\tilde{c} - 0.5)^4$ with $a1 = 0.995176$, $a2 = 2.81811$ and $a3 = 4.30724$.

The laminar flame speed takes different values when the flame is stretched (curved or strained or both). According to the asymptotic studies [78, 96, 102], the stretched flame structure in the limit of small strain and curvature terms depends on the stretch κ. In the present work, the linear theory of instabilities as described by Clavin [117] is utilized to model the stretched laminar flame speed:

$$s_L = s_L^0 - \ Ma_c\ \kappa\ \delta_L \tag{4.15}$$

The change in the laminar flame speed from the un-stretched one occurs through a linear relationship and is proportional to the stretch κ, where Markstein number Ma_c is the proportionality constant. The unknown parameters are estimated according to correlations of Müller *et al.* [118] and Göttgens *et al.* [119]. The stretch κ is estimated considering only strain effects. Following the work of Hawkes and Cant [12], the strain effects are calculated as:

$$\kappa \approx \ \kappa_s = \left(\delta_{ij} - n_{ij}\right)\frac{\partial \widetilde{u_i}}{\partial x_j} + \Gamma\left(\frac{k_{sgs}}{s_L^0}, \frac{\delta_L}{\Delta}\right)\frac{\sqrt{k_{sgs}}}{\Delta} \tag{4.16a}$$

utilizing a modified efficiency function Γ as proposed by [120]. Here δ_{ij} is the Kronecker delta, k_{sgs} is the sub-grid scale turbulent kinetic energy, $n_{ij} = \overline{(N_i)}_s\overline{(N_j)}_s + (\delta_{ij}/3)[1 - \overline{(N_k)}_s\overline{(N_k)}_s]$ is the flame orientation factor with $\overline{(N_i)}_s = -(\partial\bar{c}/\partial x_i)/\Sigma$ being the i^{th} component of flame surface-weighted normal vector. The first and second terms in the RHS of Eq. (4.16a) arise due to the strain rates resulting from the resolved and unresolved scales respectively. The efficiency function Γ is calculated as:

$$log_{10}(\Gamma) = -\frac{1}{s+0.4}exp\{-(s+0.4)\} + [1 - exp\{-(s+0.4)\}]\left\{\sigma\left(\frac{u'_\Delta}{s_L^0}\right)s - 0.11\right\} \quad (4.16b)$$

$$s = log_{10}\left(\frac{\Delta}{\delta_L}\right);\ \sigma\left(\frac{u'_\Delta}{s_L^0}\right) = \frac{2}{3}\left[1 - 0.5exp\left\{-\left(\frac{u'_\Delta}{s_L^0}\right)^{1/3}\right\}\right];\ u'_\Delta = \left(\frac{2}{3}k_{sgs}\right)^{0.5} \quad (4.16c)$$

Putting all modelled parameters in Eq. (4.7), the FSD can finally be written as:

$$\Sigma = C_{K1}\left(\frac{2.2\Delta}{\max(\delta_L Ka_\Delta^{-1/2}, 2\delta_L)}\right)^{D-2}\tilde{c}(1-\tilde{c})|\nabla\tilde{c}|F(\tilde{c})^{-1} \quad (4.17)$$

where $C_{K1} = 4.5$ provides the best agreement in the validation of numerical results with experimental data.

The blending functions as proposed by Chakraborty and Klein [51] are used to obtain the theoretically exact behaviour of Eq. (4.17) [$\Sigma \to |\nabla\tilde{c}|$] in the limit of fully resolved wrinkling:

$$\Sigma = \left\{\exp\left(\frac{-\Delta}{\varepsilon_i}\Theta\right) + \left(1 - \exp\left(\frac{-\Delta}{\varepsilon_i}\Theta\right)\right)C_{K1}\left(\frac{2.2\Delta}{\max(\delta_L Ka_\Delta^{-1/2}, 2\delta_L)}\right)^{D-2}\tilde{c}(1-\tilde{c})F(\tilde{c})^{-1}\right\}|\nabla\tilde{c}| \quad (4.18)$$

Following [49], Θ = 2.5 is used.

4.2 Simplified Keppeler FSD combustion model

The model Eq. (4.17) can be simplified by examining a plot of $\tilde{c}(1-\tilde{c})$, $F(\tilde{c})$ and $\tilde{c}(1-\tilde{c})F(\tilde{c})^{-1}$ versus c̃. It is shown in Fig. 4.1 that the product of $\tilde{c}(1-\tilde{c})F(\tilde{c})^{-1}$ in Eq. 4.17 is nearly constant with a value of around 0.22 over the whole range of $\tilde{c}$. The expression $\tilde{c}(1-\tilde{c})F(\tilde{c})^{-1}$ has maximum and mean values of around 0.25 and 0.22 respectively. The value drops

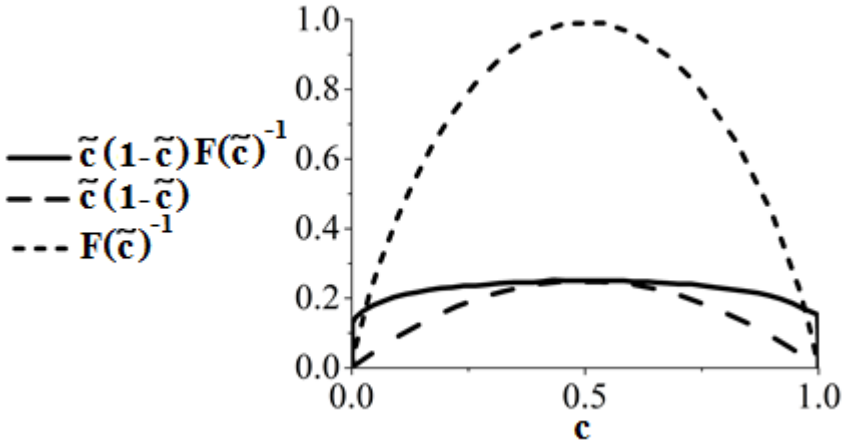

Figure 4.1: Evaluation of $\tilde{c}(1-\tilde{c})$, $F(\tilde{c})$ and $\tilde{c}(1-\tilde{c})F(\tilde{c})^{-1}$

to zero at the extreme ends of $\tilde{c}$, but this occurs at $\tilde{c} \approx 0$ and $\tilde{c} \approx 1$. Incorporating this finding in Eq. (4.17) yields a simplified combustion model:

$$\Sigma = \left(\frac{2.2\Delta}{\max\left(\delta_L K a_\Delta^{-1/2}, 2\delta_L\right)} \right)^{2-D} |\nabla \tilde{c}| = \Xi\, |\nabla \tilde{c}| \tag{4.19}$$

The model Eq. (4.19) is simpler and with a model constant of 1. Also, it shows a correct behaviour in the limit of fully resolved flame wrinkling, so no correction or blending functions are required. This eliminated any possible numerical effects produced with the blending functions. With the simplified model, there is no need to calculate the slope of progress variable as a function of the progress variable $F(\tilde{c})$. The model Eq. (4.19) can also be used to make an analytic evaluation of flame wrinkling factor ($\Xi = \Sigma/|\nabla \tilde{c}|$). However, it is important to note that the simplified Eq. (4.19) is obtained by approximating the product of the terms $C_{K1}\tilde{c}(1-\tilde{c})F(\tilde{c})^{-1}$ to 1.0. Thus, it is expected that the simplified model underestimates the values of FSD as compared with Eq. (4.17). On very fine grids with filter width below the flame thickness ($\Delta < \delta_L$), Eq. (4.19) gives wrinkling factor less than one. This situation can be avoided using blending functions as used in Eq. (4.18). However, this situation would appear on approaching a DNS grid resolution ($\Delta < 0.1$ mm) where a flame is fully resolved. In chapter 6, the performance of the simplified version of the original LES model is discussed and compared to the original model. The numerical results are validated with the experimental database of Kobayashi *et al.* [47,83].

4.3 Subgrid scalar flux modelling

The other term, which needs to be modelled in Eq. (4.1), is the subgrid scalar transport $\left(F_i^{sg} = \bar{\rho}\widetilde{u_i c} - \bar{\rho}\widetilde{u}_i\tilde{c}\right)$. In the original and simplified Keppeler models, it is modelled using the gradient hypothesis:

$$F_i^{sg} = -\bar{\rho}\frac{\nu_{sgs}}{Sc_t}\frac{\partial \tilde{c}}{\partial x_i} \tag{4.20}$$

here Sc_t and ν_{sgs} denote the turbulent Schmidt number and subgrid scale kinematic viscosity.

The counter gradient subgrid scalar fluxes are not explicitly modelled when using the gradient hypothesis based model. It has been shown in many theoretical, experimental and Direct Numerical Simulations (DNS) studies that the turbulent sub-grid scalar flux (SGSF) can exhibit counter gradient behaviour under some conditions. In the present work, the performance of the original Keppeler model is investigated with subgrid scalar flux models presented by Huai *et al*. [45] (see Eq. (4.21)) and Clark *et al.* [46] (see Eq. (4.22)), which showed satisfactory performance in a-priori analysis of different subgrid scalar flux models [43,44].

$$F_i^{sg} = -\bar{\rho}\nu_{sgs}{Sc_t}^{-1}(\partial\tilde{c}/\partial x_i) + \bar{\rho}\, D_{an}\Delta^2\widetilde{S_{ik}}(\partial\tilde{c}/\partial x_k) \tag{4.21}$$

$$F_i^{sg} = \bar{\rho}(\Delta^2/12)(\partial\widetilde{u}_i/\partial x_k)(\partial\tilde{c}/\partial x_k) \tag{4.22}$$

In Eq. (4.21), D_{an} is model parameter, which is taken to be 0.14 [45, 51] in the present analysis. The SGFS model by Clark *et al.* [46] explicitly accounts for the relative alignment of the resolved velocity gradients and scalar gradients. Thus, the model inherently takes into account the possibility of dominance of the transport due to turbulent velocity fluctuations over the transport due to flame normal acceleration and vice versa. This behaviour, which can also be explained based on a scaling analysis [44], makes the model to predict both gradient and counter-gradient type transport. Similar to the Clark model, the SGSF model according to Huai *et al.* [45] also addresses the relative alignment between resolved strain rate and scalar gradients and thus takes into account the local flame normal acceleration effects. The model can predict both gradient and counter-gradient type transport depending on the relative strength of turbulent velocity fluctuation and flame normal acceleration. It can be seen from Eqs. (4.21) and (4.22) that the CGT components of all the SGSF models considered here disappear in the limit of $\Delta \rightarrow 0$

(i.e. when the flow is completely resolved). The models given by Eq. (4.20), Eq. (4.21) and Eq. (4.22) are referred to as GRAD, HUAI and CLARK respectively in this work. The performance of the original Keppeler model with GRAD, HUAI and CLARK models is discussed in detail in Chapter 6.

Richard [121] and Richard *et al.* [13] used a different model for F_i^{sg} (see Eq. (4.23)) as proposed by Rymer [122]. Boger [123] and Weller *et al.* [124] considered a model similar to Eq. (4.23) but multiplying the term responsible for counter-gradient transport (CGT) by wrinkling factor Ξ (see Eq. (4.24))

$$F_i^{sg} = -\bar{\rho}\frac{\nu_{sgs}}{Sc_t}\frac{\partial \tilde{c}}{\partial x_i} - \rho_u s_L \, N_{\mathrm{i}} \, (\bar{c} - \tilde{c}) \tag{4.23}$$

$$F_i^{sg} = -\bar{\rho}\frac{\nu_{sgs}}{Sc_t}\frac{\partial \tilde{c}}{\partial x_i} - \rho_u s_L \, \Xi \, N_{\mathrm{i}} \, (\bar{c} - \tilde{c}) \tag{4.24}$$

where $N_{\mathrm{i}} = -\nabla\bar{c}/|\nabla\bar{c}| = -\nabla\tilde{c}/|\nabla\tilde{c}|$ is the normal to the iso-surface of the filtered progress variable. The models given by Eq. (4.23) and Eq. (4.24) are referred to as RICHARD and WELLER models, respectively, in this work. Due to increased extent of subgrid scale wrinkling with increasing Δ, the wrinkling factor takes a greater magnitude for larger values of Δ. This suggests that contribution due to CGT in the WELLER model takes a greater magnitude as compared to the contribution in the RICHARD model, especially for larger values of Δ. For small values of Δ, where $\Xi \approx 1$, the performance of the RICHARD and WELLER models remain close to each other.

Tullis and Cant [124] (see Eq. (4.25)) and Rymer [123] (see Eq. (4.26)) extended the RANS model by Venante *et al.* [35] and proposed the following models for F_i^{sg}.

$$F_{\mathrm{i}}^{sg} = -\alpha_E\bar{\rho}\frac{\nu_{sgs}}{Sc_t}\frac{\partial \tilde{c}}{\partial x_i} - \bar{\rho}s_L \, \Xi \, N_{\mathrm{i}}\tau \, \tilde{c}(1 - \tilde{c}) \tag{4.25}$$

$$F_{\mathrm{i}}^{sg} = -\alpha_E\bar{\rho}\frac{\nu_{sgs}}{Sc_t}\frac{\partial \tilde{c}}{\partial x_i} - \bar{\rho}s_L \, N_{\mathrm{i}}\tau \, \tilde{c}(1 - \tilde{c}) \tag{4.26}$$

where α_E is the efficiency function included to account for the effects of subgrid scale Schmidt number and the wrinkling that the turbulent eddies can produce. It ranges from the order of unity to zero when the turbulent structures are too small to wrinkle the flame front. For the present

work $\alpha_E = 1$ is used. The scalar transport due to velocity fluctuations and flame normal acceleration are presented by first and second terms on RHS of Eqs. (4.25) and (4.26). The models given by Eq. (4.25) and Eq. (4.26) are referred to as TULLIS and RYMER models, in this work, respectively. Similar to the WELLER model, the TULLIS model predicts a greater magnitude of CGT due to the presence of Ξ as compared to the corresponding contribution in the RYMER model. For small values of Δ, the predictions of the TULLIS and RYMER models remain close to each other but their predictions differ from each other for large values of Δ. Moreover, using a BML model-type Flamelet flame density function (FDF) $\bar{c} = (1+\tau)\tilde{c}/(1+\tau\tilde{c})$, $\rho_u(\bar{c}-\tilde{c})$ can be transformed into $\bar{\rho}\tau\tilde{c}(1-\tilde{c})$, where $\bar{\rho} = \rho_u/(1+\tau\tilde{c})$. Thus the second term on RHS of the WELLER (RICHARD) model approaches to the second term on RHS of the TULLIS (RYMER) model.

4.4 Investigation of Pressure and Le number effects in different FSD models

In Chapter 6, the performance of some the well-known SAFSD models, available in open literature, is examined under high-pressure conditions and non-unity Le number. The selected models are developed by Angelberger *et al.* [97], Fureby [104], Muppala *et al.* [105] and Zimont [106]. The original Keppeler model, which showed good performance for turbulent Bunsen flames over a wide range of turbulence and pressures between 1 and 20 bar, is also investigated for Le number dependency. The numerical results are compared with the broad set of experimental data of Kobayashi *et al.* [47,82,83]. The selected models are referred in the rest of the paper with the last name of the first author mentioned in the original work.

Angelberger *et al.* [97] developed their model based on a DNS study of flame stretch and vortex pair interaction [117] and expressed Ξ in the following form:

$$\Xi = \left[1 + C_A\, \Gamma\, \frac{u'_\Delta}{s_L}\right] \tag{4.27}$$

where $C_A = 1$ is a model constant and Γ is the efficiency function, which accounts for the net straining effect of all the vortices smaller than the LES filter width Δ. This parameter is modelled as:

$$\Gamma = A * exp\left[\frac{-B}{(u'_\Delta/s_L)^{0.3}}\right] * \left(\frac{\Delta}{\delta_L}\right)^{2/3} \tag{4.28}$$

where A =0.75 and B =1.2.

Fureby [104] developed his model based on the fractal approach to model Ξ, which is given by Eq. (4.4). In this model the inner and outer cut-off scales, fractal dimension and wrinkling factor are modelled with the following expressions:

$$\varepsilon_i = \frac{s_L\,\Delta}{u'_\Delta\,\Gamma} \tag{4.29a}$$

$$\varepsilon_o = \Delta \tag{4.29b}$$

$$D = \frac{2.05 s_L}{u'_\Delta + s_L} + \frac{2.35 u'_\Delta}{u'_\Delta + s_L} \tag{4.29c}$$

$$\Xi = \left(1 + \frac{\Gamma * u'_\Delta}{s_L}\right)^{D-2} \tag{4.29d}$$

Zimont and Lipatnikov [106] used the expression for Σ_{gen} as a function of u'_Δ and the Damköhler number Da.

$$\Xi = \left[1 + C_Z \left(\frac{u'_\Delta}{s_L}\right)^{3/4} \left(\frac{\Delta}{\delta_L}\right)^{1/4}\right] \tag{4.30}$$

where $C_Z = 0.51$ is a model constant. The model was initially derived for RANS simulations and for high turbulence cases. For additional details about the models, the reader is referred to the original papers where these models have been presented. The key features of all the models used in the present study are summarised in Table 4.1.

4.5 RANS version of the Keppeler model

In section 4.4, the development of the Keppeler model in the LES context is presented. This model has shown a satisfactory performance in applications where a correct prediction of turbulent flame speeds with changing pressure is important. It would be interesting to see the applicability of the same reaction closure with suitable modifications in the RANS context.

Table 4.1: Summary of the selected algebraic FSD models

Model name	Original version	Tuned version
Angelberger [97]	$\Gamma = A * exp\left[\frac{-B}{(u'_\Delta/s_L)^{0.3}}\right] * \left(\frac{\Delta}{\delta_L}\right)^{2/3}$ $A = 0.75 \quad B = 1.2$ $\Xi = \left[1 + C_A\, \Gamma\, \frac{u'_\Delta}{s_L}\right]$ $C_A = 1.0$	$\Gamma = A * exp\left[\frac{-B}{(u'_\Delta/s_L)^{0.3}}\right] * \left(\frac{\Delta}{\delta_L}\right)^{2/3}$ $A = 9.5 \quad B = 1.2$ $\Xi = \left[1 + C_A\, C_{Le}\, C_p\, \Gamma\, \frac{u'_\Delta}{s_L}\right]$ $C_A = 0.4\ ,\ C_{Le} = \frac{1}{Le}, C_p = \left(\frac{p}{p_o}\right)^n$
Fureby [104]	$D = \frac{2.05 s_L}{u'_\Delta + s_L} + \frac{2.35 u'_\Delta}{u'_\Delta + s_L}$ $\Gamma = A * exp\left[\frac{-B}{(u'_\Delta/s_L)^{0.3}}\right] * \left(\frac{\Delta}{\delta_L}\right)^{2/3}$ $A = 0.75 \quad B = 1.2$ $\varepsilon_i = \frac{s_L\, \Delta}{u'_\Delta\, \Gamma};\ \ \varepsilon_o = \Delta$ $\Xi = \left(1 + \frac{\varepsilon_o}{\varepsilon_i}\right)^{D-2}$	$D = \frac{8/3 Ka_\Delta + 2C_D}{Ka_\Delta + C_D}$ $\Gamma = A * exp\left[\frac{-B}{(u'_\Delta/s_L)^{0.3}}\right] * \left(\frac{\Delta}{\delta_L}\right)^{2/3}$ $A = 9.5 \quad B = 1.2$ $\varepsilon_i = \max\left(\frac{s_L\, \Delta}{u'_\Delta\, \Gamma}, \delta_L\right);\ \ \varepsilon_o = \Delta$ $\Xi = \ C_{Le}\left(1 + \frac{\varepsilon_o}{\varepsilon_i}\right)^{D-2};\ \ C_{Le} = 1/Le$
Keppeler [53]	$D = \frac{8/3 Ka_\Delta + 2C_D}{Ka_\Delta + C_D}$ $\varepsilon_i = \max\left(\delta_L Ka_\Delta^{-1/2}, 2\delta_L\right)$ $\Xi = \left(\frac{2.2\Delta}{\varepsilon_i}\right)^{D-2}$	$D = \frac{8/3 Ka_\Delta + 2C_D}{Ka_\Delta + C_D}$ $\varepsilon_i = \max\left(\delta_L Ka_\Delta^{-1/2}, 2\delta_L\right)$ $\Xi = \ C_{Le}\left(\frac{2.2\Delta}{\varepsilon_i}\right)^{D-2};\ \ C_{Le} = 1/Le$
Zimont [106]	$\Xi = \left[1 + C_Z \left(\frac{u'_\Delta}{s_L}\right)^{3/4} \left(\frac{\Delta}{\delta_L}\right)^{1/4}\right]$ $C_Z = 0.51$	$\Xi = \left[1 + C_Z\, C_{Le}\, C_p \left(\frac{u'_\Delta}{s_L}\right)^{3/4} \left(\frac{\Delta}{\delta_L}\right)^{1/4}\right]$ $C_Z = 1.2,\ C_{Le} = \frac{1}{Le}, C_p = \left(\frac{p}{p_o}\right)^n$

Lipatnikov and Chomiak [126], Veynante and Versich [127] and Bray *et al.* [128] have carried out an extensive evaluation and review of RANS models for premixed combustion modelling.

Several LES premixed combustion models based on the FSD approach, as investigated in [51, 52], have a direct counterpart in the context of RANS approach. This situation can provide a good basis for investigating the pros and cons of the LES and RANS modelling approaches. Hence, a RANS version of the Keppeler model is developed and its performance is investigated in comparison with the LES version. The results are presented in Chapter 6.

The Keppeler model is transformed into the RANS context by replacing the subgrid scale quantities, e.g. subgrid scale velocity fluctuations u'_Δ and the filter width Δ with total velocity fluctuations u' and the integral length scale l_0. With these changes, the inner and outer cut-off scales, fractal dimension and wrinkling factor expressions in the RANS model can be written as:

$$\varepsilon_i = \max\left(\delta_L Ka^{-1/2}, 2\delta_L\right) \quad where \quad Ka = \left(\frac{u'}{s_L^0}\right)^{\frac{3}{2}} \left(\frac{l_0}{\delta_L}\right)^{-\frac{1}{2}} \tag{4.31}$$

$$\varepsilon_o = \ l_0 \tag{4.32}$$

$$D = \frac{8/3Ka \ + 2C_D}{Ka + C_D} \tag{4.33}$$

$$\Sigma = C_{K1} \left(\frac{l_0}{\max\left(\delta_L Ka^{-1/2}, 2\delta_L\right)}\right)^{D-2} \tilde{c}(1-\tilde{c})|\nabla\tilde{c}|F(\tilde{c})^{-1} \tag{4.34}$$

It has been found that the RANS Keppeler model under-predicts the turbulent flame speed values when compared with the corresponding experimental data. A new model constant $C_{K2} = 1.4$ provides the best agreement in the validation of numerical results with the experimental data. Along with C_{K2}, Eq. (4.34) requires the blending functions (as used in Eq. (4.18)).

$$\Sigma = \left\{\exp\left(-\frac{l_0}{\varepsilon_i}\Theta\right) + \left(1 - \exp\left(-\frac{l_0}{\varepsilon_i}\Theta\right)\right) C_{K1}C_{K2} \left(\frac{l_0}{\max\left(\delta_L Ka_\Delta^{-1/2}, 2\delta_L\right)}\right)^{D-2} \tilde{c}(1-\tilde{c})F(\tilde{c})^{-1}\right\} |\nabla\tilde{c}| \tag{4.35}$$

where $\Theta = 2.5$ is used.

As discussed in section 4.3, the Eq. (4.34) can be simplified as the terms $C_{K1}\tilde{c}(1-\tilde{c})F(\tilde{c})^{-1} \approx 1$.

$$\Sigma = C_{K2}\left(\frac{l_0}{\max\left(\delta_L Ka^{-1/2}, 2\delta_L\right)}\right)^{D-2}|\nabla\tilde{c}| \tag{4.36}$$

It can be seen that Eq. (4.36) also needs the blending functions to obtain the theoretically exact behaviour [$\Sigma \rightarrow |\nabla\tilde{c}|$] in the limit of no flame wrinkling. This yields the following expression for Σ in the RANS context:

$$\Sigma = \left\{exp\left(-\frac{l_0}{\varepsilon_i}\Theta\right) + \left(1 - exp\left(-\frac{l_0}{\varepsilon_i}\Theta\right)\right) C_{K2}\left(\frac{l_0}{\max\left(\delta_L Ka^{-1/2}, 2\delta_L\right)}\right)^{D-2}\right\}|\nabla\tilde{c}| \tag{4.37}$$

The strain effects, as used in Eq. (4.15) to estimate the stretched laminar flame speed, are calculated as:

$$\kappa \approx \kappa_s = \left(\delta_{ij} - n_{ij}\right)\frac{\partial\widetilde{u_i}}{\partial x_j} + \Gamma\left(\frac{k}{s_L^0}, \frac{\delta_L}{l_0}\right)\frac{\sqrt{k}}{l_0} \tag{4.38a}$$

$$log_{10}(\Gamma) = -\frac{1}{s + 0.4}exp\{-(s + 0.4)\} + [1 - exp\{-(s + 0.4)\}]\left\{\sigma\left(\frac{u'}{s_L^0}\right)s - 0.11\right\} \tag{4.38b}$$

$$s = log_{10}\left(\frac{l_0}{\delta_L}\right);\ \sigma\left(\frac{u'}{s_L^0}\right) = \frac{2}{3}\left[1 - 0.5exp\left\{-\left(\frac{u'}{s_L^0}\right)^{1/3}\right\}\right];\ u' = \left(\frac{2}{3}k\right)^{0.5} \tag{4.38c}$$

The scalar transport ($\bar{\rho}\widetilde{u_i c} - \bar{\rho}\widetilde{u_i}\tilde{c}$), in the RANS version of the Keppeler models, is modelled using the gradient hypothesis:

$$F_i^{sg} = -\bar{\rho}\frac{\nu_t}{Sc_t}\frac{\partial\tilde{c}}{\partial x_i} \tag{4.39}$$

where ν_t denotes the turbulent kinematic viscosity. The turbulent quantities, e.g. k, ν_t and l_0 are calculated using the SST k-ω model (see section 2.3.2.2).

Chapter 5

Numerical and Experimental setup

In this chapter the numerical setup and the experimental database used for the validation of numerical predictions are presented.

5.1 Numerical setup

The combustion models have been implemented in the open source CFD toolbox, OpenFOAM. Table 5.1 shows the inlet and operating conditions for the combustion cases used in the present study. The computational domain is cylindrical with a diameter of 80 mm and a length of 120 mm. A structured mesh, which is concentrated in the flame regions (expansion ratio = width of end cell/width of first cell = 1.8), is used thus avoiding any problems associated with anisotropic, inhomogeneous grids. The dimensions of the computational domain are selected to ensure that the results are not affected by boundaries. The maximum Courant number is set to 0.3 to achieve numerical stability and accuracy. For time advancement, backward Euler scheme is used. An unlimited second order linear scheme is used to discretize the convective term of the momentum equation [58]. A second order linear scheme with a flux limiter (limitedLinear) [58] is used to discretize the convective term in the scalar transport equation. A second order linear scheme is applied to discretize the diffusive terms [58]. At the inlet for all parameters Dirichlet boundary condition is used, except for the pressure. Neumann boundary condition is used for temperature at all the boundaries except at the inlet where the temperature is set to 300 K. The correct turbulence intensity and the integral length at the inlet is provided by using the turbulence generator as proposed by Kempf *et al.* [129] and successfully implemented by Tangermann *et al.* [130] in OpenFOAM. The subgrid scale viscosity is modelled by a one-equation eddy-viscosity model as developed by Schumann [71] and used by Fureby *et al.* [72]. The sub-grid scale velocity fluctuations are calculated using $u'_{\Delta} = \sqrt{2k_{sgs}/3}$ where $k_{sgs}$is the subgrid turbulent kinetic energy. In the RANS context, the turbulent eddy viscosity and turbulent kinetic energy are calculated using SST k-ω model.

Table 5.1: Summary of the operating conditions

Case	fuel	Φ	p [bar]	U [m/s]	u' [m/s]	l_0 [mm]
1	CH_4	0.9	1	2.02	0.10	1.80
2	CH_4	0.9	1	2.33	0.20	1.43
3	CH_4	0.9	1	2.42	0.33	1.40
4	CH_4	0.9	1	2.36	0.46	1.25
5	CH_4	0.9	5	2.05	0.09	0.83
6	CH_4	0.9	5	2.53	0.19	0.99
7	CH_4	0.9	5	3.38	0.61	1.15
8	CH_4	0.9	5	2.21	0.40	1.15
9	CH_4	0.9	10	3.40	0.26	1.05
10	CH_4	0.9	10	2.11	0.36	1.10
11	CH_4	0.9	10	3.57	0.85	1.20
12	CH_4	0.9	10	4.64	1.20	1.40
13	C_3H_8	0.9	1	1.50	0.06	1.74
14	C_3H_8	0.9	1	2.25	0.18	1.50
15	C_3H_8	0.9	1	1.50	0.26	1.25
16	C_3H_8	0.9	1	1.75	0.35	1.00
17	C_3H_8	0.9	1	2.25	0.51	0.90
18	C_3H_8	0.9	1	2.50	0.58	0.90
19	C_3H_8	0.9	5	1.55	0.04	1.15
20	C_3H_8	0.9	5	1.89	0.10	1.02
21	C_3H_8	0.9	5	2.76	0.20	0.96
22	C_3H_8	0.9	5	2.62	0.42	1.10
23	C_3H_8	0.9	5	3.51	0.63	1.20
24	C_3H_8	0.9	5	5.28	0.9	1.20

The filtered reaction progress variable $\bar{c}$ contours, which are more conical in shape than the Favre filtered $\tilde{c}$ ones and correspond to the experimental evaluation procedure, are used to

estimate the turbulent flame speeds. These contours are computed using the time and circumferentially averaged $\tilde{c}$ contours, following the work of Poinsot and Veynante [55] and assuming a BML model-type Flamelet flame density function (FDF):

$$\bar{c} = \frac{(1+\tau)\tilde{c}}{1+\tau\tilde{c}} \tag{5.1}$$

where $\tau = \rho_u/\rho_b - 1$ is the heat release parameter. A least squares fit method is used to obtain the slope of the isoline $\bar{c} = 0.5$ (which is the correct quantity for evaluating the simulated flame speed for comparison to the Kobayashi database). The slope is calculated, while neglecting the curved portions of the flame front at the flame base and tip, evaluating only the linear portion of the flame. This slope allows the calculation of flame angle φ. With the mean flow velocity U known at the inlet, the flame speed can be calculated using Eq. (5.2).

5.2 Assessment of resolution quality

The resolved turbulent kinetic energy was used to assess the resolution quality of the present LES in the previous work [53]. Table 5.2 summarizes the mesh characteristics of three systematically refined grids used in [53] along with the values of Δ/l_F for different pressure values. The estimated amount of resolved kinetic energy was found in the range of 85-95% for two sample cases corresponding to low and high-pressures with mesh resolutions A and C, where the SGS kinetic energy is obtained from the one equation LES model used in this work. According to Pope [131], a well resolved LES should resolve 80% of the turbulent kinetic energy. However, as pointed out by Klein [132], the estimate of k_{sgs} based on a model is often too optimistic because it neglects the effects of numerical dissipation. Therefore, a more sophisticated method for the evaluation of LES quality, as proposed by Celik *et al.* [133], was used. This method is based on the Richardson extrapolation concept and measures the percentage of the resolved turbulent kinetic energy k_{res} to the total turbulent kinetic energy k_{tot}. The ratio of k_{res} to k_{tot} was found in a range of 65-80% and 87-95% for mesh resolution A and C, respectively. Although the LES on the fine mesh is reasonably well resolved in terms of turbulent kinetic energy, a large fraction of the flame wrinkling is unresolved at high-pressures, i.e. the SGS model needs to do proportionally more work at high-pressures. As an example, only 15% of the flame surface is resolved at 20 bar on the fine mesh [53]. The comparison of numeri-

Table 5.2: Summary of the mesh characteristic

Mesh	Δ [mm]	Grid size	$\left.\frac{\Delta}{\delta_L}\right\|_{0.1\ \mathrm{MPa}}$	$\left.\frac{\Delta}{\delta_L}\right\|_{0.5\ \mathrm{MPa}}$	$\left.\frac{\Delta}{\delta_L}\right\|_{1\ \mathrm{MPa}}$
A	0.4	0.6×10^6	8.8	19	27.8
B	0.3	2.0×10^6	6.6	14.2	20.9
C	0.2	3.7×10^6	4.4	9.5	13.9

cal predictions of turbulent flame speed using three different mesh sizes with experimental data for methane and propane fuels was done in [53] to make sure that the results are grid independent. In the present work, meshes A and C are used.

5.3 Experimental set up

The numerical results are validated with results from experimental work by Kobayashi *et al*. [47,82,83]. Figure 5.1 shows the schematic of the facility where the experiments were conducted.

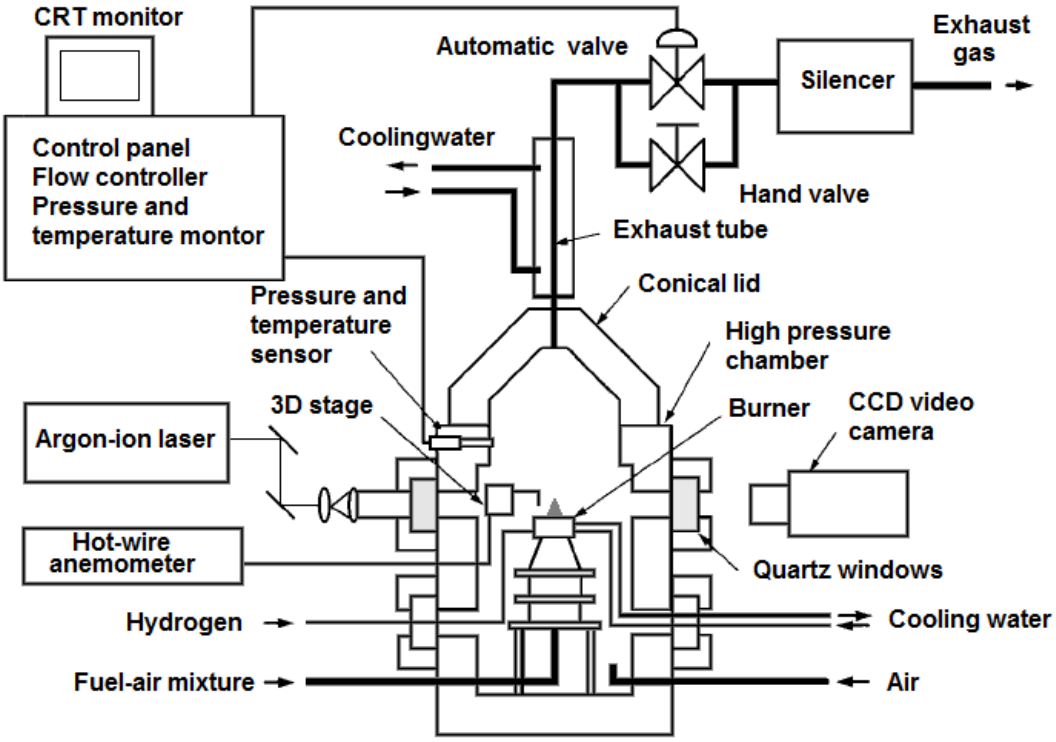

Figure 5.1: Schematic of the Kobayashi experimental apparatus [83]

In the experimental work the effects of ambient pressure on the turbulent burning velocity of premixed flames were investigated in a high-pressure environment. A nozzle-type burner (diameter 20 mm), with a turbulence generator to adjust a certain combination of turbulence level and length scale, was installed in a high-pressure chamber (diameter 498 mm and length 600 mm). Four different kinds of perforated plates were used as a turbulence generator and installed 40 mm upstream of the chamber. The constant temperature hot-wire anemometry method was used for the turbulence and flow velocities measurements at the centre of the burner exit. The measurements involved lean methane/air mixtures for 1, 5, 10, 20 and 30 bar and propane/air for 1 and 5 bar at an equivalence ratio of $\Phi = 0.9$. Ethylene/air mixtures were also investigated with varied stoichiometry of $\Phi = 0.5$, 0.7 and 0.9 for 1, 5 and 10 bar. Measured rms-values and integral length scales range between $0.05 \leq u' \leq 0.85$ m/s and $0.83 \leq l_0 \leq 1.4$ mm while the mean flow velocity ranges between 1.9 and 4.64 m/s. Flame observations were conducted using instantaneous Schlieren photographs and high-speed laser tomography. An instantaneous Schlieren image of a typical turbulent flame is shown in Fig. 5.2a. An averaged flame front, which is reported to be equivalent to a $\bar{c} = 0.5$ iso-contour, was created using 50 instantaneous Schlieren photographs of turbulent flame fronts assuming rotational symmetry, which was then used to estimate the turbulent flame speed:

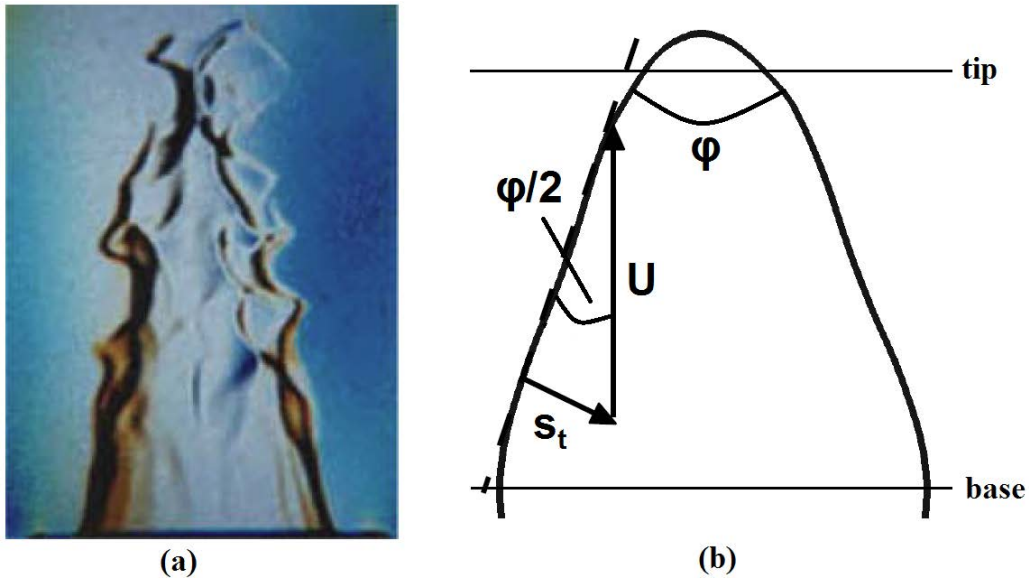

Figure 5.2: (a) Instantaneous Schlieren image of a typical lean premixed turbulent flame from Kobayashi *et al.* [83] (b) method used in the experiment to determine turbulent flame speed

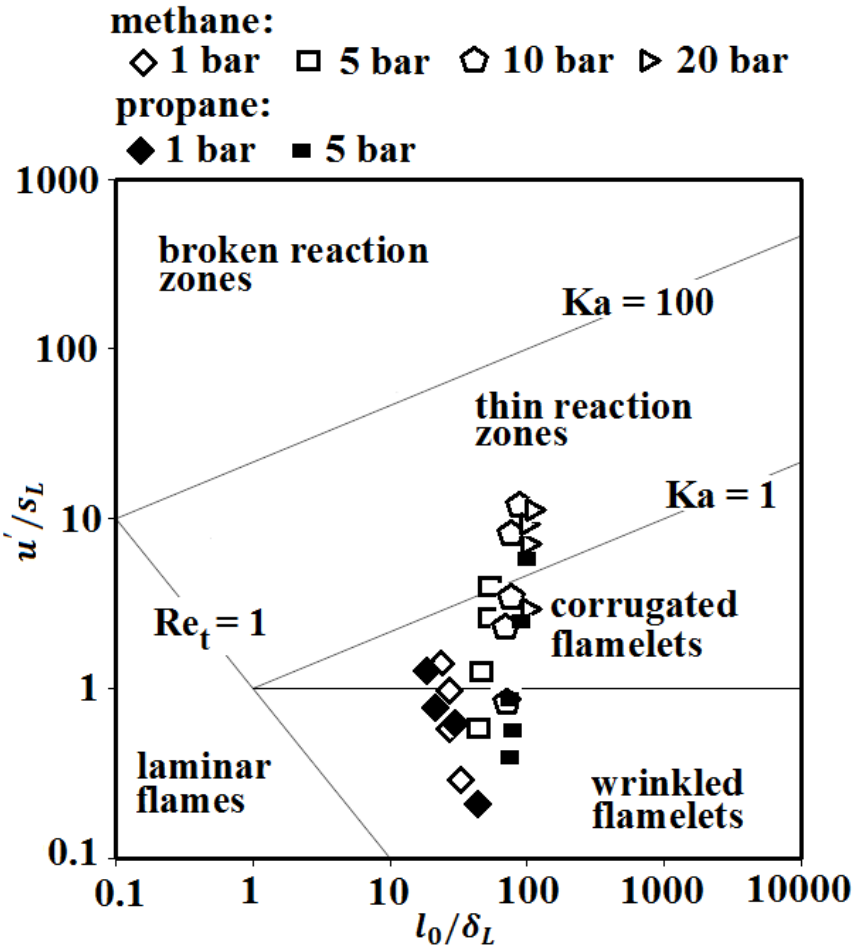

Figure 5.3: Peters diagram of the experimental data for methane and propane.

$$s_t = U\ sin(\varphi/2) \tag{5.2}$$

where U denotes the bulk velocity of the unburnt mixture and φ is the flame angle. The experimental method utilized to calculate the turbulent flame speed is sketched in Fig. 5.2b. The identical approach is also used here to calculate the turbulent flame speed from the averaged LES $\bar{c}$-field. Figure 5.3 shows the Peters diagram where the methane and propane flames studied in the experiments are indicated. It can be seen that the majority of the cases fall within the corrugated and wrinkled flamelet regime while few high-pressure cases fall within the thin reaction zone regime.

In addition to Eq. (5.2), the turbulent flame speed s_t has been estimated by using the following expressions:

$$\frac{s_t}{s_L^o} = \frac{\int \Sigma \ dV}{A_{mean,\bar{c}}} \tag{5.3}$$

$$s_t = \frac{\int \bar{\dot{\omega}} \, dV}{\rho_u A_{mean,\bar{c}}} = \frac{\int \langle \rho_u s_L \Sigma \rangle dV}{\rho_u A_{mean,\bar{c}}} \tag{5.4}$$

where $A_{mean,\bar{c}}$ is the area of $\langle \bar{c} \rangle = 0.5$ isosurface. The flame speed evaluations using Eqs. (5.2)-(5.4) are shown in Figs. 5.4a and 5.4b for p =0.1 and 1.0 MPa cases. It can be seen from these figures that the turbulent flame speed values obtained using Eq. (5.3) are greatly over-predicted irrespective of the choice of the SGSF model. This over-prediction originates due to the absence of strain rate effects and the usage of un-stretched laminar flame speed in Eq. (5.3). Use of Eqs. (5.2) and (5.4) yields similar results. Thus, the turbulent flame speed s_t is evaluated using the experimental method in the rest of the paper from the averaged LES $\bar{c}$-field.

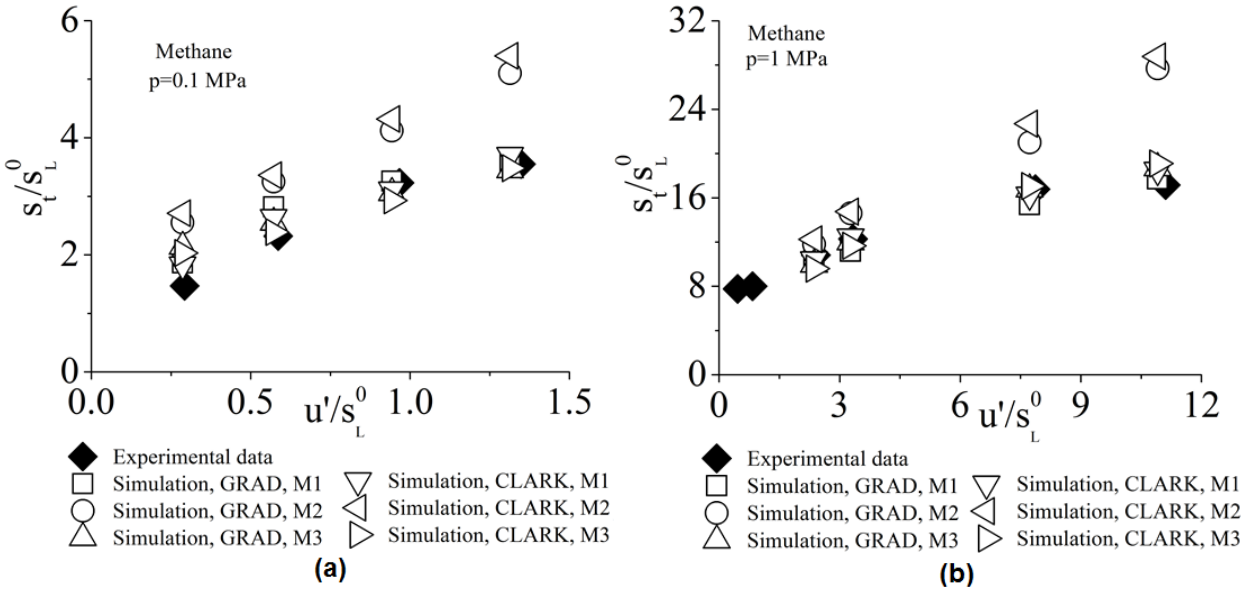

Figure 5.4: Variation of s_t/s_L^0 with u'/s_L^0 for (a) $p = 0.1$ MPa and (b) $p = 1.0$ MPa using methods given by Eqs. (5.2)-(5.4), which are indicated by M1, M2 and M3 in Figs. 5.4(a) and (b)

Chapter 6

Results and discussion

In this chapter, the numerical results obtained with the FSD models for the predictions of premixed flames are presented and discussed in detail.

6.1 Investigation of Simplified Keppeler model

The performance of the simplified Keppeler model is compared with the original model using methane as a fuel and the results are presented in this section. The turbulent flame speeds are calculated and validated with the experimental database of Kobayashi *et al.* [47,83]. Pressure, bulk velocity of fuel at the inlet, integral length scale and rms turbulent velocity vary between 1 MPa $\leq p \leq$ 20 bar, 1.5 m/s $\leq U \leq$ 3.51 m/s, 0.83 mm $\leq l_0 \leq$ 1.8 mm and 0.04 $\leq u' \leq$ 0.73, respectively.

Figure 6.1 shows the comparison of the time-averaged progress variable $\langle \bar{c} \rangle$ and the instantaneous Favre-filtered progress variable $\tilde{c}$ for case 4 with the original and simplified

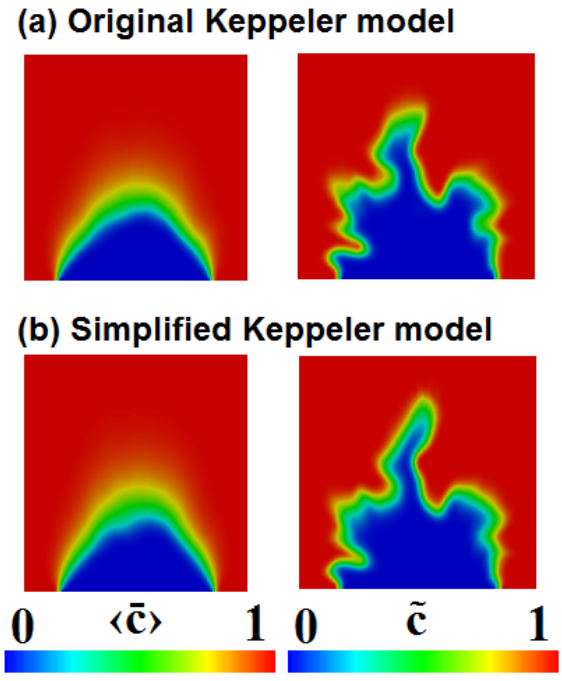

Figure 6.1: Comparison of time-averaged $\langle \bar{c} \rangle$ and instantaneous progess variable $\tilde{c}$ contours with (a) original (b) simplified Keppeler model.

Keppeler models. The time-averaged and the instantaneous flame surfaces with the original Keppeler model are shown in Fig. 6.1(a), while Fig. 6.1(b) shows the flame surfaces with the simplified Keppeler model. Comparing the instantaneous flame fronts in Fig. 6.1a and Fig. 6.1b shows that the explicit wrinkling with the simplified model is lower as compared to the original model. However, the original and simplified Keppeler models predict similar time-averaged flame surfaces.

Figure 6.2 illustrates the method used to calculate the turbulent flame speed. The contours of Reynolds averaged $\langle \bar{c} \rangle$ with an isoline corresponding to $\bar{c} = 0.5$ are shown in Fig. 6.2. The time and circumferential averaging is applied to improve the calculation of the flame speeds. The flame speed is calculated by the slope of the isoline $\bar{c} = 0.5$ after selecting the suitable portion of the flame length from the flame front.

The performance of the two models is compared by evaluating the turbulent flame speed for methane fuel at different pressure levels. The predicted flame speeds are plotted versus u' in Fig. 6.3a, Fig. 6.3b and Fig. 6.3c at different pressure levels to check whether the proposed models can match the experimental database. The flame speeds are calculated according to the method illustrated in Fig. 6.2. The turbulent flame speeds at p = 1 bar are shown in Fig. 6.3a while Fig. 6.3b and Fig. 6.3c show the comparison of flame speeds at p = 5 bar and 20 bar, respectively. The turbulent flame speeds match with the experimental data quite well. Comparing the estimated flame speeds using methane fuel at different pressure levels with the original and simplified models shows that both models give satisfactory performance. However, the flame

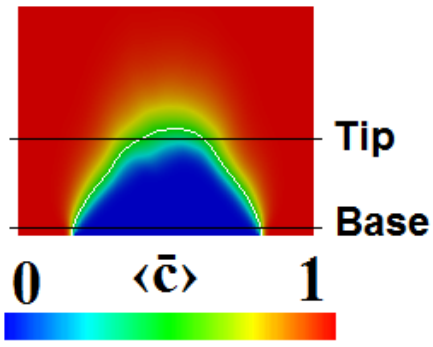

Figure 6.2: Graphical representation of the method used to calculate flame speed

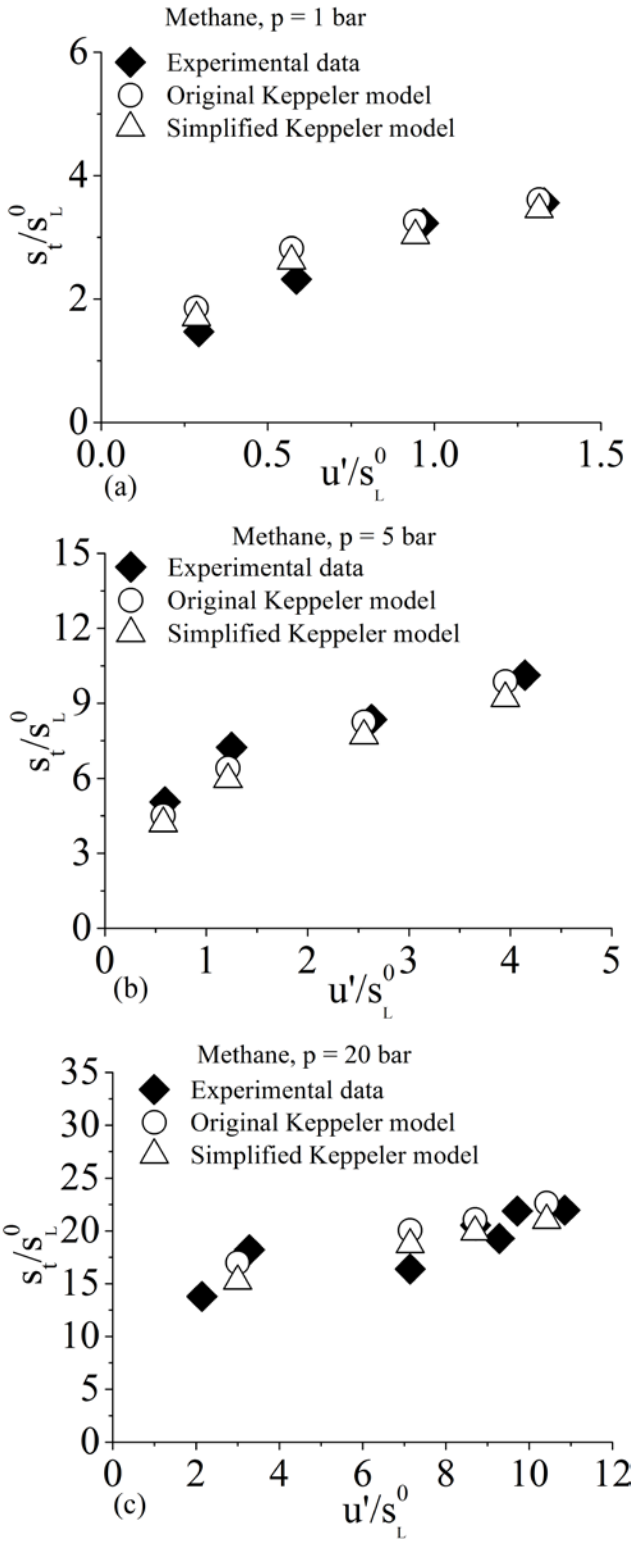

Figure 6.3: Comparison of turbulent flame speed at (a) 1 bar (b) 5 bar (c) 20 bar using methane fuel with original and simplified Keppeler models

speeds obtained with the simplified model are lower than those obtained with the original model. The simplified model provides improved results in the cases where the original model would give over-estimated values of the turbulent flame speeds.

6.2 Investigation of original Keppeler model with different SGSF models

In this section, two more sophisticated SGSF closures (Eqs. (4.21) and (4.22)) are investigated in combination with the original Keppeler model presented in section 4.1. The study is focused at comparing these two formulations in comparison with the classical gradient hypothesis approach, which was used in the earlier work [53]. Section 6.2.1 is based on a-posteriori analysis. Detailed explanations for the observed behaviour will be provided in section 6.2.2 based on a-priori analysis.

6.2.1 A-posteriori analysis

The model performance is first evaluated in terms of the predicted flame surface and the predicted turbulent flame speeds. The time-averaged progress variable $\langle \bar{c} \rangle$ and the instantaneous Favre filtered progress variable $\tilde{c}$ for case 4 and case 12 using mesh A (henceforth denoted as 4A and 12A) are shown in Fig. 6.4 and Fig. 6.5 for different SGSF models. The other cases are not shown for the sake of conciseness because qualitatively similar results have been obtained for other cases too. For case 4A, the time-averaged and the instantaneous flame surfaces with the GRAD model are shown in Fig. 6.4a, while Figs. 6.4b and 6.4c show the flame surfaces using the CLARK and HUAI models, respectively. A comparison of the flame fronts in Fig. 6.4 shows that the flame shape and thickness are slightly modified. The flame front gets thinner with the use of HUAI and CLARK models. However, the change is marginal. The instantaneous flame contours $\tilde{c}$ = 0.05 and $\tilde{c}$ = 0.95 with GRAD model are superimposed on the flame contours obtained using CLARK and HUAI models in Fig. 6.4d. The inner lines represent $\tilde{c} = 0.05$ while outer lines represent $\tilde{c} = 0.95$. The comparison shows that the flame shape and thickness are weakly modified. It can also be observed from Fig. 6.4 that the time-averaged flames tend to be

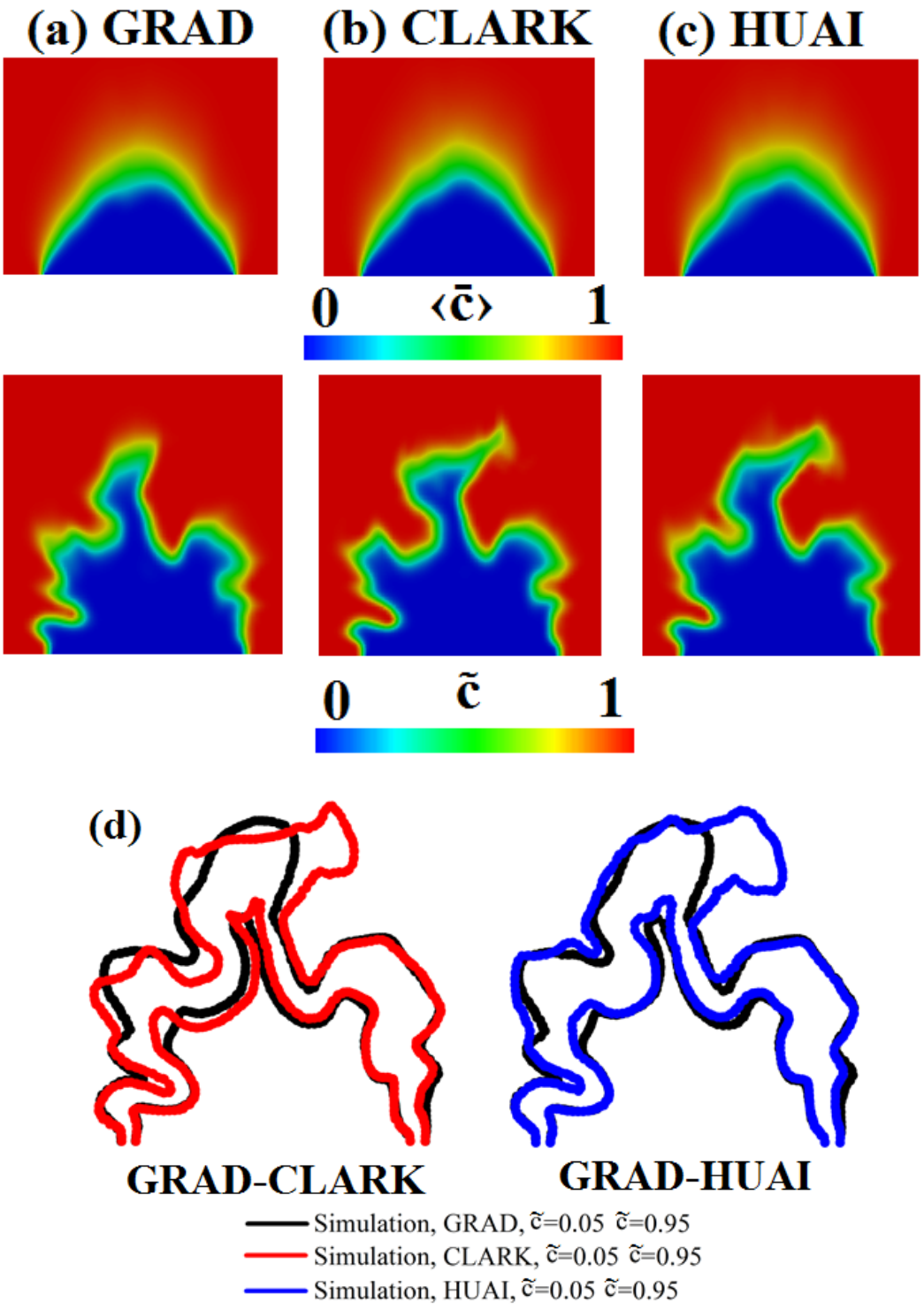

Figure 6.4: Comparison of time-averaged $\langle \bar{c} \rangle$ and instantaneous flame surface $\tilde{c}$ with (a) GRAD (b) CLARK (c) HUAI models for case 4A; (d) an overlay of instantaneous flame contours for GRAD, CLARK and HUAI models for case 4A. The inner lines denote $\tilde{c} = 0.05$ whiles outer lines denote $\tilde{c} = 0.95$.

more conical with HUAI and CLARK models having a highly pronounced curved flame tip. This makes the estimation of the turbulent flame speeds more accurate and easier, since a linear portion of the flame can be obtained by neglecting smaller portions from the flame base and tip. Table 6.1 shows that the value of the resolved flame surface ($S_{res} = \int |\nabla \bar{c}|\, dV$) with HUAI and CLARK models increases by about 10-15%. This suggests that the flame front gets more wrinkled with the use of HUAI and CLARK models. Similar trends can be observed in Fig. 6.5 for case 12A.

Table 6.1: Values of resolved flame surface with GRAD, HUAI and CLARK models

Model	S_{res} [m^2]
GRAD	0.001598
HUAI	0.001762
CLARK	0.001803

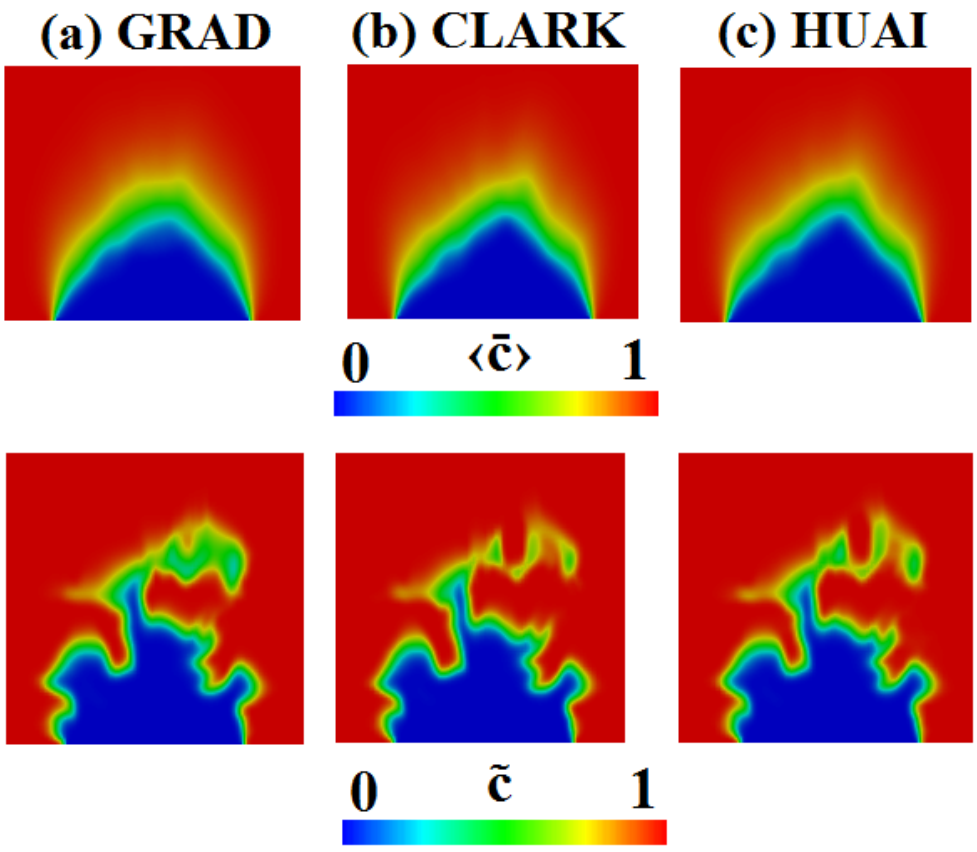

Figure 6.5: Comparison of time-averaged $\langle \bar{c} \rangle$ and instantaneous flame surface $\tilde{c}$ with (a) GRAD (b) CLARK (c) HUAI model for case 12A.

The influence of filter width on the time-averaged progress variable $\langle \bar{c} \rangle$, the instantaneous Favre filtered progress variable $\tilde{c}$, FSD Σ and $|\nabla \tilde{c}|$ for cases 4A and 4C with HUAI and CLARK models is shown in Fig. 6.6. It is worth noting that qualitatively similar results have been obtained for the other cases in Table 5.1 and hence, only case 4 is shown in Fig. 6.6 for the sake of conciseness. Comparing case A to case C, it can be seen that $|\nabla \tilde{c}|$, which is an indicator of the resolved flame surface, is smoother for the coarsest mesh and strongly wrinkled for the finest mesh. The instantaneous turbulent flame fronts are thinner but the time-averaged turbulent flame fronts do not change much when the mesh resolution is increased. This confirms that the combustion model gives satisfactory performance, in terms of grid independence, independent of the SGSF closure.

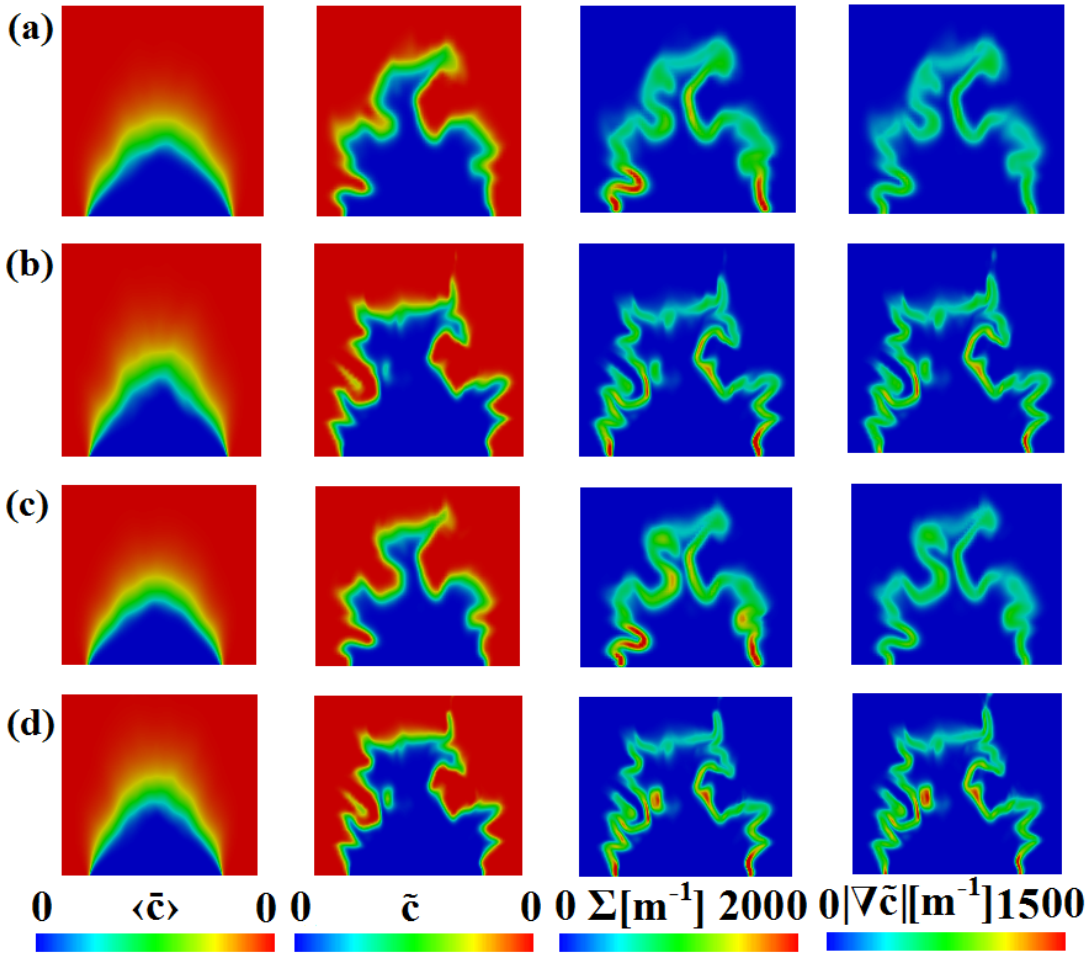

Figure 6.6: Influence of filter width on the time-averaged $\langle \bar{c} \rangle$, instantaneous flame surface $\tilde{c}$, FSD Σ and $|\nabla \tilde{c}|$ with HUAI model for (a) case 4A (b) 4C, and with CLARK model for (c) case 4A (d) 4C.

It has to be noted here that the implicit filtering approach has been used in this work where the ratio of filter width to grid spacing is kept constant. In addition, the nonlinear numerical discretization scheme used for reaction progress variable transport ensures a numerical thickness of the resolved flame front of approximately 5 grid cells and hence, the flux limiter can be viewed as an additional implicit filter. Explicit filtering of the reaction progress variable equation and the related consistency issues between flame and flow filter sizes are discussed in a recent paper by Mercier *et al.* [134].

The performance of the combustion model with GRAD, HUAI and CLARK models is evaluated by comparing the predicted turbulent flame speed for methane fuel at different pressure levels with the experimental data. The predicted turbulent flame speeds are plotted versus u'/s_L^0 in Fig. 6.7 for 0.1 MPa, 0.5 MPa and 1 MPa. The increasing trend of turbulent flame speeds with increasing values of u'/s_L^0 is captured well at all pressures. The comparison of the estimated flame speeds using thermo-chemical properties of methane at different pressure levels with CLARK and HUAI formulations with classical gradient closure for SGSF reveals that the change of the overall flame speed is within the error tolerance of the evaluation of the turbulent flame speed.

There are several possible reasons for the small influence of the SGSF model on the turbulent flame speed results in the present study. One could, for example, assume that contrary to Reynolds-averaged Navier Stokes (RANS) simulations, where the turbulent scalar flux is entirely modelled [35], the present LES partially resolves the important physical mechanisms responsible for the turbulent fluxes [135] and therefore, possibly also partially resolves the physical processes responsible for counter-gradient transport (CGT) [136]. However, the statistical behaviour of the nature of turbulent scalar flux (i.e. CGT versus GT) depends on the competition between transport due to turbulent velocity fluctuations and flame normal acceleration. Table 5.1 and Fig. 6.7 show that u'/s_L^0 values range from very small to rather large values. Therefore, the absence of a significant amount of CGT at the unresolved scale is unlikely. Another possible explanation is that the momentum transport is still done with an eddy viscosity model. Hence, the momentum flux modelling error will also result in a scalar advection error, which may preferentially be of a gradient type. Scalar transport in the general purpose CFD code OpenFOAM is done with a flux limiter scheme. The inherent numerical diffusion might also

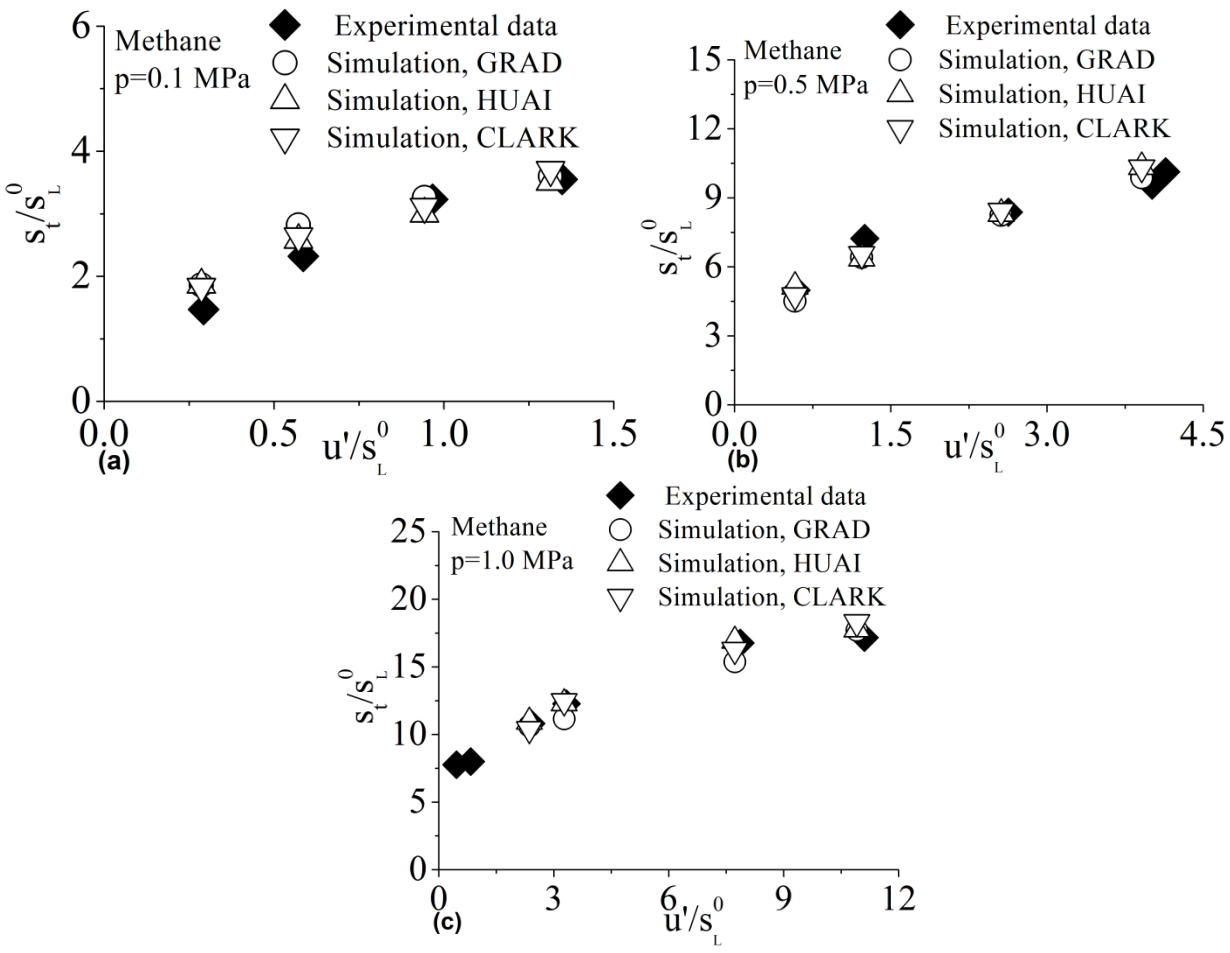

Figure 6.7: Comparison of turbulent flame speed at (a) 0.1 MPa, (b) 0.5 MPa and (c) 1.0 MPa using methane fuel

counter and possibly dominate over the CGT effects predicted by the SGSF closures. This will be examined in more detail in the next section. In this regard, it is also important to mention that no numerical problems, in terms of unrealizable values of the reaction progress variable c, were observed when using Clark's model (CLARK), despite the fact that this model was reported to provide an insufficient amount of SGS dissipation and hence, is unstable in nature [137].

Finally, a KPP analysis was done in [141] to determine the effect of the CGT type SGSF model on the turbulent flame speed. However, as pointed out by Hakberg and Gosman [138], in this kind of analysis the turbulent flame speed is determined by the properties at the leading edge of the flame brush, where counter-gradient diffusion is unlikely to prevail. This is consistent with recent DNS findings reported in Gao *et al.* [43,44] and Klein *et al.* [139]. Despite the fact that

some combustion models cannot be analysed directly using the traditional KPP technique [100,140], the arguments put forward in [141] suggest that CGT is not likely to affect the turbulent flame speed evaluated in the limit of $c \to 0$.

6.2.2 A-priori analysis

The interaction of SGSF and FSD closures in the original Keppeler model have been investigated further using a-priori DNS analysis in order to understand the combined effects of these terms [141]. This analysis was done by the coauthors [Prof. Klein and Prof. Chakraborty] of the work [141] and the key findings are presented here only for completeness. The interested reader is referred to [141] for more details. The DNS database, described in detail in Ref. [142], has been explicitly filtered using a Gaussian filter kernel for a range of filter widths from $\Delta \approx 0.4\,\delta_L^0$ where the flame is almost resolved, up to $\Delta \approx 2.8\,\delta_L^0$ where the flame becomes fully unresolved and Δ is comparable to the integral length scale. The initial values of normalized root mean square turbulent velocity fluctuation u'/s_L^0, the ratio of turbulent integral length scale to flame thickness l_0/δ_L^0, Damköhler number $Da = l_0 s_L^0/\delta_L^0 u'$, $Ka = (u'/s_L^0)^{1.5}(l_0/\delta_L^0)^{0.5}$ and turbulent Reynolds number $Re_t = \rho_u\, u' l_0/\mu_u$ are provided in Table 4 where $\delta_L^0 = (T_{ad} - T_u)/\max|\nabla\hat{T}|_L$ is the thermal flame thickness with $\hat{T}$ being the dimensional temperature. Table 6.2 indicates that the cases A, C and E (B, C and D) have same values of Da (Ka) and Ka (Da) is modified to bring about the changes in Re_t. Standard values are chosen for Prandtl number Pr and ratio of specific heats γ (i.e. $\mathrm{Pr} = 0.7$ and $\gamma = 1.4$). The flame Mach number $M = S_L/\sqrt{\gamma R T_0}$, heat release parameter $\tau = (T_{ad} - T_u)/T_u$ and Lewis number Le are taken to be 0.014, 4.5 and 1.0 respectively.

Table 6.2: List of initial simulation parameters and non-dimensional numbers

Case	A	B	C	D	E
u'/s_L^0	5.0	6.25	7.5	9.0	11.25
l_0/δ_{th}	1.67	1.44	2.5	4.31	3.75
Re_t	22.0	23.5	49.0	100	110
Da	0.33	0.23	0.33	0.48	0.33
Ka	8.65	13.0	13.0	13.0	19.5

Before proceeding with the analysis, another model for the turbulent transport term in the $\tilde{c}$ transport equation is presented below (see Eq. (6.1a)), which consists of a gradient contribution, i.e. the GRAD model and a term that is of counter-gradient type [42,52,124]:

$$\frac{\partial F_i^{sg}}{\partial x_i} = \frac{\partial(\overline{\rho u_i c} - \bar{\rho}\tilde{u}_i\tilde{c})}{\partial x_i} = \frac{\partial}{\partial x_i}\left(-\frac{\mu_{sgs}}{Sc_t}\frac{\partial \tilde{c}}{\partial x_i}\right) + \rho_u s_L \Xi(|\nabla \bar{c}| - |\nabla \tilde{c}|) \qquad (6.1a)$$

$$\frac{\partial}{\partial x_i}\left(\overline{\rho\alpha\frac{\partial c}{\partial x_i}}\right) + \bar{\dot{\omega}} - \frac{\partial(\overline{\rho u_i c} - \bar{\rho}\tilde{u}_i\tilde{c})}{\partial x_i} = \frac{\partial}{\partial x_i}\left(\overline{\rho\alpha\frac{\partial c}{\partial x_i}}\right) + \bar{\dot{\omega}} - \frac{\partial F_i^{sg}}{\partial x_i}$$

$$= \rho_u s_L \Xi|\nabla \bar{c}| + \frac{\partial}{\partial x_i}\left(\frac{\mu_{sgs}}{Sc_t}\frac{\partial \tilde{c}}{\partial x_i}\right) - \rho_u s_L \Xi(|\nabla \bar{c}| - |\nabla \tilde{c}|) = \rho_u s_L \Xi|\nabla \tilde{c}| + \frac{\partial}{\partial x_i}\left(\frac{\mu_{sgs}}{Sc_t}\frac{\partial \tilde{c}}{\partial x_i}\right) \qquad (6.1b)$$

The last contribution on right-hand side of Eq. (6.1a) constitutes an implicit CGT SGSF model, because the model appears implicitly in the equations if the resolved flame surface $|\nabla \bar{c}|$ in the FSD given by $\Sigma = \Xi|\nabla \bar{c}|$ is replaced with $|\nabla \tilde{c}|$. In other words, $\rho_u s_L \Xi|\nabla \tilde{c}|$ can be understood as a combination of the divergence of an implicit SGSF model of CGT type, and the filtered flame front displacement (FFFD) term = $\overline{\nabla \cdot (\rho\alpha\nabla c)} + \bar{\dot{\omega}}$ (see Eq. (6.1b)). Here, Eq. (6.1a) is denoted as the IMPL model if the wrinkling factor Ξ is set to the following expression as governed by Eq. (4.17):

$$\Xi = \left(2.2\Delta \,/\, \max\left(\delta_L Ka_\Delta^{-1/2}, 2\delta_L\right)\right)^{D-2} \qquad (6.1c)$$

From Eq. (4.3) one could assume that the expression for the FFFD should be proportional to $|\nabla \bar{c}|$. However, the model given by Eq. (4.17) is essentially proportional to $|\nabla \tilde{c}|$. The IMPL model arises from the fact that $|\nabla \tilde{c}|$ is used instead of $|\nabla \bar{c}|$. Note that, since a transport equation for $\tilde{c}$ is solved, the precise value of $\bar{c}$ is not available. This model is only introduced to explain (by means of a-priori analysis) the effects which might arise if one uses $|\nabla \tilde{c}|$ instead of $|\nabla \bar{c}|$ in the model expression for FFFD. Interested readers are referred to Ref. [143] for further discussion on this.

Expressing the FFFD with the help of Eq. (4.3) and using the FSD model given by Eq. (4.17) in combination with the gradient flux approximation GRAD results exactly in the expression given by Eq. (6.1b). Figure 6.8 shows the well-known Pearson correlation coefficients between the divergence of modelled SGSF term and exact turbulent scalar flux from DNS for the GRAD,

CLARK and the IMPL models. The calculation is done over the whole computational domain, but limited to the flame brush region, i.e. to the range $0.1 \leq \bar{c} \leq 0.9$. The HUAI model performs similar to the CLARK model, but with slightly smaller correlation than the CLARK model, and thus is not shown here. To reduce the amount of information, the correlation coefficients in Fig. 8b are averaged over all filter widths for each case and this averaged value is denoted as c^{Δ}, whereas $c^{u',\Delta}$ represents an averaging of c^{Δ} over cases A-E. It can be seen from Fig. 6.8 that the GRAD model is negatively correlated with the exact SGSF term for cases A-C, whereas a small positive correlation is observed for cases with very high turbulence intensities (e.g. cases D and E). This behaviour shows also that the extent of CGT increases with decreasing turbulence intensity. The CLARK model shows a considerably better correlation coefficient than the other alternatives. It was reported in [43,44] that the CLARK model exhibited the best a-priori performance among several SGSF closures available in the existing literature. The IMPL model seems to be particularly successful in representing the CGT transport as the correlation increases from case E to case A. Overall the implicit model demonstrates a positive correlation with the SGSF term.

This suggests that using an explicit CGT model, or a model able to represent CGT transport, is

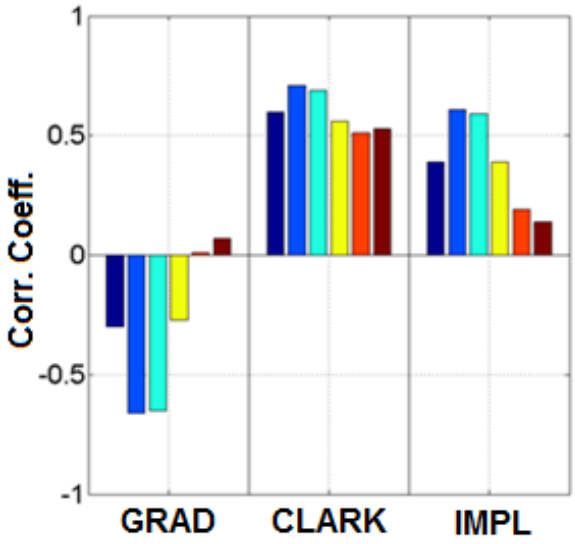

Figure 6.8 (a) Correlation coefficients between $\partial\left(F_i^{sg}\right)/\partial x_i$ and $\partial\left(F_i^{sg,model}\right)/\partial x_i$ for models GRAD, CLARK, IMPL: $c^{u',\Delta}$(■); $c^{\Delta}(u'/S_L = 5.0)$ (■); $c^{\Delta}(u'/S_L = 6.25)$ (■); $c^{\Delta}(u'/S_L = 7.5)$ ( ); $c^{\Delta}(u'/S_L = 9.0)$ (■) and $c^{\Delta}(u'/S_L = 11.25)$ (■)

No longer required for the FSD model given by Eq. (4.17). In fact, it can be argued that the CGT part of the SGSF flux would be taken into account twice by using such a model, in particular in situations when CGT is dominant. In order to make the analysis more complete the correlation between $-\nabla\cdot(\overline{\rho u_i c}-\bar{\rho}\widetilde{u_i}\tilde{c})+\overline{\nabla\cdot(\rho D\nabla c)+\dot{\omega}}$ and the corresponding model expressions is finally considered. The FFFD, $\overline{\nabla\cdot(\rho D\nabla c)+\dot{\omega}}$ is modelled using Eqs. (4.3) and (4.17) (denoted KP, Keppeler's model), and the SGSF part is modelled using either the GRAD or the CLARK model. The resulting models are referred to as the GRADKP and CLARKKP models, respectively. The correlation coefficients averaged over all cases and all filter widths, i.e. $c^{u',\Delta}$, are 0.46 and 0.45 for GRADKP and CLARKKP models, respectively, and thus the a-priori analysis also corroborates the observation that both model combinations perform similarly. It is interesting to observe that the GRAD model even yields a slightly better correlation coefficient than the CLARK model when combined with Eq. (4.17). However, this observation is only valid for this particular FSD model and other FSD closures may demonstrate a different behaviour. A more extensive analysis of this aspect is left for future work.

6.3 Investigation of pressure and Le number effects

In this section, the performance of different FSD models is investigated for pressure and *Le* number effects in the predictions of premixed flames.

6.3.1 Investigation of the original Keppeler model with Le number correction

In this section, the performance of the original Keppeler model is investigated in its substantiated form−which we call the tuned Keppeler model− by the explicit inclusion of a term accounting for fuel effect. As described in the previous sections, the Keppeler model, in its original form, showed excellent performance for methane flames (*Le* = 1) over a wide range of turbulence and pressures between 1 and 20 bar, at situations which are typical for industrial gas turbines and spark-ignition engines [53]. The performance of the model was also investigated with propane fuel (*Le* = 1.62) and it was observed that the predicted turbulent flame speed values overestimate the experimental findings, especially at high turbulence values [53]. In practice, fuels having

higher *Le* numbers than methane have applications in spark ignition engines and gas turbines, thus investigation of the fuel effects on the flame characteristics at high-pressures is of considerable importance. A non-unity *Le* number is expected to influence the flame characteristics by modifying the local processes of species diffusion towards the flame front and of heat diffusion away from the flame front. Several experimental investigations have shown a significant role of *Le* number in highly turbulent premixed flames [144], especially for high-pressure conditions [49]. In the RANS study by Muppala *et al.* [105], an explicit Lewis number dependency (1/*Le*) in an algebraic FSD reaction rate closure was found successful in matching the burning rate of a variety of fuels ($Le \geq 1$) with the experimental data for pressures up to 10 bar. The model was further extended for LES approach and checked for its applicability for a Bunsen-like burner, a sudden expansion dump combustor and a typical swirl–stabilised gas turbine combustor [17]. It showed results in good agreement with the experiments. In recent work [145] from the same group, the RANS model is used to simulate lean premixed turbulent methane/hydrogen/air flames ($Le \leq 1$) with an effective *Le* number approach. The reaction rate closure approach with an explicit *Le* number dependency term was found to give a very good agreement for all the flames with hydrogen content up to 20% and a satisfactory agreement for 30% and 40% hydrogen. Chakraborty and Cant [146] also reported that the approximation $\overline{(\rho S_d)}_S \approx \rho_u s_L$ is not valid for non-unity *Le* number fuels and suggested the following scaling:

$$\overline{(\rho S_d)}_S \approx \rho_u s_L / Le \tag{6.2}$$

In a recent study [143], based on a-priori analysis of DNS data for a range of different *Le* numbers, the performance of several subgrid scalar flux models and algebraic FSD models in the context of turbulent premixed combustion is investigated on an individual basis and in terms of their combined interactions. It is reported that the *Le* number correction given by Eq. (6.2) significantly improves the magnitude of the surface-weighted filtered values of density-weighted displacement speed.

Following the above discussion, the correction given by Eq. (6.2) is included in the final FSD expression of the Keppeler model. The performance of the tuned and original versions of the model is investigated and compared to the experimental data. The comparison is done by evaluating the predicted turbulent flame speeds for propane fuel at 1 and 5 bars. The flame speeds are calculated according to the method explained in section 5.1 and illustrated in Figs.

5.2b and 6.2. The normalised flame speeds for propane fuel s_t/s_L^0 are plotted versus u'/s_L^0 in Figs. 6.9a and 6.9b for 1 and 5 bar, respectively. The Keppeler model without *Le* number correction shows deviations with increasing turbulence level and the turbulent flame speed is increasingly over-predicted. However, the model scales well with the pressure. With the tuned Keppeler model, the predicted turbulent flame speed matches the experimental data very well at 1 and 5 bar. Thus Eq. (6.2) is proven to be a suitable way of incorporating explicit fuel effects in the Keppeler model as well. The explicit *Le* number term is also introduced in the Fureby model and the results are presented and discussed in section 6.3.4.

6.3.2 Analytical investigation of the FSD models with respect to pressure dependency

In the previous section, Eq. (6.2) is shown to be an effective way of incorporating explicit fuel effects in the algebraic FSD modelling. In this section, the performance of the Angelberger, Fureby and Zimont models is analytically investigated to check their ability to scale correctly with pressure. The wrinkling factors, using Eqs. (4.27), (4.29d), (4.30) and (6.1c), are analytically calculated for a system that is representative of the current LES setup. The calculations are done with typical values of s_L^0, δ_L and α for methane fuel using $\Delta = 0.4$ mm

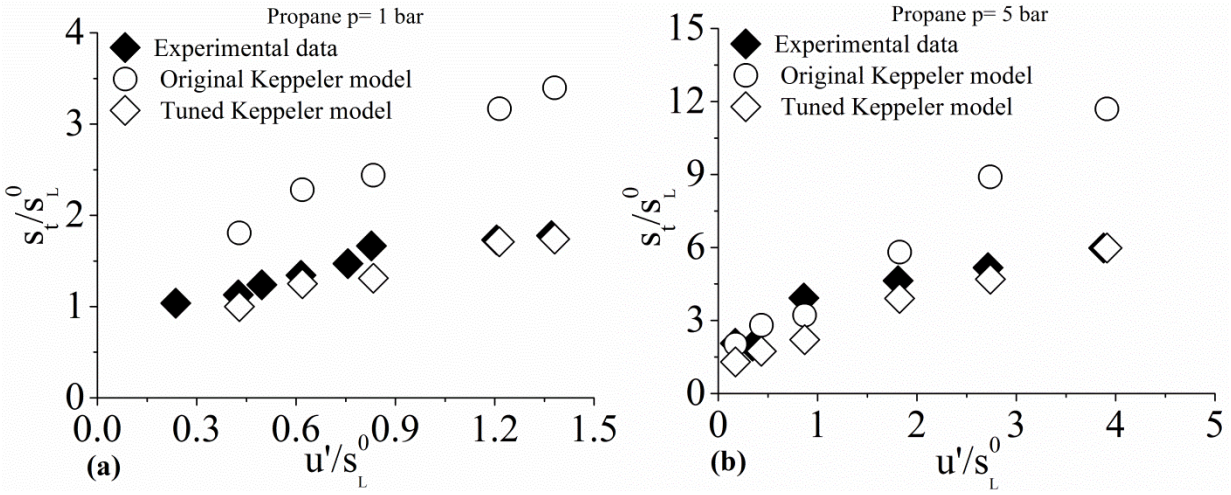

Figure 6.9: Comparison of turbulent flame speed at (a) 1 bar and (b) 5 bar using tuned Keppeler model for propane fuel

(representing a single mesh block) at 1, 5 and 10 bar. The subgrid turbulent velocity fluctuation value is calculated with $u'_\Delta = \sqrt{2\,k_{sgs}/3}$, where k_{sgs} is approximated as 10% of the total turbulent kinetic energy as reported in [131], a good LES should resolve about 80-90% of the total turbulent kinetic energy. The procedure used and a comparison of the analytical values of wrinkling factor with the Keppeler model and the original and tuned Fureby models are shown in Table 6.3. Figs. 6.10a, 6.10b and 6.10c show the values of wrinkling factors obtained with the original versions of the models for 1, 5 and 10 bar, respectively. The calculated values of Ξ are compared with the ones obtained with the Keppeler model (Eq. (6.1c)), as it showed an excellent quantitative agreement with the experimental data and captured the right pressure scaling [53]. The comparison of the calculated values of Ξ at 1 bar shows deviations with increasing turbulence level and Ξ values are increasingly under-predicted (Fig. 6.10a). This suggests the tuning of model constants to reach the right quantitative agreement and the increasing trend of turbulent flame speed values with increasing values of turbulence as observed in the experimental findings. The results in Figs. 6.10b and 6.10c show that all the models failed to capture the right pressure scaling. This highlights the requirement for tuning the models to achieve the right pressure dependency and claim generality of the conditions, where the models can be used successfully.

6.3.3 Comparison of pressure exponents of s_t

The analysis presented in the previous section implies that the turbulent flame speed s_t would decrease with increasing pressure, unlike results from theoretical [18] and experimental [17] studies, where pressure independence of s_t for methane is reported. The experimental data used for the validation of the present work also reports weak pressure dependence $s_t \propto p^{0.07}$ for methane [82]. In this section, the pressure dependence of the reaction rate closure expressions of the Angelberger, Fureby and Zimont models, interpreted in s_t, is calculated using a simple analysis and compared to the experimental findings for methane and propane. The method is used by Muppala *et al.* [105] to develop a correct pressure dependence of the reaction rate closure in their combustion model. The pressure dependency of s_t for the combustion models

Table 6.3: Comparison of analytical values of wrinkling factor at 1, 5 and 10 bar using the Keppeler model, the original and tuned Fureby models for methane fuel

						Keppeler Model				Original Fureby Model				Tuned Fureby Model			
Case	s_L^0	δ_L	Δ	u'	u'_Δ	Ka	ε_i	D	Ξ	Γ	ε_i	D	Ξ	Γ	ε_i	D	Ξ
	(m/s)	(m)	(m)	(m/s)	(m/s)	$(-)$	(m)	$(-)$	$(-)$	$(-)$	(m)	$(-)$	$(-)$	$(-)$	(m)	$(-)$	$(-)$
2	0.35	4.51E-05	4.00E-04	0.2	0.06325	2.58E-02	0.000281	2.308277	1.421764	0.432506	0.005118	2.095914	1.007244	5.478403	0.000404	2.308277	1.236308
4	0.35	4.51E-05	4.00E-04	0.46	0.14546	0.090012	0.00015	2.500016	2.418433	0.673763	0.001428	2.138078	1.034676	8.534333	0.000113	2.500016	2.132419
6	0.1565	2.02E-05	4.00E-04	0.19	0.06008	0.053446	8.73E-05	2.426991	2.68155	1.109477	0.000939	2.133224	1.048408	14.05338	7.41E-05	2.426991	2.208496
8	0.1565	2.02E-05	4.00E-04	0.61	0.1929	0.307454	4.04E-05	2.607399	6.499355	1.779052	0.000182	2.215626	1.284439	22.53466	2.02E-05	2.607399	6.320029
9	0.1107	1.43E-05	4.00E-04	0.26	0.08222	0.12091	4.1E-05	2.534138	5.140988	1.863378	0.000289	2.177855	1.167092	23.60279	2.28E-05	2.534138	4.7558
12	0.1107	1.43E-05	4.00E-04	1.2	0.37947	1.198879	2.85E-05	2.650392	9.298144	3.01973	3.86E-05	2.282248	1.98512	38.24991	1.43E-05	2.650392	8.940832

$$Ka_\Delta = \left(\frac{u'_\Delta}{s_L^0}\right)^{3/2}\left(\frac{\delta_L}{\Delta}\right)^{1/2}$$

$$\varepsilon_i = \delta_L * max\left(Ka_\Delta^{-1/2}, 2\right)$$

$$D = \frac{8/3Ka_\Delta + 2C_D}{Ka_\Delta + C_D}$$

$$\Xi = C_{Le}\left(\frac{2.2\Delta}{\varepsilon_i}\right)^{D-2}$$

$$\Gamma = A * \left[\frac{-B}{\left(u'_\Delta/s_L^0\right)^{0.3}}\right] * \left(\frac{\Delta}{\delta_L}\right)^{2/3}$$

$$A = 0.75, B = 1.2$$

$$\varepsilon_i = \frac{s_L^0 * \Delta}{u'_\Delta * \Gamma}$$

$$D = \frac{2.05 * s_L^0}{u'_\Delta + s_L^0} + \frac{2.35 * u'_\Delta}{u'_\Delta + s_L^0}$$

$$\Xi = \left(1 + \frac{\Delta}{\varepsilon_i}\right)^{D-2}$$

$$\Gamma = A * \left[\frac{-B}{\left(u'_\Delta/s_L^0\right)^{0.3}}\right] * \left(\frac{\Delta}{\delta_L}\right)^{2/3}$$

$$A = 9.5, B = 1.2$$

$$\varepsilon_i = \max\left(\frac{s_L^0 \Delta}{u'_\Delta \Gamma}, \delta_L\right)$$

$$D = \frac{8/3Ka_\Delta + 2C_D}{Ka_\Delta + C_D}$$

$$\Xi = C_{Le}\left(1 + \frac{\Delta}{\varepsilon_i}\right)^{D-2}$$

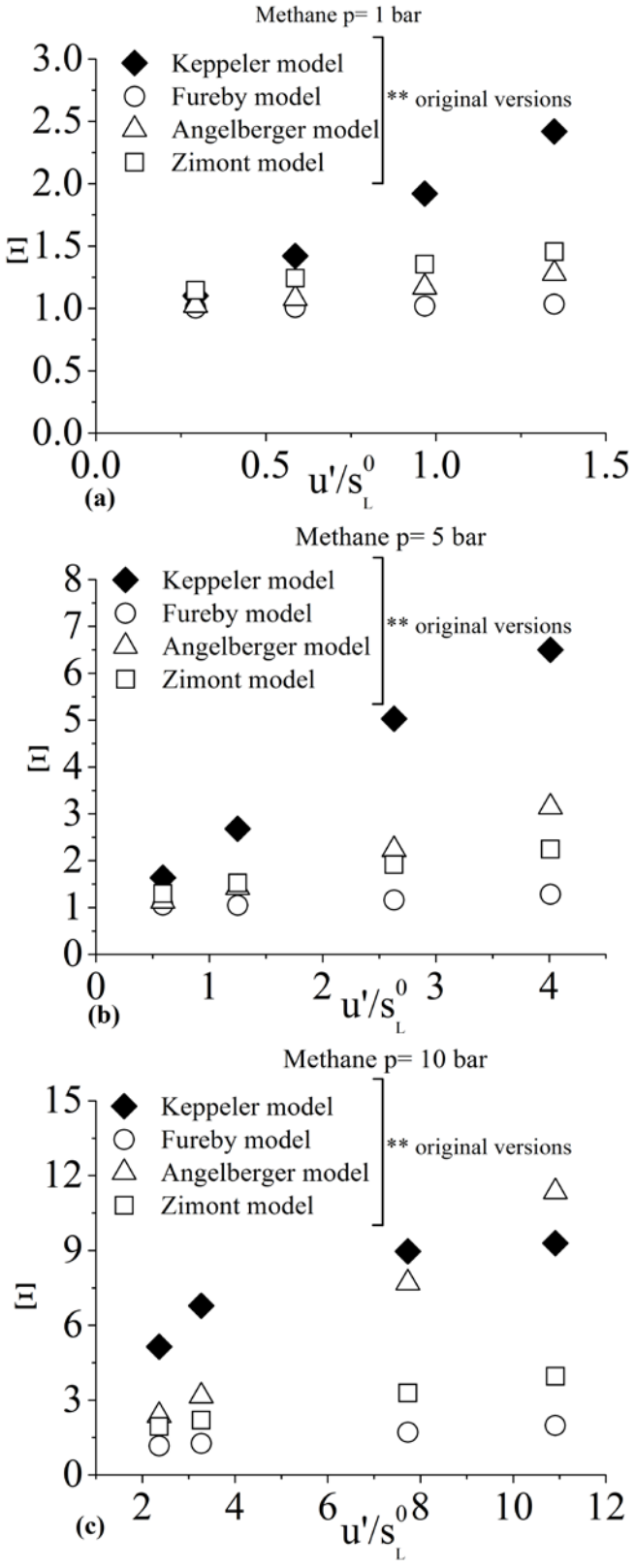

Figure 6.10: Analytical comparison of wrinkling factor at (a) 1 bar, (b) 5 bar and (c) 10 bar using the original versions of the models for methane fuel

Table 6.4: Comparison of pressure exponents of the FSD models.

Original Angelberger model			Tuned Angelberger model		
$\sim p^x, x = \cdots$	CH_4	C_3H_8	$\sim p^x, x = \cdots$	CH_4	C_3H_8
s_L	-0.50	-0.26	s_L	-0.50	-0.26
$\Xi(= s_t/s_L)$	0.83	0.75	$\Xi(p/p_0)^n(= s_t/s_L)$ $n = -0.25$	0.58	0.50
$s_L\Xi(= s_t)$ (Cal.)	0.33	0.49	$s_L\Xi(p/p_0)^n(= s_t)$ (Cal.)	0.08	0.24
s_t (Experimental)	0.07	0.24	s_t (Experimental)	0.07	0.24
Original Zimont model			Tuned Zimont model		
$\sim p^x, x = \cdots$	CH_4	C_3H_8	$\sim p^x, x = \cdots$	CH_4	C_3H_8
s_L	-0.50	-0.26	s_L	-0.50	-0.26
$\Xi(= s_t/s_L)$	0.50	0.38	$\Xi(p/p_0)^n(= s_t/s_L)$ $n = 0.15$	0.65	0.53
$s_L\Xi(= s_t)$ (Cal.)	0	0.12	$s_L\Xi(p/p_0)^n(= s_t)$ (Cal.)	0.08	0.27
s_t (Experimental)	0.07	0.24	s_t (Experimental)	0.07	0.24
Original Fureby model			Tuned Fureby model		
$\sim p^x, x = \cdots$	CH_4	C_3H_8	$\sim p^x, x = \cdots$	CH_4	C_3H_8
s_L	-0.50	-0.26	s_L	-0.50	-0.26
$\Xi(= s_t/s_L)$ with $D_{max} = 2.35$	0.29	0.26	$\Xi(= s_t/s_L)$ with $D_{max} = 8/3$	0.55	0.50
$s_L\Xi(= s_t)$ (Cal.)	-0.21	0	$s_L\Xi(= s_t)$ (Cal.)	0.05	0.24
s_t (Experimental)	0.07	0.24	s_t (Experimental)	0.07	0.24

being in focus of the current work is calculated and the key findings are summarised in Table 6.4. The pressure dependence of the wrinkling factor expressions (Eqs. (4.27), (4.29d) and (4.30)) are calculated using the typical pressure scalings of s_L^0, δ_L and α for methane and propane fuels. It can be seen that none of the models possesses the correct pressure dependency of s_t compared to the experimentally observed $s_t \propto p^{0.07}$(methane) and $s_t \propto p^{0.24}$ (propane) [82]. This is in agreement with the analytical results shown in Fig. 6.10, where a large gap is observed between the calculated and reference values and the difference becomes larger with

pressure rise. Thus, both theoretical and analytical investigations argue an additional pressure influence to be included in the models. This is achieved by introducing an explicit pressure term $(p/p_0)^n$ in the Angelberger and Zimont models where $p_0 = 1$ bar, p is the operating pressure and exponent n is determined from the aforementioned analysis to get the right dependency of s_t, while in the Fureby model a better agreement is achieved using a modified estimation of D and ε_i. The tuning of the Fureby model will be explained in detail in the next section. The tuned versions of the models shows the corrected pressure dependence of s_t, which are now quite close to the experimental value The wrinkling factors obtained with the Eqs. (4.27), (4.29d) and (4.30) are recalculated incorporating the suitable tuning of model constants and the corrections for pressure dependency, and are plotted in Figs. 6.11a, 6.11b and 6.11c for 1, 5 and 10 bar, respectively. The new values of Ξ show the correct scaling with pressure and exhibit fairly good agreement with the ones obtained using the Keppeler model. The changes made to the model, to get their tuned versions, are summarised in Table 4.1.

6.3.4 Investigation of the Fureby model with the pressure and *Le* number corrections

In this section, the observations made in sections 6.3.2 and 6.3.3 are verified by randomly choosing the Fureby model and doing LES simulations with its original and tuned versions. Various studies [51,52,148-150] have reported that the Fureby model gives a satisfactory performance and seems to be a promising representative of an algebraic FSD closure method. But it is worth noting that most of these studies are done for high Karlovitz number (*Ka*) cases and are mainly limited to atmospheric methane flames. This motivates an investigation assessing the performance of the Fureby model in terms of turbulent flame propagation for situations corresponding to wrinkled flamelets and thin reaction zone regimes (having low *Ka* number) with a variety of fuels under high-pressures. The analytical calculations, as described in previous sections, have shown that the turbulent flame propagation predicted by the original version of the model would decrease with pressure, unlike theoretical and experimental findings for the validation data, which corresponds to low *Ka* number combustion regimes used in the present study. In the work of Chakraborty and Klein [51], a novel power law based FSD model was proposed, its performance was investigated in terms of the predicted FSD and compared with the

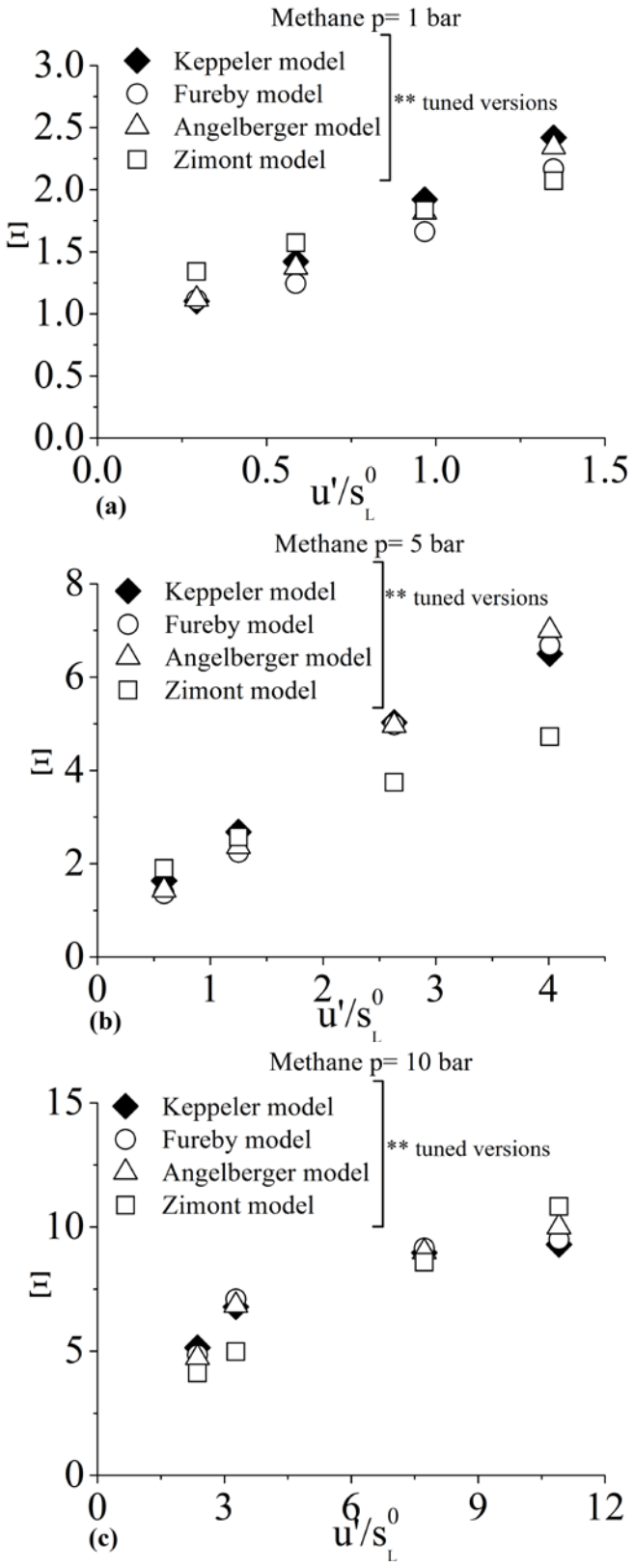

Figure 6.11: Analytical comparison of wrinkling factor at (a) 1 bar, (b) 5 bar and (c) 10 bar using the tuned versions of the models for methane fuel

corresponding values obtained from the DNS data alongside thirteen other existing algebraic FSD models, including the Fureby model. It is reported that for a high *Ka* number case, the Fureby model gives a satisfactory performance but for a low *Ka* number case the model greatly under-predicts the FSD values as compared to the DNS data [51, pp. 8-11]. The authors explained that the disagreement might be due to inaccurate estimation of efficiency function Γ, fractal dimension D and inner cut-off scale ε_i values at these conditions. It is also concluded that the model performance would be enhanced using an accurate and efficient parameterization of Γ, D and ε_i. In the original paper presenting the Fureby model [104], the author himself reported that Eq. (13c) was the only available empirical expression for D at that time. Moreover, a parameterization constant "A" is used to calculate ε_i. It is reported that the adopted parameterization is probably not optimal and is likely to be improved and optimized when the performance of the model is evaluated with suitable DNS and experimental data. It is also worth noting that unity is omitted in the Ξ expression. Thus, the resolved contribution to overall wrinkling is neglected and in the presence of zero/weak turbulence the wrinkling factor approaches to zero. This assumption works fine for high turbulence cases, i.e. for $\Xi \gg 1, \Xi = (1 + \varepsilon_o/\varepsilon_i)^{D-2} \cong (\varepsilon_o/\varepsilon_i)^{D-2}$. Hence, the original Fureby model may be intended for high Reynolds number cases only. Ma *et al.* [52] compared the performance of various algebraic FSD models alongside the Fureby model by performing LES of the ORACLES burner and Volvo Rig. It is reported that the Fureby model provides predictions that follows very closely $\Sigma \rightarrow |\nabla \tilde{c}|$ (Ξ =1). Similar findings have been reported in [148-150]. The analytical study presented in section 6.3 also shows that at ambient pressure, the Fureby model predicts Ξ close to one for low *Ka* number cases. In the current study, the model also under-predicts Ξ values even for high *Ka* number cases, but most other researchers have used the un-stretched laminar flame speed s_L^0 instead of stretched laminar flame speed s_L, increasing turbulent flame speed [148] and making the overall performance of the model satisfactory. The analysis, as shown in section 6.3.3, of the Fureby model with Eq. (4.29c) where D reaches to a constant upper value of 2.35, predicts a very low overall pressure influence on s_t for methane and propane fuels, which contradicts the experimental findings. But if D reaches to a constant upper value of 8/3 as used in Keppeler model, the KPP analysis predicts the correct pressure scaling of s_t. Thus, D has to reach a constant upper value of about 8/3 in the limit of high Reynolds number to predict the correct scaling of the model with pressure. The parameterization constant "A" in Eq. (4.28) is also tuned

from 0.75 to 9.5 to get an accurate estimation of ε_i and a good agreement of numerical predictions with the experimental data. The inner cut-off scale can get smaller than the laminar flame thickness in the original Fureby model, which is contrary to the findings of Driscoll [151] that the smallest wrinkling scale is always larger than $C\delta_L$,where C is a constant of the order of unity. It is also reported in the experimental work of Kobayashi *et al.* [111] that ε_i/δ_L reaches to a constant value, at least for high-pressure turbulent flames. Therefore, ε_i is limited to a value proportional to δ_L. The changes made to the Fureby model are summarized in Table 4.1. The LES simulations are done with the original and tuned versions of the Fureby model for methane and propane fuels and the results are compared with the experimental data and the Keppeler model. The performance of the tuned Fureby model is investigated with two different expressions of D, i.e. using Eq. (4.10) and Eq. (4.29c) but changing $D_{\max}$ from 2.35 to 2.667.

$$D = \frac{2.05 s_L}{u'_\Delta + s_L} + \frac{2.667 u'_\Delta}{u'_\Delta + s_L} \tag{6.3}$$

The normalized turbulent flame speed values for cases 2, 4, 9 and 12 are shown and compared with the experimental data in Table 6.5. It can be seen that the tuned Fureby model with Eq. (6.3) for D greatly under-predicts s_t, while the model with Eq. (4.10) for D gives turbulent flame speed values and pressure scaling in good agreement with the experimental data. Thus Eq. (4.10) which also gives good results in the Keppeler model, is used in the tuned Fureby model in the rest of the calculations. The effect of filter width on the time-averaged progress variable $\langle\bar{c}\rangle$, the instantaneous Favre filtered progress variable $\tilde{c}$, FSD Σ and $|\nabla\tilde{c}|$ for case 4 and case 12 using mesh A and C (henceforth denoted as 4A, 4C,12A and 12C) are shown in Fig. 6.12 for the tuned

Table 6.5: The normalised turbulent flame speed values obtained with the tuned Fureby model using Eqs. (6.5) and (4.10)

Pressure [bar]	Case	Experimental	Tuned Fureby model with Eq. (6.3) used for D	Tuned Fureby model with Eq. (4.10) used for D
		s_t/s_L^0	s_t/s_L^0	s_t/s_L^0
1	2	2.32	1.99	2.74
	4	3.55	2.74	4.02
10	9	10.83	3.32	9.71
	12	17.13	12.22	17.59

Fureby model. For the sake of conciseness, the other cases are not presented here because qualitatively similar results have been observed for other cases in Table 5.1. Figures 6.12a and 6.12c show the results with mesh A for 1 and 10 bar respectively while the results with mesh C are shown in Figs. 6.12b and 6.12d for 1 and 10 bar. Comparing the results for case A to case C, it can be observed that $|\nabla\tilde{c}|$ contours (an indicator of the resolved flame surface) are strongly wrinkled for the finest mesh and smoother for the coarsest mesh. The instantaneous turbulent flame fronts get thinner but the time-averaged turbulent flame fronts are not affected much when

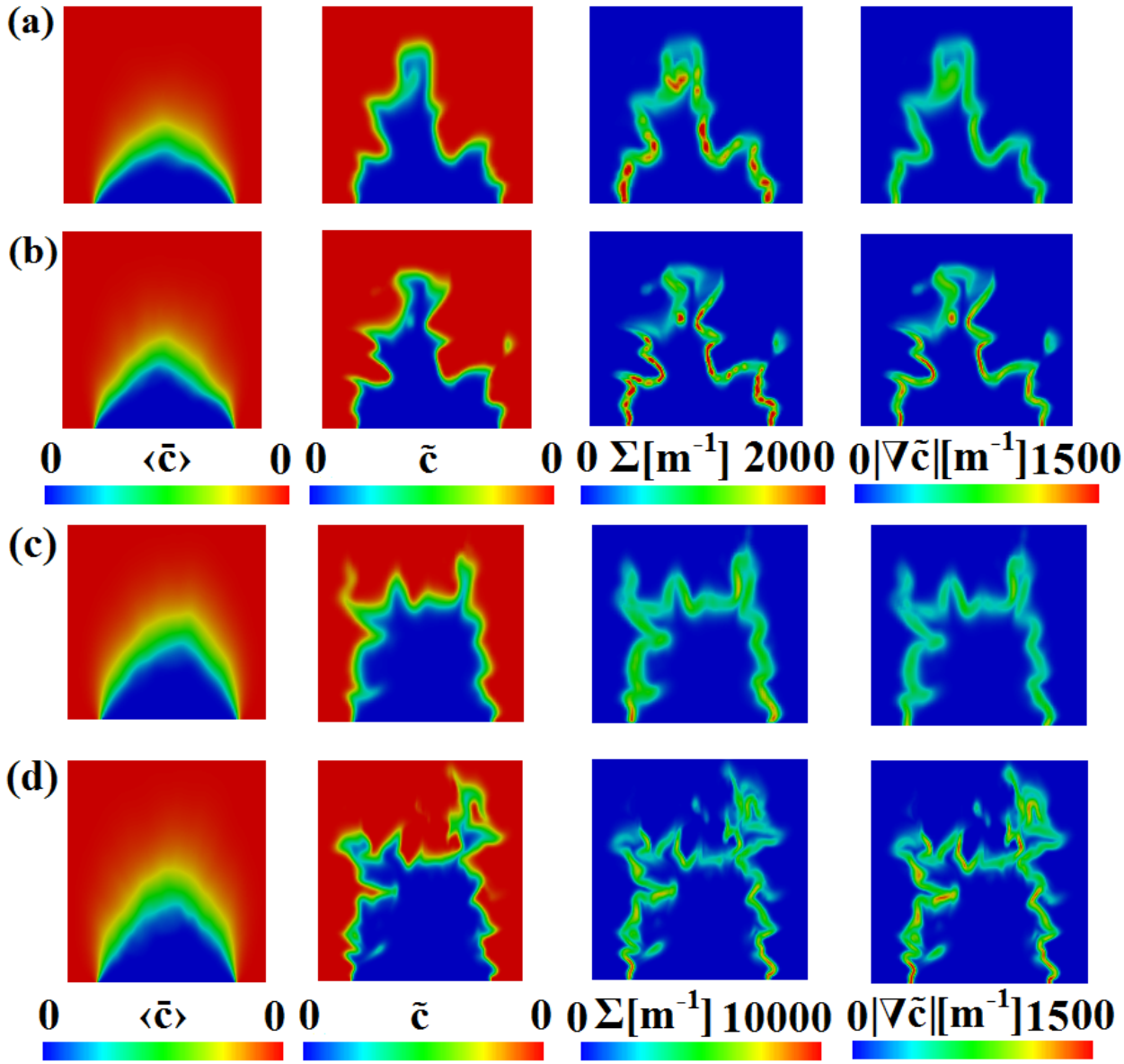

Figure 6.12: Influence of filter width on the time-averaged $\langle\bar{c}\rangle$, instantaneous flame surface $\tilde{c}$, FSD Σ and $|\nabla\tilde{c}|$ with tuned Fureby model for (a) case 4A, (b) 4C,(c) case 12A (d)12C.

the mesh resolution is increased. This shows that the tuned Fureby model gives satisfactory performance in terms of grid independence. For methane, Figs. 6.13a, 6.13b and 6.13c show the normalized flame speeds s_t/s_L^0 plotted versus u'/s_L^0 for 1, 5 and 10 bar respectively. For the original version of the Fureby model, a large gap can be observed between experimental and the predicted values, with the difference growing larger with pressure increment. The tuned version of the model gives very good quantitative agreement with the experimental data and captures the correct scaling with pressure. Figs. 6.14a and 6.14b show similar plots for propane fuel using the tuned version of the model with and without the *Le* number correction given by Eq. (6.2). The tuned Fureby model with the *Le* number correction, shows excellent agreement with experimental data over a wide range of turbulence and pressures between 1 and 5 bar.

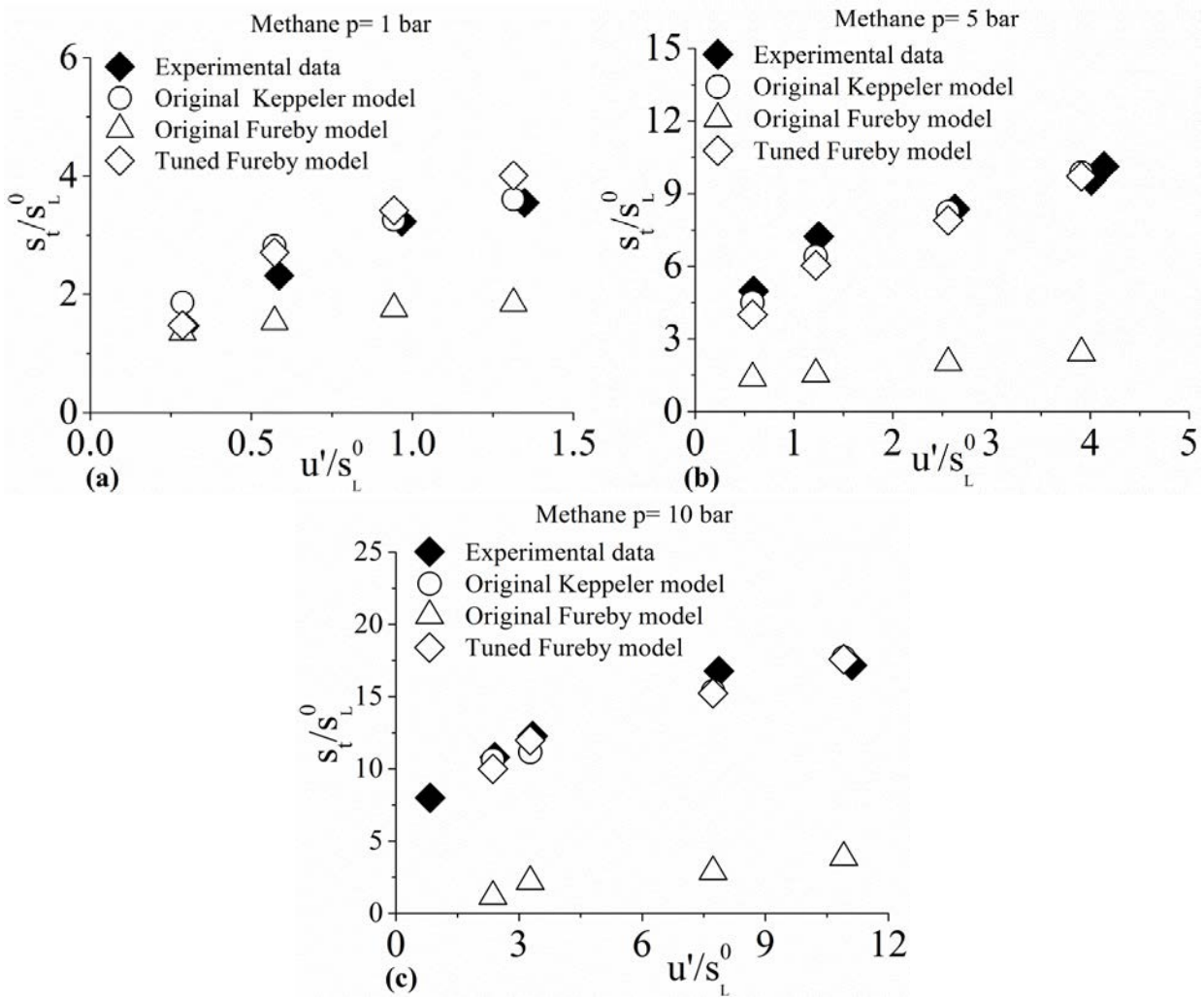

Figure 6.13: Comparison of turbulent flame speed at (a) 1 bar, (b) 5 bar and (c) 10 bar using the tuned and original Fureby models for methane fuel

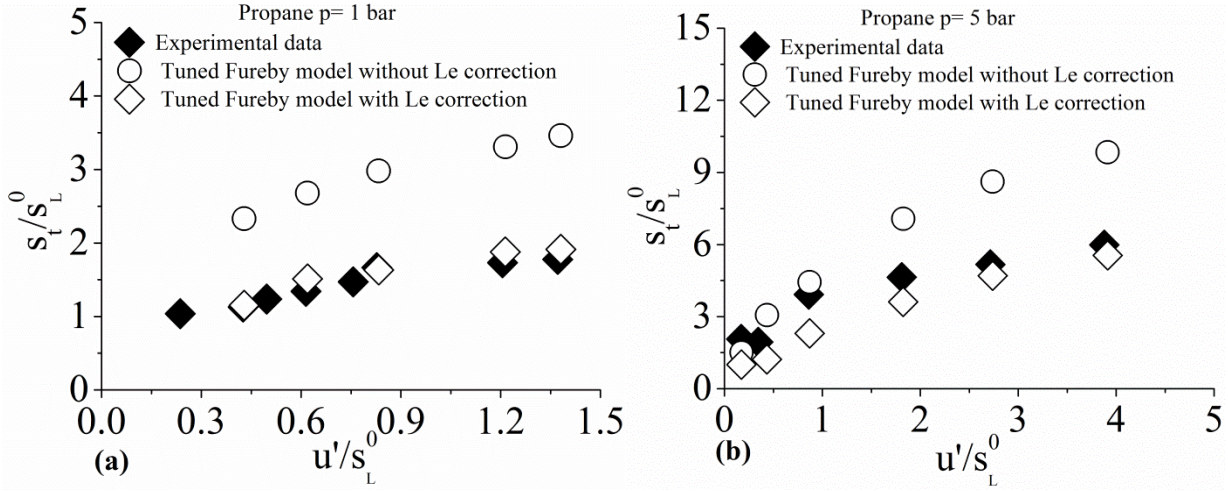

Figure 6.14: Comparison of turbulent flame speed at (a) 1 bar and (b) 5 bar using the tuned Fureby model with and without Le number correction for propane fuel

6.4 Investigation of RANS version of Keppeler model

In this section, the performance of the RANS Keppeler model is investigated using methane and propane as fuel and compared with the LES Keppeler model. The development of RANS Keppeler model is presented in section 4.5. Three systematically refined computational grids are used to evaluate the performance of the model in terms of predicted turbulent flame speed and the predicted flame surface. In Fig. 6.15, the mean Reynolds-averaged progress variable contours $\langle \bar{c} \rangle$ obtained with the RANS Keppeler model (Eq. (4.35)) are shown and compared with the corresponding predicted results from the LES Keppeler model (Eq. (4.18)) for case 7 using mesh A. For the sake of conciseness, the comparison of the results for other cases is not shown here because qualitatively similar results have been obtained for other cases. A comparison of the flame fronts in Fig. 6.15 shows that the Reynolds-averaged flames predicted by the RANS Keppeler model are more conical in shape with a highly pronounced curved flame tip as compared to the LES version of the model. The normalized turbulent flame speeds predicted by the RANS and LES Keppeler model are 10.21 and 10.37, respectively. It shows that the RANS Keppeler model gives a satisfactory performance, however, it predicts slightly less wrinkling of the flame for case 7 as compared to the LES Keppeler model.

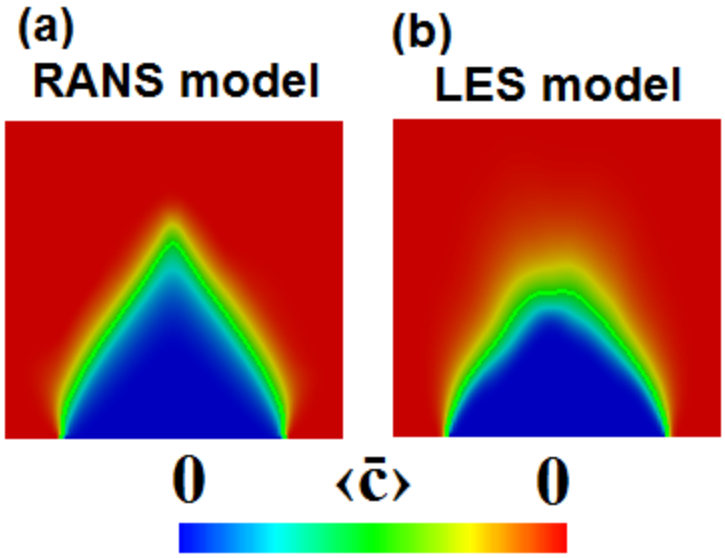

Figure 6.15: Comparison of time-averaged $\langle \bar{c} \rangle$ progress variable contours with original: (a) RANS Keppeler (b) LES Keppeler models. The inner lines denote $\bar{c} = 0.5$.

The performance of the simplified RANS Keppeler model (Eq. (4.37)) is compared with the original RANS Keppeler model (Eq. (4.35)) using case 7 with mesh A and the results are shown in Fig. 6.16. Similar Reynolds-averaged flame contours are predicted by the simplified and

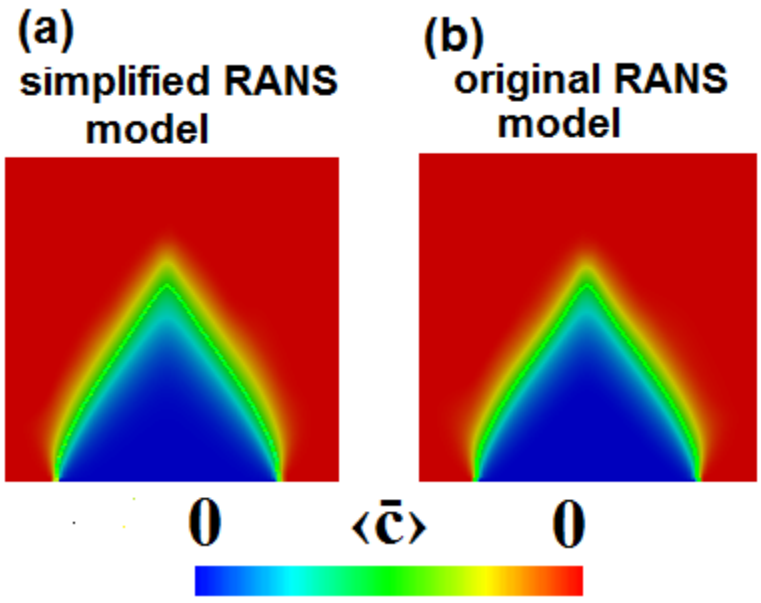

Figure 6.16: Comparison of time-averaged $\langle \bar{c} \rangle$ progress variable contours with: (a) simplified (b) original RANS Keppeler models. The inner lines denote $\bar{c} = 0.5$.

original RANS Keppeler models. However, the flame obtained with the simplified RANS Keppeler model is slightly longer and hence, the predicted turbulent flame speed is lower as compared to the original RANS Keppeler mode. The normalized turbulent flame speeds predicted by the simplified and original RANS models for case 7 are 9.98 and 10.21, respectively. These results support the results obtained and discussed in section 6.1. Since, the simplified and original RANS Keppeler models yield similar results, the former model is used in the rest of the evaluations made with the RANS Keppeler model.

Figure 6.17 shows the influence of grid resolution on the mean progress variable contours $\langle \bar{c} \rangle$ for case 7 with the simplified RANS Keppeler model at three systematically refined computational grids. The Reynolds-averaged flame contours do not change much as the grid resolution is increased, which is a sign of grid convergence for the RANS model. This shows that the RANS version of the Keppeler model gives satisfactory performance in terms of grid independence of predicted flame contours and turbulent flame speeds. Qualitatively similar results were obtained for other cases in Table 5.1.

The performance of the RANS Keppeler model is also compared with the experimental data. The comparison is made by evaluating the predicted turbulent flame speeds for methane fuel at 1, 5, 10 bar and for propane fuel at 1 and 5 bar. The *Le* number correction, as shown in Eq. (6.2), is used to include the fuel effects in the evaluations. Figure 6.18 shows the normalized flame speeds s_t/s_L^0 plotted versus u'/s_L^0 for methane fuel while Fig. 6.19 shows a similar plot for

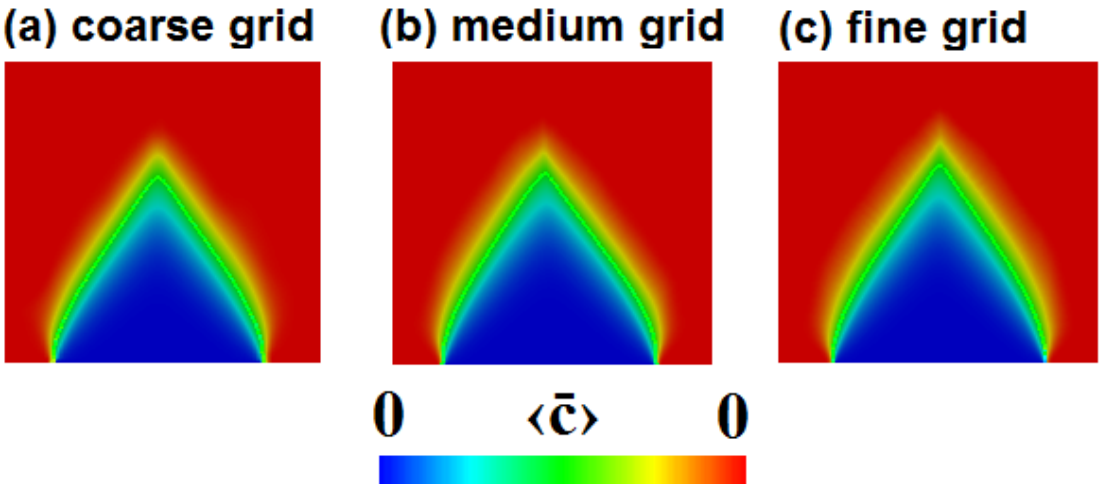

Figure 6.17: Comparison of time-averaged $\langle \bar{c} \rangle$ progress variable contours with: (a) coarse (b) medium fine grids using simplified Keppeler model. The inner lines denote $\bar{c} = 0.5$.

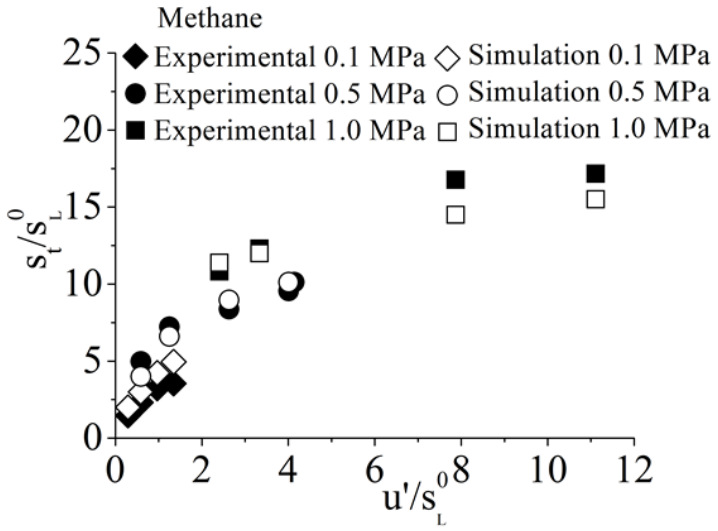

Figure 6.18: Comparison of turbulent flame speed at 1, 5 and 10 bar using the simplified RANS Keppeler model for methane fuel

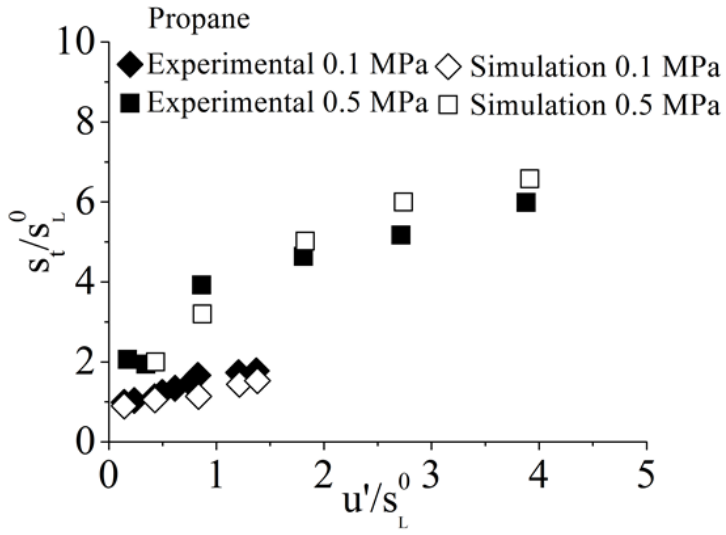

Figure 6.19: Comparison of turbulent flame speed at 1 and 5 bar using the simplified RANS Keppeler model for propane fuel

propane fuel. The model captures the correct scaling of s_t/s_L^0 with pressure for both methane and propane fuels. For a given pressure, in spite of under-prediction and over prediction of the turbulent flame speed, increasing trend of s_t/s_L^0 with increasing u'/s_L^0 is satisfactorily predicted by the RANS Keppeler model.

6.5 Investigation of $|\nabla\bar{c}|$ versus $|\nabla\tilde{c}|$ in FSD expression

It has been described in chapter 4, that the sum of the LES filtered reaction rate and molecular diffusion of the progress variable can be written in terms of a generalized flame surface density Σ_{gen}. Boger *et al.* [8] defined Σ_{gen}as:

$$\Sigma_{gen} = \overline{|\nabla c|} \tag{6.4}$$

The Σ_{gen}can be expressed in terms of subgrid scale wrinkling factor Ξ as:

$$\Sigma_{gen} = \Xi|\nabla\bar{c}| \tag{6.5}$$

where the wrinkling factor Ξ is defined as $\Xi = \overline{|\nabla c|} \,/\, |\nabla\bar{c}|$, or essentially the ratio of turbulent to laminar flame speed. When Eq. (6.5) is used in conjunction with Eq. (4.2), the issue of flame thickness control needs to be resolved. Ma *et al.* [52] reported that when the gradient-type $|\nabla\bar{c}|$ models are used without suitable CGT models, the predicted flame thickness grows in the simulation at a physically unrealistic rate. In practical cases, this issue is of secondary importance because: (a) the excessive growth of the predicted flame thickness is limited by the short residence time of the flame in the burner regions (b) in most of the cases, the flame location is a more significant quantity to know than the predicted flame thickness (c) the overall burning rate depends on the flame propagation. With the gradient-type $|\nabla\bar{c}|$ models, the turbulent flame speed is not affected by the flame brush thickness ($s_t \propto \int \Sigma_{gen}\, dx \propto \int \Xi|\nabla\bar{c}|\, dx$). It is shown in section 6.2.2 that when $|\nabla\tilde{c}|$ is used in Eq. (6.5) instead of $|\nabla\bar{c}|$, it acts like an implicit CGT SGSF model and controls the unrealistic thickening of the flame. In this section, the thickening of the flame with the gradient-type $|\nabla\bar{c}|$ models is investigated in conjunction with different CGT SGSF models as presented in section 4.3 using a simple 1D flame, where the turbulent wrinkling is entirely at the subgrid level.

6.5.1 Initial flame profile

For a stationary 1D flame at $t = 0$, the progress variable $\tilde{c}$, its first derivative $\partial\tilde{c}/\partial x$ and second derivative $\partial^2\tilde{c}/\partial x^2$ can be represented in terms of error function:

$$\tilde{c} = \frac{[1 + erf(x)]}{2}; \qquad erf(x) = \frac{2}{\sqrt{\pi}}\int_0^x e^{-x^2}\, dx \tag{6.6}$$

$$\frac{\partial \tilde{c}}{\partial x} = \frac{1}{\sqrt{\pi}} e^{-x^2} \tag{6.7}$$

$$\frac{\partial^2 \tilde{c}}{\partial x^2} = \frac{-2}{\sqrt{\pi}} e^{-x^2} x \tag{6.8}$$

6.5.2 Flame density and speed in terms of $\tilde{c}$

Progress variable is a normalized quantity, which can be written as:

$$c = \frac{T - T_u}{T_b - T_u} \tag{6.9}$$

Using the equation of state, temperature can be expressed in terms of pressure and density as $T = p/\rho R$. At constant pressure, Eq. (6.9) can be simplified as:

$$\bar{\rho} = \frac{\rho_u}{1 + \tau \tilde{c}} \tag{6.10}$$

where $\tau = \rho_u/\rho_b - 1$. The turbulent burning rate per unit area $\dot{m}$ can be written in terms of flame density and speed as:

$$\dot{m} = \text{constant};\ \rho u_x = \rho_u u_u = \rho_u s_t \quad (\text{for } u_u = s_t) \tag{6.11}$$

Substituting Eq. (6.10) into Eq. (6.11), the expression for flame speed in terms of progress variable can be written as:

$$\widetilde{u_x} = (1 + \tau \tilde{c}) s_t \tag{6.12}$$

From Eq. (6.10) and (6.12), $\partial \bar{\rho}/\partial x$ and $\partial \widetilde{u_x}/\partial x$ can be written as:

$$\frac{\partial \bar{\rho}}{\partial x} = -\frac{\rho_u \tau}{(1 + \tau \tilde{c})^2} \frac{\partial \tilde{c}}{\partial x} \tag{6.13}$$

$$\frac{\partial \widetilde{u_x}}{\partial x} = s_t \tau \frac{\partial \tilde{c}}{\partial x} \tag{6.14}$$

6.5.3 Expression for $\partial \bar{c}/\partial x$

The expression for $\partial \bar{c}/\partial x$ can be obtained using Eq. (5.1). For conciseness, only the final simplified expression is presented here:

$$\bar{c} = \frac{(1+\tau)\tilde{c}}{1+\tau\tilde{c}}; \quad \frac{\partial \bar{c}}{\partial x} = \frac{(1+\tau)}{(1+\tau\tilde{c})^2}\frac{\partial \tilde{c}}{\partial x} \tag{6.15}$$

6.5.4 1D progress variable transport equation with $|\nabla\tilde{c}|$ in FSD expression

For a 1D case, the Favre-filtered progress variable transport equation (Eq. (4.1)) can be written as:

$$\frac{\partial \bar{\rho}\tilde{c}}{\partial t} + \frac{\partial \bar{\rho}\tilde{c}\widetilde{u_x}}{\partial x} + \frac{\partial}{\partial x}(\bar{\rho}\widetilde{u_x c} - \bar{\rho}\widetilde{u_x}\tilde{c}) = \frac{\partial}{\partial x_x}\left(\overline{\rho\alpha\frac{\partial c}{\partial x_x}}\right) + \bar{\dot{\omega}} = \rho_u s_L \Xi \left|\frac{\partial \tilde{c}}{\partial x}\right| = \rho_u s_t \left|\frac{\partial \tilde{c}}{\partial x}\right| \tag{6.16}$$

Using continuity equation (Eq. (2.1)), the above equation can be simplified as:

$$\bar{\rho}\frac{\partial \tilde{c}}{\partial t} = \rho_u s_t \left|\frac{\partial \tilde{c}}{\partial x}\right| - \bar{\rho}\widetilde{u_x}\frac{\partial \tilde{c}}{\partial x} - \frac{\partial}{\partial x}(\bar{\rho}\widetilde{u_x c} - \bar{\rho}\widetilde{u_x}\tilde{c}) \tag{6.17}$$

For a flame with $u_u = s_t$, the first and second terms on RHS of Eq. (6.16) will become zero (using Eq. (6.11)) and we are left with:

$$\bar{\rho}\frac{\partial \tilde{c}}{\partial t} = -\frac{\partial}{\partial x}(\bar{\rho}\widetilde{u_x c} - \bar{\rho}\widetilde{u_x}\tilde{c}) \tag{6.18}$$

The above equation shows that the thickness of the flame depends on the gradient or counter-gradient nature of the used SGSF model. If SGSF model is of gradient-type, the flame thickness will be increased and vice versa.

6.5.5 1D progress variable transport equation with $|\nabla\bar{c}|$ in FSD expression

Equation (6.17) is developed using $|\nabla\tilde{c}|$ in the FSD expression. A similar expression can be developed using Eq. (6.18) together with Eqs. (2.1) and (6.15):

$$\bar{\rho}\frac{\partial \tilde{c}}{\partial t} = \rho_u s_t \left|\frac{\partial \bar{c}}{\partial x}\right| - \bar{\rho}\widetilde{u_x}\frac{\partial \tilde{c}}{\partial x} - \frac{\partial}{\partial x}(\bar{\rho}\widetilde{u_x c} - \bar{\rho}\widetilde{u_x}\tilde{c}) \tag{6.19a}$$

Using Eq. (6.11), the above equation can be written as:

$$\bar{\rho}\frac{\partial \tilde{c}}{\partial t} = \left[\frac{(1+\tau)}{(1+\tau\tilde{c})^2} - 1\right]\rho_u s_t \frac{\partial \tilde{c}}{\partial x} - \frac{\partial}{\partial x}\left(F_x^{sg}\right) \tag{6.19b}$$

The first term on RHS of Eq. (6.19b) is denoted in the rest of the work with term X. Since $[(1+\tau)/(1+\tau\tilde{c})^2] > 1$, the term X is of gradient-type. Figure 6.20a shows the plot of term X and it can be seen that it would induce strong flame thickening, which is not uniform at the unburnt and burnt flame sides. The second term on RHS side of Eq. (6.19b) represents the subgrid scalar flux (SFSF), which should be of counter-gradient type in order to counter balance the physically unrealistic thickening of the flame.

6.5.6 Gradient hypothesis based model

The most conventional way to model SGSF term is to use the gradient hypothesis based model:

$$-\frac{\partial}{\partial x}\left(F_x^{sg}\right) = \frac{\partial}{\partial x}\left(\bar{\rho}\frac{\nu_{sgs}}{Sc_t}\frac{\partial \tilde{c}}{\partial x}\right) \tag{6.20}$$

In Eq. (6.20), ν_{sgs} is the subgrid turbulent eddy viscosity and it is calculated using the Smagorinsky model [69]:

$$\nu_{sgs} = (C_s\Delta)^2\sqrt{2S_{\mathrm{ij}}S_{\mathrm{ij}}}; \quad S_{\mathrm{ij}} = 0.5\left(\frac{\partial \widetilde{u_{\mathrm{i}}}}{\partial x_{\mathrm{j}}} + \frac{\partial \widetilde{u_{\mathrm{j}}}}{\partial x_{\mathrm{i}}}\right) \tag{6.21}$$

For the 1D case, Eq. (6.21) can be simplified as:

$$\nu_{sgs} = (C_s\Delta)^2\sqrt{2}\frac{\partial \widetilde{u_x}}{\partial x}; \quad S_{xx} = \frac{\partial \widetilde{u_x}}{\partial x} \tag{6.22}$$

C_s is the Smagorinsky constant and a theoretical value of 0.18 for isotropic turbulence is used in this analysis. Using Eqs. (6.22) and (6.14), Eq. (6.20) can be simplified as:

$$-\frac{\partial}{\partial x}(F_x^{sg}) = Sc_t^{-1}(C_s\Delta)^2\sqrt{2}\frac{\partial}{\partial x}\left(\bar{\rho}\frac{\partial \widetilde{u_x}}{\partial x}\frac{\partial \tilde{c}}{\partial x}\right) = Sc_t^{-1}(C_s\Delta)^2\sqrt{2}\,s_t\tau\frac{\partial}{\partial x}\left(\bar{\rho}\frac{\partial \tilde{c}}{\partial x}\frac{\partial \tilde{c}}{\partial x}\right) = A\frac{\partial}{\partial x}\left[\bar{\rho}\left(\frac{\partial \tilde{c}}{\partial x}\right)^2\right]$$

$$-\frac{\partial}{\partial x}\left(F_x^{sg}\right) = A\left[2\bar{\rho}\frac{\partial \tilde{c}}{\partial x}\frac{\partial^2 \tilde{c}}{\partial x^2} + \frac{\partial \bar{\rho}}{\partial x}\left(\frac{\partial \tilde{c}}{\partial x}\right)^2\right] = A\left[2\bar{\rho}\frac{\partial \tilde{c}}{\partial x}\frac{\partial^2 \tilde{c}}{\partial x^2} - \frac{\rho_u\tau}{(1+\tau\tilde{c})^2}\left(\frac{\partial \tilde{c}}{\partial x}\right)^3\right] \tag{6.23}$$

where $A = Sc_t^{-1}(C_s\Delta)^2\sqrt{2}\,s_t\tau$. For the present analysis, Sc_t is taken to be 0.75 as it assumes a value of order of unity for gaseous flow. Figure 6.20b shows the plot of Eq. (6.23) and it can be

seen that it is of gradient-type and would induce additional flame thickening rather than counter balancing the strong flame thickening induced by term X.

6.5.7 CLARK model

The second term on RHS of Eq. (6.19b) can also be calculated using the CLARK model (Eq. (4.22)):

$$-\frac{\partial}{\partial x}\left(F_x^{sg}\right) = -\frac{\partial}{\partial x}\left(\bar{\rho}\frac{\Delta^2}{12}\frac{\partial\widetilde{u_x}}{\partial x}\frac{\partial\tilde{c}}{\partial x}\right) = -\frac{\Delta^2}{12}s_t\tau\frac{\partial}{\partial x}\left(\bar{\rho}\frac{\partial\tilde{c}}{\partial x}\frac{\partial\tilde{c}}{\partial x}\right) = B\frac{\partial}{\partial x}\left[\bar{\rho}\left(\frac{\partial\tilde{c}}{\partial x}\right)^2\right]$$

$$-\frac{\partial}{\partial x}\left(F_x^{sg}\right) = -B\left[2\bar{\rho}\frac{\partial\tilde{c}}{\partial x}\frac{\partial^2\tilde{c}}{\partial x^2} - \frac{\rho_u\tau}{(1+\tau\tilde{c})^2}\left(\frac{\partial\tilde{c}}{\partial x}\right)^3\right] \tag{6.24}$$

where $B = (\Delta^2/12)\, s_t\tau$. Figure 6.20c shows the plot of Eq. (6.24) and it can be seen that it is of weak counter gradient-type and has the potential to counter balance the strong flame thickening induced by term X, provided that the model constant B is increased to capture the right quantitative trend.

6.5.8 HUAI model

The SGSF term in Eq. (6.19b) can also be modelled using the HUAI model:

$$-\frac{\partial}{\partial x}\left(F_x^{sg}\right) = -\frac{\partial}{\partial x}\left(-\bar{\rho}\frac{\nu_{sgs}}{Sc_t}\frac{\partial\tilde{c}}{\partial x} + \bar{\rho}\, D_{an}\Delta^2\widetilde{S_{xx}}\frac{\partial\tilde{c}}{\partial x}\right) \tag{6.25}$$

The first and second terms on RHS of Eq. (6.25) account for the gradient and counter-gradient contributions to F_x^{sg}, respectively. The former term is already simplified to Eq. (6.23) and the latter term can be simplified as:

$$-\frac{\partial}{\partial x}\left(F_x^{sg}\right)_{CGT} = -D_{an}\Delta^2\frac{\partial}{\partial x}\left(\bar{\rho}\,\frac{\partial\widetilde{u_x}}{\partial x}\,\frac{\partial\tilde{c}}{\partial x}\right) = -D_{an}\Delta^2 s_t\tau\frac{\partial}{\partial x}\left[\bar{\rho}\left(\frac{\partial\tilde{c}}{\partial x}\right)^2\right]$$

$$-\frac{\partial}{\partial x}\left(F_x^{sg}\right)_{CGT} = -C\left[2\bar{\rho}\frac{\partial\tilde{c}}{\partial x}\frac{\partial^2\tilde{c}}{\partial x^2} - \frac{\rho_u\tau}{(1+\tau\tilde{c})^2}\left(\frac{\partial\tilde{c}}{\partial x}\right)^3\right] \tag{6.26}$$

Substituting Eqs. (6.26) and (6.23) into Eq. (6.25):

$$-\frac{\partial}{\partial x}\left(F_x^{sg}\right) = (A - C)\left[2\bar{\rho}\frac{\partial \tilde{c}}{\partial x}\frac{\partial^2 \tilde{c}}{\partial x^2} - \frac{\rho_u \tau}{(1+\tau\tilde{c})^2}\left(\frac{\partial \tilde{c}}{\partial x}\right)^3\right] \tag{6.27}$$

where $C = D_{an}\Delta^2 s_t \tau$. Figure 6.20d shows the plot of Eq. (6.27) and it can be seen that the HUAI model performs similar to the CLARK model. The strong flame thickening induced by term X can be counter balanced by using the HUAI model, provided that the model constant C is increased to capture the right quantitative trend.

6.5.9 WELLER model

In this section, the WELLER model (Eq. (4.24)) is used to calculate the SGSF term:

$$-\frac{\partial}{\partial x}\left(F_x^{sg}\right) = -\frac{\partial}{\partial x}\left(-\bar{\rho}\frac{\nu_{sgs}}{Sc_t}\frac{\partial \tilde{c}}{\partial x} - \rho_u s_L\, \Xi\, N_x\, (\bar{c} - \tilde{c})\right) \tag{6.28}$$

The second term, which accounts for the counter-gradient contribution to F_x^{sg} can be simplified as:

$$-\frac{\partial}{\partial x}\left(F_x^{sg}\right)_{CGT} = \rho_u s_L\, \Xi \frac{\partial}{\partial x}\left[N_x\, (\bar{c} - \tilde{c})\right] = \rho_u s_L \frac{s_t}{s_L}\left[(\bar{c} - \tilde{c})\frac{\partial N_x}{\partial x} + N_x\frac{\partial \bar{c}}{\partial x} - N_x\frac{\partial \tilde{c}}{\partial x}\right] \tag{6.29}$$

The first term on RHS of Eq. (6.29) will be cancelled out since for the 1D case $N_x = -1$, Eq. (6.29) becomes:

$$-\frac{\partial}{\partial x}\left(F_x^{sg}\right)_{CGT} = \rho_u s_t\left(N_x\frac{\partial \bar{c}}{\partial x} - N_x\frac{\partial \tilde{c}}{\partial x}\right) = \rho_u s_t\left(\left|\frac{\partial \tilde{c}}{\partial x}\right| - \left|\frac{\partial \bar{c}}{\partial x}\right|\right) \tag{6.30}$$

Figure 6.20e shows the plot of Eq. (6.30) and it can be seen that it is quantitatively exactly equal to the term X in Eq. (6.21) but with opposite sign. Substituting Eq. (6.30) into Eq. (6.19b) with the gradient transport term, the term X will be canceled out and an equation similar to Eq. (6.18) is obtained. This shows that with using the WELLER model for the 1D case, $|\nabla \bar{c}|$ in the FSD expression is changed to $|\nabla \tilde{c}|$ and implicitly account for the CGT effects in the FSD source term.

6.5.10 RICHARD model

It can be observed by comparing the expressions of RICHARD and WELLER models (Eqs. (4.23) and (4.24)) that the RICHARD CGT model is developed by setting $\Xi = 1$, so the

simplified expression for the RICHARD CGT model can be developed in a similar way used to obtain Eq. (6.30):

$$-\frac{\partial}{\partial x}\left(F_x^{sg}\right)_{CGT} = \frac{\partial}{\partial x}[\rho_u s_L N_x(\bar{c}-\tilde{c})] = \rho_u s_L\left[\left|\frac{\partial \tilde{c}}{\partial x}\right| - \left|\frac{\partial \bar{c}}{\partial x}\right|\right] = -\rho_u s_L\left[\frac{(1+\tau)}{(1+\tau\tilde{c})^2}-1\right]\left|\frac{\partial \tilde{c}}{\partial x}\right| \quad (6.31)$$

Figure 6.20f shows the plot of Eq. (6.31). Substituting Eq. (6.31) into Eq. (6.19) with the gradient transport term, Eq. (6.19) becomes:

$$0 = \rho_u s_L(\Xi-1)\left[\frac{(1+\tau)}{(1+\tau\tilde{c})^2}-1\right]\left|\frac{\partial \tilde{c}}{\partial x}\right| + \frac{\partial}{\partial x}\left(\bar{\rho}\frac{\nu_{sgs}}{Sc_t}\frac{\partial \tilde{c}}{\partial x}\right) \quad (6.32)$$

For $\Xi = 1$, i.e. for a laminar flame the RICHARD model performs similar to the WELLER model and the first term on RHS side of Eq. (6.32) is cancelled out. However, for $\Xi > 1$, the flame thickening effect from $|\nabla \bar{c}|$ is largely retained.

6.5.11 TULLIS model

In this section, the TULLIS model (Eq. (4.25)) is used to calculate the SGSF term:

$$\frac{\partial}{\partial x}\left(F_x^{sg}\right) = -\frac{\partial}{\partial x}\left[-\alpha_E \bar{\rho}\frac{\nu_{sgs}}{Sc_t}\frac{\partial \tilde{c}}{\partial x} - \bar{\rho} s_L\, \Xi\, N_x \tau\, \tilde{c}(1-\tilde{c})\right] \quad (6.33)$$

The second term which accounts for the counter-gradient contribution to F_x^{sg} can be simplified as:

$$-\frac{\partial}{\partial x}\left(F_x^{sg}\right)_{CGT} = s_L\, \Xi\tau\frac{\partial}{\partial x}[\bar{\rho}\, N_x \tilde{c}(1-\tilde{c})] = s_t\, \tau\frac{\partial}{\partial x}[\bar{\rho}\, N_x \tilde{c}(1-\tilde{c})\,]$$

$$-\frac{\partial}{\partial x}\left(F_x^{sg}\right)_{CGT} = s_t\, \tau\left[\frac{\partial \bar{\rho}}{\partial x}N_x\tilde{c}(1-\tilde{c}) + \bar{\rho}\frac{\partial N_x}{\partial x}\tilde{c}(1-\tilde{c}) + \bar{\rho}\, N_x\frac{\partial \tilde{c}}{\partial x}(1-\tilde{c}) - \bar{\rho}\, N_x\tilde{c}\frac{\partial \tilde{c}}{\partial x}\right]$$

$$-\frac{\partial}{\partial x}\left(F_x^{sg}\right)_{CGT} = s_t\, \tau\left[-\frac{\rho_u\tau}{(1+\tau\tilde{c})^2}\frac{\partial \tilde{c}}{\partial x}\, N_x\tilde{c}(1-\tilde{c}) + \bar{\rho}\, N_x\frac{\partial \tilde{c}}{\partial x} - 2\bar{\rho}\, N_x\tilde{c}\frac{\partial \tilde{c}}{\partial x}\right]$$

$$-\frac{\partial}{\partial x}\left(F_x^{sg}\right)_{CGT} = s_t\, \tau\left[\frac{\rho_u\tau}{(1+\tau\tilde{c})^2}\left|\frac{\partial \tilde{c}}{\partial x}\right|\tilde{c}(1-\tilde{c}) - \bar{\rho}\,\left|\frac{\partial \tilde{c}}{\partial x}\right| + 2\bar{\rho}\,\tilde{c}\left|\frac{\partial \tilde{c}}{\partial x}\right|\right]$$

$$-\frac{\partial}{\partial x}\left(F_x^{sg}\right)_{CGT} = D\left|\frac{\partial \tilde{c}}{\partial x}\right|\left[\frac{\rho_u\tau}{(1+\tau\tilde{c})^2}\,\tilde{c}(1-\tilde{c}) - \bar{\rho}\, + 2\bar{\rho}\,\tilde{c}\right] \quad (6.34)$$

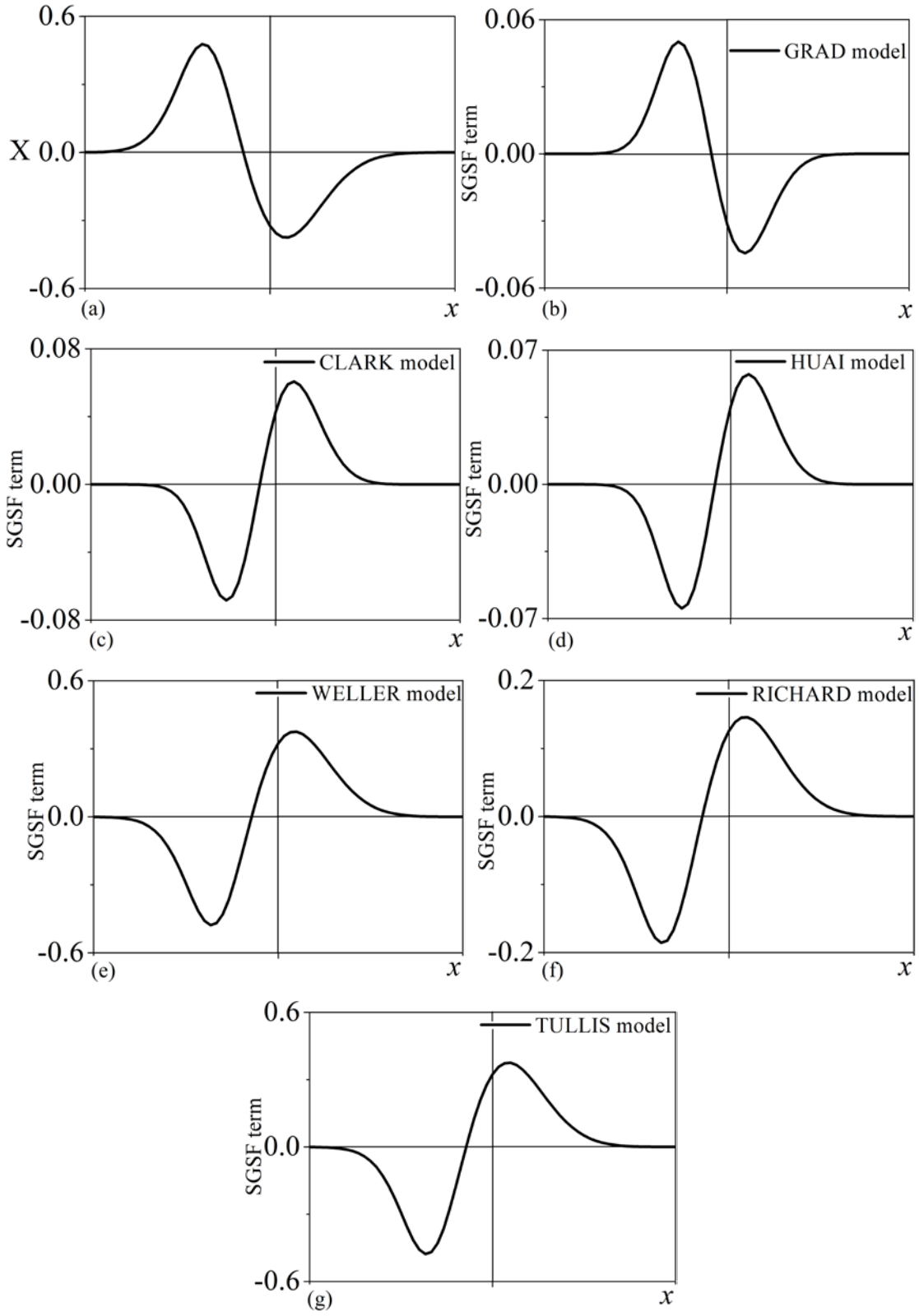

Figure 6.20: Plot of (a) term X and SGSF term using: (b) GRAD model (c) CLARK model (d) HUAI model (e) WELLER model (f) RICHARD model (g) TULLIS model

where $D = s_t\,\tau$. Figure 6.20g shows the plot of Eq. (6.34) and it can be seen that the TULLIS model performs similar to the WELLER model, as explained in section 4.3. The trends viewed with the WELLER model in section 6.5.9 are also observed with the TULLIS model.

Chapter 7

Conclusions

In the present study, different modifications have been made to an already established subgrid scale FSD model to investigate various features of turbulent premixed combustion of considerable importance. The main findings of the present study are concluded as following:

- The performance of a simplified version of the original Keppeler model is investigated. The simplifications to the original Keppeler model are discussed and its performance is compared to the original model and validated with the experimental data. The simplified Keppeler model showed a satisfactory performance. The numerical predictions of turbulent flame speeds with both models, at conditions typical for spark-ignition engines and industrial gas turbines, match with the experimental data satisfactorily well. However, the flame speeds obtained with the simplified model are slightly lower than the values obtained with the original model.
- The performance of the original Keppeler model is investigated in conjunction with three different closures of SGSF: classical gradient hypothesis closure, Clark's tensor diffusivity model and Huai's model. Originally it was used together with a gradient hypothesis closure for SGSF [53]. The results show that the turbulent flame speed is not significantly affected by SGSF closure and the numerical predictions of turbulent flame speed match the experimental data reasonably well, independent of the SGSF closure. However, the flame shape and thickness are modified by the more advanced SGSF closure to some extent. A-priori analysis based on an existing DNS database yielded a qualitatively similar model behavior as obtained from a-posteriori model assessments using LES simulations, in the sense that no clear advantage could be seen when using more sophisticated SGSF models in combination with the FSD closure applied in the Keppeler model. Detailed physical explanations have been provided for the observed influences of SGSF closure on the overall performance of the Keppeler model. It has been identified that replacing the filtered reaction progress variable with its Favre filtered counterpart in the expression of the resolved FSD was shown to act as an implicit CGT

model and consequently, explicit treatment of the CGT part of SGSF becomes less important, if not redundant. Hence, it leads the comparatively good performance of the gradient flux approximation in combination with the particular closure of FFFD term used in the Keppeler model.

- An extensive numerical study, supported with the analytical work, is performed to investigate the effects of pressure and fuel type in the reaction rate closure using some of the popular algebraic flame surface density reaction rate closure models available in open literature. The numerical predictions are compared with the well documented experimental data for lean methane and propane fuels for different flow and turbulence inlet conditions at operating pressures between 1 and 10 bar. With the original versions of the selected models, turbulent flame speed is under-predicted with difference growing larger for larger pressure. The model constants were tuned and the pressure corrections obtained with the KPP analysis were incorporated to achieve correct pressure dependency of the turbulent flame speed. Following the work available in the open literature, a new term was incorporated (1/*Le*) introducing the fuel effects in the reaction rate closure of the Keppeler and Fureby models. With these changes, the models predict the turbulent flame speed values in a very good agreement with the experimental data. The tuned models now include two important aspects of technical relevance, i.e. the influence of the Lewis number for different fuels and high-pressure effects on the reaction rate.
- A RANS version of the Keppeler model [53], which is originally derived for the LES of premixed flames, is developed and its performance is investigated. The results from the new RANS model showed a satisfactory performance in comparison with its LES counterpart and experimental data.
- Lastly, the effects of replacing Reynolds-averaged progress variable $\bar{c}$ with its Favre filtered counterpart $\tilde{c}$ in the expression of FSD is investigated in combination with different SGSF models in a 1D formulation. The presence of $|\nabla \bar{c}|$ in the FSD expression results in a physically unrealistic thickening of the flame which can be counter-balanced by using suitable SGSF models (e.g. WELLER or TULLIS models) that account for the flux of CGT type.

Bibliography

[1] International Energy Outlook 2016 http://www.eia.gov/forecasts/ieo/world.cfm

[2] N. Peters, Turbulent combustion, Cambridge University Press, 2000.

[3] J. Janicka, and A. Sadiki, Large eddy simulation for turbulent combustion. Proceedings of Combustion Institute, 30 (1):537–547, 2005.

[4] H. Pitsch, Large eddy simulation of turbulent combustion. Annual Review of Fluid Mechanics, 38:453 – 482, 2006.

[5] S. Menon and W. Jou, Large eddy simulations of combustion instability in an axisymmetric ramjet combustor, Combust. Sci. Tech.,75:53-72, 1991.

[6] T. D. Butler and P. J. O'Rourke, A numerical method for two dimensional unsteady reacting flows, Proc. Sym. (Int.) Combust., 16:1503-151, 1977.

[7] O. Colin, F. Ducros, D. Veynante, and T. Poinsot, A thickened flame model for large eddy simulations of turbulent premixed combustion, Phys. Fluids vol. 12, pp. 1843-1863, 2000.

[8] M. Boger, D. Veynante, H. Boughanem and A. Trouvé, Direct numerical simulation analysis of flame surface density concept for large eddy simulation of turbulent premixed combustion, Proc. Sym. (Int.) Combust., 27:917-925, 1998.

[9] E. R. Hawkes and R. S. Cant, A flame surface density approach to large eddy simulation of premixed turbulent combustion, Proc. Combust. Inst., 28:51–58, 2000.

[10] N. Chakraborty and R. S. Cant, A priori analysis of the curvature and propagation terms of the flame surface density transport equation for large eddy simulation, Phys. Fluids, 19:105101, 2007.

[11] N. Chakraborty and R. S. Cant, Direct numerical simulation analysis of the flame surface density transport equation in the context of large eddy simulation, Proc. Combust. Inst. 32: 1445–1453, 2009.

[12] E. Hawkes and R. S. Cant, Implications of a flame surface density approach to large eddy simulation of turbulent premixed combustion, Combust. Flame, 126: 1617–1629, 2001.

[13] S. Richard, O. Colin, O. Vermorel, C. Angelberger, A. Benkenida and D. Veynante, Towards large eddy simulation of combustion in spark ignition engines, Proc. Combust. Inst. 31: 3059–3066, 2007.

[14] R. Knikker, D. Veynante and C. Meneveau, A dynamic flame surface density model for large eddy simulation of turbulent premixed combustion, Phys. Fluids, 16: 91–94, 2004.

[15] G. Wang, M. Boileau, D. Veynante and K. Truffin, Large eddy simulation of a growing turbulent premixed flame kernel using a dynamic flame surface density model, Combust. Flame, 159: 2742–2754, 2012.

[16] C. Duwig and C. Fureby, Large eddy simulation of unsteady lean stratified premixed combustion, Combust. Flame, 151:85–103, 2007.

[17] N. Aluri, S. P. R. Muppala and F. Dinkelacker, Large-eddy simulation of lean premixed turbulent flames of three different combustion configurations using a novel reaction closure, Flow Turbul. Combust. 80:207–224, 2008.

[18] B. Fiorina, R. Vicquelin, P. Auzillon, N. Darabiha, O. Gicquel and D. Veynante, A filtered tabulated chemistry model for LES of premixed combustion. Combust. Flame, 157(3):465-475, 2010.

[19] B. Fiorina, R. Mercier, G. Kuenne, A. Ketelheun, A. Avdic, J. Janicka, D. Geyere, A. Dreizler, E. Alenius, C. Duwig, P. Trisjono, K. Kleinheinz, S. Kang, H. Pitsch, F. Proch, F. C. Marincola and A. Kempf, Challenging modelling strategies for LES of non-adiabatic turbulent stratified combustion. Combust. Flame, 162:4264-4282, 2015.

[20] B. B. Mandelbrot, On the geometry of homogeneous turbulence, with stress on the fractal dimension of the Iso-surfaces of scalars. Journal of Fluid Mechanics, 72 (3):401–416, 1975.

[21] K. R. Sreenivasan, Fractals and multifractals in fluid turbulence. Annual Review of Fluid Mechanics, 23 (1):539–600, 1991.

[22] G. L. Santavicca and D. A.North, The Fractal nature of premixed turbulent flames". Combustion Science and Technology, 72(4): 215-232, 1990.

[23] F. Gouldin, An application of fractals to modelling to premixed flames". Combustion and Flame, 68(3): 249-266, 1987.

[24] F. Gouldin, K. Bray and J. Y Chen, Chemical closure model for fractal flamelets". Combustion and Flame, 77(3-4):241-259, 1989.

[25] F. Charlette, C. Meneveau and D. Veynante, A power-law flame wrinkling model for LES of premixed turbulent combustion. Part I: Non-dynamic formulation and initial tests," Combustion and Flame 131:159-180, 2002.

[26] P. A. Libby and K. N. C. Bray, Counter-gradient diffusion in premixed turbulent flames, AIAA J., 19:205-213, 1981.

[27] K. N. C. Bray, P. A. Libby and J. B. Moss, Unified modelling approach for premixed turbulent combustion-part I: general formulation, Combust. Flame, 61:87–102, 1985.

[28] J. B. Moss, Simultaneous measurements of concentration and velocity in an open premixed turbulent flame, Combust. Sci. Technol., 22:119–129, 1980.

[29] R. K. Cheng, Conditional Sampling of Turbulence Intensities and Reynolds Stress in Premixed Turbulent Flames, Combust. Sci. Technol., vol. 41, pp. 109–142, 1984.

[30] N. W. H. Armstrong and K. N. C. Bray, Premixed turbulent combustion flow field measurements using PIV and LST and their Application to flamelet modelling of engine combustion, SAE Paper 92-2322, 1992.

[31] Y. C. Chen and R. W. Bilger, Turbulence and scalar transport in premixed bunsen flames of lean hydrogen/air mixtures, Proc. Combust. Inst., 21:521–528, 2000.

[32] S. Pfadler, A. Leipertz, F. Dinkelacker, J. Waesle, A. Winkler and T. Sattelmayer, Two-dimensional direct measurement of the turbulent flux in turbulent premixed swirl flames, Proc. Combust. Inst., 31:1337–1344, 2007.

[33] S. Pfadler, A. Leipertz and F. Dinkelacker, Systematic experiments on turbulent premixed bunsen flames including turbulent flux measurements, Combust. Flame, 152:616–631, 2008.

[34] C. J. Rutland and R.S. Cant, Turbulent transport in premixed flames, Pro. Summer Progr., Cent. Turbul. Res., NASA Ames/ Stanford University,75–94, 1994.

[35] D. Veynante, A. Trouvé, K. N. C. Bray and T. Mantel, Gradient and counter-gradient scalar transport in turbulent premixed flames, J. Fluid Mech., 332: 263–293, 1997.

[36] N. Swaminathan, R.W. Bilger and B. Cuenot, Relationship between turbulent scalar flux and conditional dilatation in premixed flames with complex chemistry, Combust. Flame, 126: 1764-1779, 2001.

[37] S. Nishiki, T. Hasegawa, R. Borghi and R. Himeno, Modelling of turbulent scalar flux in turbulent premixed flames based on DNS database, Combust. Theor. Model., 10: 39-55, 2006.

[38] N. Chakraborty and R. S. Cant, Physical Insight and Modelling for Lewis Number Effects on Turbulent Heat and Mass Transport in Turbulent Premixed Flames, Num. Heat Trans. A, 55:762-779, 2009.

[39] N. Chakraborty and R. S. Cant, Effects of Turbulent Reynolds Number on the Modelling of Turbulent Scalar Flux in Premixed Flames, Num. Heat Trans. A, vol. 67(11), pp. 1187-1207, 2015.

[40] S. Pfadler, F. Dinkelacker, F. Beyrau and A. Leipertz, High Resolution Dual-plane Stereo-PIV for Validation of Subgrid Scale Models in Large Eddy Simulations of Turbulent Premixed Flames, Combust. Flame, vol. 156, pp. 1552-1564, 2009.

[41] S. Pfadler, J. Kerl, F. Beyrau, A. Leipertz, A. Sadiki, J. Scheuerlein, and F. Dinkelacker, Direct Evaluation of the Subgrid Scale Scalar Flux in Turbulent Premixed Flames with Conditioned Dual-plane Stereo-PIV, Proc. Combust. Inst., vol. 32, pp. 1723-1730, 2009.

[42] G. Lecocq, S. Richard, O. Colin and L. Vervisch, Gradient and counter-gradient modelling in premixed flames: theoretical study and application to the LES of a lean premixed turbulent swirl-burner, Combust. Sci. Technol.,182:465-479, 2010.

[43] Y. Gao, N. Chakraborty and M. Klein, Assessment of the performances of sub-grid scalar flux models for premixed flames with different global Lewis numbers: a Direct Numerical Simulation analysis, Int. J. Heat Fluid Flow, 52:28–39, 2015.

[44] Y. Gao, M. Klein and N. Chakraborty, Assessment of sub-grid scalar flux modelling in premixed flames for Large Eddy simulations: A-priori Direct Numerical Simulation analysis, Eur. J. Mech. - B/Fluids, vol. 52, pp. 97–108, 2015.

[45] Y. Huai, A. Sadiki, S. Pfadler, M. Loffler, F. Beyrau, A. Leipertz and F. Dinkelacker, Experimental assessment of scalar flux models for Large Eddy Simulations of non-reacting flows, Turbulence Heat Mass Transfer, 5:263–266, 2006.

[46] R. A. Clark, J. H. Ferziger and W. C. Reynolds, Evaluation of Subgrid-scale Models using an Accurately Simulated Turbulent Flow, J. Fluid Mech., 91:1–16, 1979.

[47] H. Kobayashi, T. Nakashima, T. Tamura, K. Maruta and T. Niioka, Turbulence measurements and observations of turbulent premixed flames at elevated pressures up to 3.0 MPa, Combust. Flame, 108:104–117, 1997.

[48] A. Bounif, A. Aris and I. Gökalp, Pressure effects on the spectral behaviour of the thermal field in non-reacting and low Damköhler reacting flows, Int. J. Therm. Sci., 38:819–831, 1999.

[49] A. Soika, F. Dinkelacker and A. Leipertz, Pressure influence on the flame front curvature of turbulent premixed flames: comparison between experiment and theory, Combust. Flame. 132:451–462, 2003.

[50] A. N. Lipatnikov and J. Chomiak, Molecular transport effects on turbulent flame propagation and structure, Prog. Energy Combust. Sci., 31:1–71, 2005.

[51] N. Chakraborty and M. Klein, A priori direct numerical simulation assessment of algebraic flame surface density models for turbulent premixed flames in the context of large eddy simulation, Phys. Fluids, 20: 85-108, 2008.

[52] T. Ma , O. T. Stein , N. Chakraborty and A. M. Kempf, A posteriori testing of algebraic flame surface density models for LES, 17: 431-482, 2013.

[53] K. Keppeler, E. Tangermann, U. Allauddin and M. Pfitzner, LES of low to high turbulent combustion in an elevated pressure environment, Flow Turbul. Combust., 92:767-802, 2014.

[54] R. Lindstedt and E. Váos, Modelling of premixed turbulent fames with second moment methods, Combust. Flame, 116:461-485, 1999.

[55] T. Poinsot and D. Veynante, Theoretical and numerical Combustion, 2nd edition, Edwards, 2005.

[56] Peter Gerlinger. Numerische Verbrennungssimulation. Springer Berlin / Heidelberg, 2005.

[57] D. Veynante and L. Vervisch, Turbulent combustion modelling. Progress in Energy and Combustion Science, 28:193-266, 2002.

[58] OpenFOAMCFD Limited . OpenFOAM User Guide http://cfd.direct/openfoam/user-guide/

[59] A. N. Kolmogorov, The local structure of turbulence in incompressible viscous fluids for very large Reynolds numbers, Proc. Roy. Soc. Lond. A., 434:9-13, 1991.

[60] L. Davidson, Lecture notes Dept. of Thermo and Fluid Dynamics, Chalmers University of Technology, Goteborg, Swedon, 2000.

[61] T. V. Boussinesq, Théorie de l'écoulement tourbillonnant, Mém. Prés. Acad. Sci., Paris, XX111, 46, 1877.

[62] L. Prandtl, Bemerkung zur theorie der freien turbulenz, Z.A.M.M., 22:241-243, 1942.

[63] P. Y. Chou, On the velocity correlations and the solution of the equations of turbulent fluctuation, Quart. Appl. Math., 3:38, 1945.

[64] B. E. Launder and B. I. Sharma, Application of the energy dissipation model of turbulence to the calculation of flow near a spinning disc", Letters in Heat Mass Transf., 1(2):131-138. 1974.

[65] D. C. Wilcox, Re-assessment of the scale-determining equation for advanced turbulence models, AIAA Journal, 26(11):1299-1310, 1988.

[66] F. R. Menter, Performance of popular turbulence models for attached and separated adverse pressure gradient flow, AIAA J. 30:2066-2072, 1992.

[67] F. R. Menter, Improved two-equation $k-\omega$ turbulence models for aerodynamics flows, NASA Technical Memorandum TM-103975, NASA Amess, CA, 1992.

[68] A. Leonard, Energy cascade in large-eddy simulations of turbulent fluid flows, Adv. Geophys., 18:237-248, 1974.

[69] J. Smagorinsky. General circulation experiments with the primitive equations I. the basic experiment. Mon. Weather Rev., 91(3):99-164, 1963.

[70] M. Germano, U. Piomelli, P. Moin and W.H. Cabot. A dynamic subgrid-scale eddy viscosity model, Phys. Fluids, 3(7):1760-1765, 1991.

[71] U. Schumann, Subgrid scale model for finite difference simulations of turbulent flows in plane channels and annuli, J. Computational Physics, 18(1):376–404, 1975.

[72] C. Fureby, G. Tabor, H. G.Weller and A. D. Gosman, A comparative study of subgrid scale models in homogeneous isotropic turbulence, Phys. Fluids, 9(5):1416–1429, 1997.

[73] I. Gökalp, An evaluation of the Klimov-Williams criterion, Proc. Combust. Inst., 67:111-119, 1987.

[74] X. J. Gu, M. Z. Haq, M. Lawes and R. Woolley, Laminar burning velocity and Markstein lengths of methane-air mixtures. Combust. Flame, 121:41-58, 2000.

[75] M. Metghalchi and J. C. Keck, Laminar burning velocity of propane-air mixtures at high temperature and pressures. Combust. Flame, 38:143-154, 1980.

[76] G. E. Andrew, D. Bradley and S. B. Lwakabamba, Turbulence and turbulent flame propagation-a critical appraisal, Combust. Flame, 24:285-304, 1975.

[77] G. Damköhler, The effect of turbulence on the flame velocity in gas mixtures, Z. Electrochem, 46:601-626, 1940. (English translation NASA Tech. Mem. 1112, 1947.

[78] P. Clavin and F. A. Williams, Effects of molecular diffusion and of thermal expansion on the structure and dynamics of premixed flames in turbulent flows of large scale and low intensity, J. Fluid Mechanics, 116:251-282, 1982.

[79] A. M. Klimov, Premixed turbulent flames-interplay of hydrodynamics and chemical phenomena, in Flames, Lasers and reactive systems (J. R. Bowen, N. Manson, A. K . Oppenheim and R. I. Soloukin, eds.), Progress in Astronautics and Aeronautics, 88:133-146, 1983.

[80] R. G. Abdel-Gayed, K.J. Al-Khishali and D. Bradley, Turbulent burning velocities and flame straining in explosions. Proc. Roy. Soc. Lond. A., 391:393-414, 1984.

[81] R. G. Abdel-Gayed and D. Bradley. A two-eddy theory of premixed turbulent flame propagation. Phil. Trans. Roy. Soc. Lond., 301:1-25, 1981.

[82] H. Kobayashi, Y. Kawabata and K. Maruta. Experimental study on general correlation of turbulent burning velocity at high-pressure. Proc. Combust. Inst., 27:941-948, 1998.

[83] H. Kobayashi, T. Tamura, K. Maruta and T. Niioka. Burning velocity of turbulent premixed flame in a high-pressure environment. Proc. Combust. Inst., 26:389-396, 1996.

[84] R. Borghi, On the structure and morphology of turbulent premixed flames, Plenum Press, New York, pp. 117-138, 1985.

[85] R. G. Abdel-Gayed and D. Bradley, Combustion regimes and the straining of turbulent premixed flames. Combust. Flame, 76:213-218, 1989.

[86] M. Düsing, Large Eddy Simulation turbulenter Vormischammen. PhD thesis, Technische Universität Darmstadt, 2004.

[87] F. A. Williams, Asymptotic methods in turbulent combustion, AIAA J., 24:867-875, 1986.

[88] H. Pitsch and H. Duchamp de Lageneste, Large Eddy Simulation of premixed turbulent combustion using a level-set approach. Proc. Combust. Inst., 29:2001-2008, 2002.

[89] H. Pitsch, A consistent level set formulation for Large Eddy Simulation of premixed turbulent combustion, Combust. Flame, 143:587-598, 2005.

[90] F. T. M. Nieuwstadt and J.P. Meeder, Large Eddy Simulation of air pollution dispersion: a review, chapter New tools in turbulence modelling, pp. 264-280. Les Editions de Physique - Springer Verlag, 1997.

[91] J. Warnatz, U. Maas and R.W. Dibble. Verbrennung. Springer-Verlag Berlin Heidelberg, 2001.

[92] D.B. Spalding. Mixing and chemical reaction in steady confined turbulent flames. Proc. Combust. Inst., 13:649-657, 1971.

[93] R. Said and R. Borghi, A simulation with a cellular automaton for turbulent combustion modelling. 22nd Symp. (Int.) on Combustion, The Combustion Institute, 569 – 577, 1988.

[94] C. Fureby and S.-I. Möller. Large eddy simulation of reacting flows applied to bluff body stabilized flames. AIAA Journal, 33(12):2339-2347, 1995.

[95] K. K. Kuo, Principles of combustion. John Wiley, New York, 1986.

[96] F. A. Williams, Combustion Theory, Benjamin Cummings, Menlo Park, CA., 1985.

[97] D. Angelberger, D. Veynante, F. Egolfopoulos and T. Poinsot, Large Eddy Simulations of combustion instabilities in premixed flames. Summer Program, Center for Turbulence Research, NASA Ames/Stanford Univ., 61-82, 1998

[98] H.G. Im, T. S. Lund and J. H. Ferziger. Large eddy simulation of turbulent front propagation with dynamic subgrid models. Phys. Fluids, 9:3826-3833, 1997.

[99] J. Piana, D. Veynane, S. Candel and T. Poinsot. Direct and Large Eddy Simulation II, chapter Direct numerical simulation analysis of the G-equation in premixed combustion, 5:321 330. Kluwer Academic Publishers, 1997.

[100] E.R. Hawkes, Large Eddy Simulation of Premixed Combustion. PhD thesis, Cambridge University, 2000.

[101] W.W. Kim, S. Menon and H.C. Mongia. Large-eddy simulation of a gas turbine combustor Flow, Combust. Sci. Tech., 143:25-62, 1999.

[102] V. Yakhot, Propagation velocity of premixed turbulent flames. Combust. Sci. Tech., 60:191-214, 1988.

[103] A. Pocheau. Scale invariance in turbulent front propagation. Phys. Rev. E, 49:1109-1122, 1994.

[104] C. Fureby, A fractal flame-wrinkling large eddy simulation model for premixed turbulent combustion, Proc. Combust. Inst., 30: 593–601, 2005.

[105] S. P. R. Muppala, N. K. Aluri, F. Dinkelacker and A. Leipertz, Development of an algebraic reaction rate closure for the numerical calculation of turbulent premixed methane, ethylene, and propane/air flames for pressures up to 1.0 MPa, Combust. Flame, 140: 257–266, 2005.

[106] V. Zimont and A. Lipatnikov, A numerical model of premixed turbulent combustion of Gases, Chem. Phys. Rep., vol. 14, pp. 993, 1995.

[107] F. Moukalled, L. Mangani and M. Darwish, The finite volume method in computational fluid dynamics: An advanced introduction with OpenFOAM and Matlab, volume 113, Springer, 2015. ISBN 978-3-319-16874-6.

[108] H. K. Versteeg and W. Malalasekra, An introduction to computational fluid dynamics: The finite volume method, Prentice Hall, 2nd edition, 2007. ISBN 978-0-13-127498-3.

[109] C. Hirsch, Numerical computation of internal and external flows, John Wiley & Sons, 1991.

[110] Ö. L. Gülder and G. J. Smallwood, Inner cut-off scale of flame surface wrinkling in turbulent premixed flames. Combust. Flame, 103(1-2):107-114, 1995.

[111] H. Kobayash and H. Kawazoe, Flame instability effects on the smallest wrinkling scale and burning velocity of high-pressure turbulent premixed flames, Proceedings of the Combustion Institute, 28(1):375-382, 2000.

[112] E. Giacomazzi, C. Bruno and B. Favini, Fractal modelling of turbulent combustion, Combustion Theory and Modelling, 4(4):391-412, 2000.

[113] O. Chatakonda, E. R.Hawkes, M. Brear, J. Chen, E. Knudsen and H. Pitsch, Modelling of the wrinkling of premixed turbulent flames in the thin reaction zones regime for large eddy simulation, Center for Turbulence Research, Proceedings of the Summer Program, pp. 611-629, 2010.

[114] G. L. North and D. A. Santavicca, The fractal nature of premixed turbulent flames, Combustion Science and Technology, 72(4):212-232, 1990.

[115] P. Constantin, I. Procaccia and K. Sreenvasan, Fractal Geometry of isoscalar surfaces in turbulence: theory and experiments, Physics review Letters, 67:1739-1743. 1991.

[116] A. Y. Klimenko, Examining the cascade hypothesis for turbulent premixed combustion, Combustion Science and Technology, 139 (1):15-40, 1998.

[117] P. Clavin, Dynamic behaviour of premixed flame fronts in laminar and turbulent flows, Progress Energy and Combustion Science, 11(1):1-59, 1985.

[118] U. C. Müller, M. Bollig and N. Peters, Approximations of burning velocities and Marksteins numbers for lean hydrogen and methanol flames, Combust. Flames, 108(3):349-356. 1997.

[119] J. Göttgen, F. Mauss and N. Peters, Analytic approximations of burning velocities and flame thicknesses of lean hydrogen, methane, ethylene, ethane, acetylene and propane flames, Symposium (International) on Combustion, 24(1):129-135. Twenty-Fourth Symposium on Combustion, 1992.

[120] C. Meneveau and T. Poinsot, Stretching and quenching of flamelets in premixed turbulent combustion, Combust. Flame, vol. 86(4):311-332, 1991.

[121] S. Richard, Large Eddy Simulation of flow and combustion in spark ignition engines, PhD dissertation, IFP-E´ cole Centrale Paris, 2005.

[122] G. Rymer, Analysis and modelling of the mean reaction rate and transport terms in turbulent premixed combustion, PhD dissertation, E´ cole Centrale Paris, 2001.

[123] M. Boger, Sub-grid scale modelling for Large Eddy Simulation of turbulent premixed combustion, PhD dissertation, E´ cole Centrale Paris, 2000.

[124] H.G. Weller, G. Tabor, A.D. Gosman and C. Fureby, Application of a flame-wrinkling LES combustion model to a turbulent mixing layer, Proc. Combust. Inst., 27:899–907, 1998.

[125] S. W. Tullis and R. S. Cant, Scalar transport modelling in Large Eddy Simulation of turbulent premixed flames, Proc. Combust. Inst., 29:2097-2104, 2002.

[126] A. Lipatnikov and J. Chomiak, Turbulent flame speed and thickness: phenomenology, evaluation, and application in multi-dimensional simulations. Progress in Energy and Combustion Science 28(1):1-74, 2002.

[127] D. Veynante and L. Vervisch, Turbulent combustion modelling. Progress in Energy and Combustion Science 28:193-266, 2002.

[128] K. N. C. Bray, M. Champion and P. Libby, Pre-mixed flames in stagnating turbulence: Part V-evaluation of models for the chemical source term. Combust. Flame 127:2023-2040, 2001.

[129]. A. Kempf, M. Klein and J. Janicka, Efficient generation of initial and inflow conditions for transient turbulent flows in arbitrary geometries, Flow Turbul. Combust., vol. 74(1):67–84, 2005.

[130] E. Tangermann and M. Pfitzner, Evaluation of combustion models for combustion-induced vortex break-down, J. Turbul., vol. 10(7), 2009.

[131] S. B. Pope, Turbulent flows, Cambridge University Press, Cambridge, UK, 2000.

[132] M. Klein, An attempt to assess the quality of large eddy simulations in the context of implicit filtering, Flow Turbul. Combust., vol. 75:131-147, 2005.

[133] I. B. Celik, Z. N. Cehreli and I. Yavuz, Index of resolution quality for Large Eddy Simulations, J. Fluids Eng., vol. 127(5):949–958, 2005.

[134] R. Mercier, V. Moureau, D. Veynante and B. Fiorina, LES of turbulent combustion: On the consistency between flame and flow filter scales, Proc. Combust. Inst., vol. 35:1359-1366, 2015.

[135] F. Schwertfirm and M. Manhart, DNS of passive scalar transport in turbulent channel flow at high schmidt numbers, Int. J. Heat Fluid Flow, vol. 28(6):1204-1214, 2007.

[136] M. Boger and D. Veynante, Large Eddy Simulations of a Turbulent Premixed V-shaped Flame, Advances Turbulence, Dopazo C. (ed.), Cimne, Barcelona, pp. 449-452, 2000.

[137] A. W. Vreman, Direct and Large Eddy Simulation of the compressible mixing layer, PhD Thesis, University of Twente, 1995.

[138] B. Hakberg and A. D. Gosman, Analytical Determination of Turbulent Flame Speed from Combustion Models, Proc. Combust. Inst., vol. 20:225-232, 1984.

[139] M. Klein, N. Chakraborty and Y. Gao, Scale similarity based models and their application to subgrid scale scalar flux modelling in the context of turbulent premixed flames, Int. J. Heat Fluid Flow, vol. 57:91–108, 2016.

[140] F. Fichot, F. Lacas, F. Veynante and D. Candel, One-dimensional propagation of a premixed turbulent flame with a balance equation for flame surface density, Combust. Sci. Technol., vol. 90:35-60, 1993.

[141] U. Allauddin, M. Klein, M. Pfitzner and N. Chakraborty, A-priori and a-posteriori analysis of algebraic flame surface density modelling in the context of large eddy simulation of turbulent premixed combustion, Num. Heat Trans., A, in press, 2016.

[142] N. Chakraborty, G. Hartung, M. Katragadda and C. F. Kaminski, A Numerical Comparison of 2D and 3D Density-weighted Displacement Speed Statistics and Implications for Laser Based Measurements of Flame Displacement Speed, Combust. Flame, vol. 158:1372-1390, 2011.

[143] M. Klein, N. Chakraborty and M. Pfitzner, Analysis of the Combined Modelling of Subgrid Transport and Filtered Flame Propagation for Premixed Turbulent Combustion, Flow Turbul. Combust., vol. 96:921-938, 2016.

[144] R. G. Abdel-Gayed, D. Bradley, M. N. Hamid and M. Lawes, Lewis number effects on turbulent burning velocity, Symp. (Int.) Combust., vol. 20:505–512, 1984.

[145] F. Dinkelacker, B. Manickam and S. P .R Muppala, Modelling and simulation of lean premixed turbulent methane/hydrogen/air flames with an effective lewis number approach, Combust. Flame, vol. 158:1742-1749, 2011

[146] N. Chakraborty and R.S. Cant, Effects of lewis number on flame surface density transport in turbulent premixed combustion. Combust. Flame, vol. 158:1768–1787, 2011.

[147] R. Keppeler, Entwicklung und Evaluierung von Verbrennungsmodellen für die Large Eddy Simulation der Hochdruck-Vermischverbrennung, PhD. Thesis, University of Bundeswehr, Munich, 2013.

[148] T. Ma, O. T. Stein, N. Chakraborty and A.M. Kempf, A Posteriori Testing of the Flame Surface Density Transport Equation for LES, Combust. Theor. Model., vol. 18:32-64, 2014.

[149] M. Katragadda, N. Chakraborty and R.S. Cant, A Priori assessment of algebraic flame surface density models in the context of large eddy simulation for non-unity Lewis number flames in the thin reaction zones regime, J. Combust., 2012, article ID 794671, 17 pages, 2012.

[150] M. Katragadda, N. Chakraborty and R.S. Cant, Effects of turbulent Reynolds number on the performance of algebraic flame surface density models for large eddy simulation in the thin reaction zones regime: A Direct Numerical Simulation analysis, J. Combust. 2012, article ID 353257, 13 pp., 2012.

[151] J. F. Driscoll, Turbulent Premixed Combustion: Flamelet structure and its effect on turbulent burning velocities, Prog. Energ. Combust. Sci., vol.34:91–134, 20